



HAL
open science

Advanced signal and imaging methods in ultrasound cortical bone assessment

Chao Han

► **To cite this version:**

Chao Han. Advanced signal and imaging methods in ultrasound cortical bone assessment. Signal and Image Processing. Sorbonne Université, 2019. English. NNT : 2019SORUS144 . tel-03141324

HAL Id: tel-03141324

<https://theses.hal.science/tel-03141324>

Submitted on 15 Feb 2021

HAL is a multi-disciplinary open access archive for the deposit and dissemination of scientific research documents, whether they are published or not. The documents may come from teaching and research institutions in France or abroad, or from public or private research centers.

L'archive ouverte pluridisciplinaire **HAL**, est destinée au dépôt et à la diffusion de documents scientifiques de niveau recherche, publiés ou non, émanant des établissements d'enseignement et de recherche français ou étrangers, des laboratoires publics ou privés.

Sorbonne Université

École doctorale

Sciences mécaniques, acoustique, électronique et robotique de Paris

Advanced signal and imaging methods in ultrasound cortical bone assessment

Par Chao Han

Thèse de doctorat de Acoustique Physique

Dirigée par M. Didier Cassereau et M. Jean-Gabriel Minonzio

Présentée et soutenue publiquement le 23 avril 2019

Devant un jury composé de:

Rapporteurs :	Marc BONNET	Directrice de recherche, ENSTA ParisTech
	Marc DESCHAMPS	Directeur de Recherche, Université de Bordeaux
Examineurs :	Vincent GIBIAT	Professeur, Université Paul Sabatier
	Nathalie FAVRETTO-CRISTINI	Chargé de recherche, Aix-Marseille Université
	Régis MARCHIANO	Professeur, Sorbonne université
Directeur de thèse:	Didier CASSEREAU	Maître de conférences, ESPCI Paris
Co-encadrant :	Jean-Gabriel MINONZIO	Maître de conférences, Universidad de Valparaiso

Acknowledgements

My deepest gratitude goes first and foremost to my supervisor Dr. Didier Cassereau, for his constant encouragement and guidance. He has walked me through all the stages of the writing of this thesis. Without his consistent and specific modification, this thesis could not have reached its present form. And in the four years Ph.D study, Didier cultivated my basic research literacy and the way of thinking logically, help me with even small problem under a grate patience. He also give me a lot of opportunities to attend lots of interaccional conference, makes me learn how to present my work in the best way and communicates with researches in other community, which is very helpful for expanding my vision in my research. Didier also encourage me explore in my subject with a great freedom, these benefits from his guidance can shown in this thesis. Additionally, I also very grateful his support for my adventure on creating my startup, this is very preciously experience in my four years.

I would like to thank Dr. Jean-Gabriel Minonzio, who is co-supervised me, specially very patient in guiding my work. He always help me to correct my mistakes especially in some subtle places. I am grateful to Dr. Quentin Grimal who is the leader of DBMS team, give me a lot an additional guidance, especially for the submitted papers. His rigorous attitude and meticulous logic influence me a lot. He has given me so much useful advices on my writing, and has tried his best to improve my paper. The special thanks to Dr. Pascal Laugier, who is the director of laboratory, recommended me to my supervisor Didier Cassereau. His extremely involving in research field and broad vision influence me a lot.

I would like to thank all the jury members for taking the time to examine my work, especially the reporters: Dr. Marc Bonnet and Dr. Marc Deschamps. I am very touched by their careful review and errata, serious and responsible research spirit. I would like to thank Dr. Pascal Dargent, who helped in implementing some experiments in Laugiven institution and he always help me in engineering domain with high enthusiastically. I would also like to thank Dr. Guillaume Renaud and Dr. Sylvain Hauptert, they always willing to help me in solving software and hardware problems in my work, which make my project progressed smoothly. And I also feel very lucky to meet the wonderful people in LIB, we spent very happy and unforgettable good times in Paris.

Special thanks go to my dear colleagues and my partner in my startup, the cherish experience for one year in the startup which makes me realize the importance of scientific research for helping people, and I am proud we are doing great things to helping cancer patient and we will never give up in a huge dilemma.

Last my thanks would go to my beloved family for their loving considerations and great confidence in me all through these years. No words can express my love to them.

Abstract

The quantitative ultrasound plays an irreplaceable role in cortical bone assessment, since of its mechanical characters and lack of ionizing radiation compare to Computed Tomography and Dual Energy X-ray Absorptiometry (DXA). Ultrasound technologies provides an affordable mean to implement non-invasive solutions to diagnostically assess the mechanical characteristics of the bone. Pulse-echo ultrasonometry can be used as a pre-screen for hip osteoporosis before dual-energy x-ray absorptiometry (DXA). In this thesis, We introduce the sparse reconstruction method into pulse-echo ultrasound of cortical bone assessment, which the aim is to estimate the ultrasound parameters of cortical bone, including the cortical thickness (Co.Th) and normalized broadband ultrasound attenuation (nBUA). The second main contribution is that we introduce Time Domain Topological Energy (TDTE) method and Full Waveform Inversion (FWI) into cortical bone imaging.

Pulse-echo ultrasound is a popular method to estimate the cortical thickness (Ct.Th) from the time delay between echoes stemming from the outer and inner bone surfaces. The thickness of cortical bone is typically close to the wavelength of ultrasound used for bone assessment, resulting in temporal overlapping of echoes. Increasing measurement frequency lowers the amplitude of echoes which are then mixed with intercortical backscattered signals. Accurate recovering of ultrasound echoes from cortical bone surfaces is an open signal processing problem. We introduce Orthogonal Matching Pursuit (OMP) to unambiguously identify echoes bouncing off the bone periosteal and endosteal boundaries. OMP is a model-based approach which allows a robust reconstruction of the waveform of each echo even in the case of temporal overlapping. Following echoes identification, Ct.Th is estimated by measuring their time-of-flight. Furthermore, the center frequency shift of both echoes yields the slope of the frequency attenuation coefficient, thereafter referred to as the normalized broadband ultrasonic attenuation (nBUA). In absence of noise and attenuation, numerical simulation results indicate that a lower limit for an accurate reconstruction of echoes is $\text{Ct.Th}/\lambda = 0.38$. Successful measurement of Ct.Th and nBUA is demonstrated in vivo. Site-matched reference values of cortical thickness and volumetric bone mineral density (vBMD) were obtained using high-resolution peripheral computed tomography. Ct.Th is highly correlated to reference thickness ($r^2 = 0.92$) and nBUA to vBMD ($r^2 = 0.90$).

This is the first time we introduce TDTE in cortical bone imaging. By using a simple homogeneous fluid reference medium, the TDTE image can be obtained efficiently. However, this efficient choice of reference medium, only the external boundary of cortical bone can be reconstructed well, the internal boundary of cor-

tical bone is weak in the TDTE image and mismatched with its real position. The TDTE with sparse signal processing or iterative TDTE can give a satisfied solution on cortical bone image. However, it only can give the geometry structure information, but can't give a quantitative image. In geophysics domain, migration and Full waveform inversion are widely used to give the image as well as the quantitative information of earth interior, including distribution of density, P-wave velocity and S-wave velocity. It has the familiar principle with TDTE, which is trying to minimize the difference between the reference model and inspected model. Both of them are solving minimization of misfit function by adjoint method, involving simulating the forward and adjoint field on reference model. The difference between them is the derivation of misfit function. TDTE is driven from topological optimization, the derivation of misfit function is mainly based on the structure of reference medium. In the migration and FWI, the minimization is respected on the model parameters: density, P-wave velocity and S-wave velocity.

The migration imaging is produced by one step gradient minimization, which means the migration only gives a rough quantitative distribution of parameters. It tries to provide the solution which is most closed to the real model in one iteration. In the numerical simulation, we can observe that, the density and impedance kernels can provide us the internal boundary of cortical bone.

FWI can give distribution of the density, compressive wave speed and shear wave speed, but it is required with huge time and computation consuming through iterations optimization process. TDTE shows well performance in extracting the structure of cortical bone, including external, internal boundary of cortical bone and porous structure inside cortical bone. The advanced signal and imaging methods, which is sparse signal processing, FWI and TDTE respectively, show strong potential to increase the capacity of pulse-echo ultrasonometry in assessment of cortical bone.

Keywords Cortical bone thickness estimation, Broadband ultrasound attenuation, cortical imaging, Time domain Topological Energy, migration, Full waveform inversion

Contents

Abstract	iii
1 Introduction	1
1.1 Background of QUS in cortical bone assessment	4
1.1.1 QUS measurements	5
1.1.2 three model of QUS measurement	9
1.1.3 the improvement of these thesis in bone parameters estimation	12
1.2 Background of ultrasound imaging in industrial and medical domain	13
1.2.1 ultrasound tomography	13
1.2.2 Full waveform inversion	16
1.2.3 Time domain topological energy	17
1.2.4 The improvement of cortical bone imaging in this thesis . . .	20
2 Sparse signal processing in the evaluation of the cortical bone	23
2.1 Sparse signal processing	26
2.1.1 Signal model	26
2.1.2 Dictionary	27
2.1.3 Orthogonal Matching Pursuit	28
2.1.4 Adapted Orthogonal Matching Pursuit	30
2.2 Estimation of the Cortical Thickness and Broadband Ultrasound At-	
tenuation	32
2.3 Numerical simulation of the OMP in the cortical bone assessment . .	35
2.3.1 2D numerical simulation	35
2.3.2 Application of OMP in imaging with a phased array transducer	36
2.4 Experimental validation	38
2.4.1 The sawbone plates	38
2.4.2 <i>Ex-vivo</i> measurement of the cortical bone	41
2.4.3 <i>In-vivo</i> measurement of the cortical bone	43
2.4.4 Results	44
2.5 Discussion	46
2.6 Appendix: Comparison between OMP and the envelop method . . .	48
2.7 Appendix: Received <i>in vivo</i> signal and reconstruction by OMP . . .	48

3	Cortical bone imaging by Time Domain Topological Energy	53
3.1	Time Domain Topological Gradient	55
3.1.1	Cost function	55
3.1.2	The topological gradient for linear elasticity and elastodynamics	56
3.1.3	Iterative process for the Time Domain Topological Gradient .	59
3.2	Numerical simulations	62
3.2.1	Image of a 2D cross-section of cortical bone	62
3.3	Result Discussion	65
3.3.1	Velocity mismatch	65
3.3.2	Sampling frequency and time interval in TDTE integration .	67
3.4	<i>in vitro</i> femur neck cortical bone validation	71
4	TDTE with Sparse Signal Processing for Cortical Bone Imaging	75
4.1	Sparse Signal Processing	76
4.1.1	Signal Model	76
4.1.2	Simplified version of OMP	76
4.1.3	Model based OMP without building dictionary	77
4.2	Additional processing	80
4.2.1	Envelope processing	80
4.2.2	Curve fitting	81
4.3	Numerical simulation	81
4.4	Experimental validation using the cortical bone phantom	86
4.5	Appendix	90
5	Iterative TDTE applied to cortical bone imaging	95
5.1	Iterative TDTE	95
5.2	Numerical simulation	98
5.2.1	Cortical bone with irregular internal boundary	98
5.3	bone phantom validation	102
5.4	Iterative TDTE of cortical bone with osteoporosis (pores inside cortical bone)	105
6	Quantitative Imaging of Cortical Bone by Full Waveform Inversion	113
6.1	Migration by adjoint method	114
6.1.1	The connection between imaging and adjoint kernels	117
6.1.2	Numerical implementation of sensitive kernels	117
6.2	Numerical imaging of cortical bone internal boundary by adjoint kernels	120
6.3	Full waveform inversion	125
6.4	Numerical Implement	128

6.4.1	pre-processing, post-processing, Nonlinear optimization . . .	128
6.4.2	Numerical implement	130
7	Summary and conclusion	133
7.1	Summary	133
7.2	Comparation between TDTE, migration and full waveform inversion	136
	Bibliography	139

List of Figures

1.1	Cortical porosity in post-mortem specimens from women aged 78 and 90 years ((Zebaze et al., 2010)) (A) Micrograph of a specimen from a 78-year-old woman. Intracortical porosity is extensive and associated with cortical thinning due to transformation of the inner cortex into a trabecularised structure of cortical remnants. White arrows show areas containing cortical remnants. Cortex adjacent to periosteum (B) appears compact with enlarged pores, but without trabecularisation. (C) The preserved endocortical envelope (shown by arrows) suggests that cortical thinning occurred from within the bone. (D) Micrograph of a specimen from a 90-year-old woman. Cortex is largely porous and looks similar to a sponge.	6
1.2	Commercial devices incorporating BUA for the assessment of osteoporosis: a) Hologic Sahara (US), b) GE Achilles (US), c) Osteometer DTU-one (DK), d) DMS UBIS-5000 (DR).	8
1.3	a) the first cortical thickness measured by pulse-echo ultrasound (Wear, 2003) b) a device to measure cortical thickness and elastic parameter by guided wave (Vallet et al., 2016)	9
1.4	a) the Pulse-echo ultrasound, the transmitting and receiving transducers are the same. b) the through-transmission on heel, the transmitting and receiving transducers are located at opposite sides of the target object. c) the transverse transmission on femur neck. d)axial-transmission measurement at the radius.	10
1.5	Operating modes in Ultrasonic Computed Tomography ((Lasaygues, 2006)). a) a single transducer in reflected mode, b) 2-D ring in the diffraction mode, c) two paired transducers in transmission mode . .	14
1.6	a) human thighbone: the left is CQUT image by 90 projections, 128 transducer, the right is corresponding X-ray tomography. b) DBDT image of a bone mimicking phantom, left is initial solution of DBDT at 350kHz, right is iteration at 1MHz ((Lasaygues et al., 2011)) . . .	15
1.7	An example ((Nguyen and Modrak, 2018)) of quantitative imaging by FWI results of the synthetic test: (a) true model, (b) initial model, (c) inverted model by FWI.	18

1.8	(a) Scheme of the experimental setup by P. Sahuguet and V. Gibiat (2015), (b) Resulting topological energy image with a logarithmic scale of 45dB dynamic. (c) Numerical setup of Density map of the inspected medium (in black 1000 kg/m ³ and white 1051 kg/m ³), (d) Image of the topological energy with a logarithmic scale of 45dB dynamic	20
2.1	principle of the ultrasound pulse-echo measurement to estimate the thickness of the cortical bone	25
2.2	OMP for strong overlapping case: up: the received signal from simulation and its envelop, down: derivation of the envelop and its correspond time matching interval	31
2.3	(a) measurement of the BUA in transmission: 1 and 5 correspond to soft tissues, 2 and 4 to the cortical bone and 3 to the trabecular bone (b) measurement of the BUA in reflection	34
2.4	(a) the numerical map of a tube with sawbone-equivalent material immersed in water, (b) the received signal when the frequency is 1MHz (c) its reconstruction by OMP	37
2.5	(a) mean square error of the reconstructed signal for different values of the ratio thickness/wavelength (b) estimated thickness precision in percentage	38
2.6	(a) the separation of two echoes when the Co.Th./ λ is 0.38, (b) its reconstruction, (c) the separation of two echoes when the Co.Th./ λ is 0.25, (d) its reconstruction.	39
2.7	numerical validation of OMP in B-scan view: a) the received signals from a 1MHz excitation, b) the reconstructed signals by OMP with a 3MHz pulse, c) the received signals from a 3MHz excitation and d) superposition of (b) and (c)	40
2.8	pulse echo ultrasound experimental setup for (a) bone phantom (b) tibia (<i>ex-vivo</i>) and (c) radius (<i>in-vivo</i>)	41
2.9	the two main echoes reconstruction, <i>ex-vivo</i> tibia measurement, using a 3.5MHz excitation	42
2.10	(a) linear correlation between the values of the cortical thickness by HRpQCT and OMP ; (b) linear correlation between the vBMD by HRpQCT and nBUA by OMP	45
2.11	The linear fit between the cortical thickness determined by pQCT and time delay estimated in (Karjalainen et al., 2008a)	47

2.12	Up: the time delays estimated by OMP (<i>in vivo</i> signal), the black arrow indicates the reverberations. Down: the time delay estimated by the envelop method (<i>in vivo</i> signal)	49
2.13	5 samples of received signals in-vivo (gray line) and its reconstruction (red dashed line) by OMP, the line array indicates the unknown deformations and multi-scatters	51
2.14	5 samples of received signals in-vivo (gray line) and its reconstruction (red dashed line) by OMP, the line array indicates the unknown deformations and multi-scatters	52
3.1	principle of the topological asymptotic method	55
3.2	numerical scheme of TDTE	61
3.3	the numerical simulation setup	63
3.4	(a) numerical simulation setup with the transducer array at 160 degrees, (b) received signals (c) TDTE image and (d) TDTE image and original map	64
3.5	(a) reconstructed image of the cortical bone by TDTE, (b) reconstructed and original images of the cortical bone	65
3.6	(a) the points locations chosen in TDTE image and original image, (b) the estimated cortical thickness and real thickness corresponding to the chosen points	66
3.7	the water is changed by homogeneous fluid longitude wave-speed is 4000 m/s: (a) the TDTE image, (b) its superposition with original map	67
3.8	TDTE image for an integration frequency (a) $f_e/10$, (b) $f_e/30$ and (c) $f_e/100$	68
3.9	the received signal with short time duration and its TDTE image . .	69
3.10	the received signal with medium time duration and its TDTE image	70
3.11	the received signal with long time duration and its TDTE image . .	71
3.12	the experimental setup for <i>in vitro</i> cortical bone imaging	72
3.13	(a)the B-scan view of received signal in position 1, (b) the corresponding TDTE image, (c) the micro CT image of femur neck, where the white rectangular is the reconstructed area	73
4.1	(a) received signal and envelop, (b) envelopes reconstructed by OMP	78
4.2	(a) the envelope by Hilbert transform (b) peak interpolation of the Hilbert transform	81

4.3	(a) received signals for the array located at an angle of 225 degrees (b) its envelop (c) time delays corresponding to the first echo by OMP and fit (d) time delays corresponding to the second echo by OMP and fit (e) time delays after curve fit (f) difference between original and reconstructed envelopes	82
4.4	the configurations when the array located in (a) 270 degree and (b) 315 degree	83
4.5	(a) received signals for the array located at an angle of 315 degrees, (b) time delays by OMP, (c) corrected time delays and amplitudes, (d) reconstructed TDTE image	84
4.6	(a) received signals for the array located at an angle of 270 degrees, (b) time delays OMP, (c) recorrected time delays and amplitudes, (d) reconstructed TDTE image	85
4.7	full reconstructed image of the cortical bone sample with TDTE and OMP, superimposed with the original map	86
4.8	(a) femoral neck bone phantom, (b) geometrical parameters of the bone phantom	87
4.9	Experimental setup	92
4.10	TDTE at 0 degree: (a) received signals without any processing, (b) reconstructed signal by OMP and increase of the frequency, (c) cor- rected time delays for the echoes from the inner boundary, (d-f) cor- responding TDTE images.	93
4.11	reconstructed image by TDTE and OMP, blue lines represent the contours of the bone phantom	93
5.1	the numerical setup for TDTE cortical bone imaging	96
5.2	the scheme of first iterative TDTE	97
5.3	the second iteration of TDTE, reference medium is modified accord- ing to the result from first iteration	98
5.4	(a) numerical setup, the red area represents the bone material, (b) reference medium used for the second iteration of TDTE	99
5.5	(a) left:received signals from inspected medium, middle: received sig- nals from reference medium, right: their difference. (b) up: the signal from inspected medium and reference medium from one transducer (No.110), down: their difference	100
5.6	reconstructed image from the second iterations of TDTE and its overlapping with original inspected cortical bone	101
5.7	the reconstructed image by 2 iterations of TDTE and its overlapping with original image of cortical bone	102

5.8	the cross-section view of experimental setup for measuring the bone phantom, where the red bold line represents the ultrasound transducer array	103
5.9	(a) the TDTE image by first iteration, where the red stars represent the transducer array (b) B-scan image	103
5.10	(a) the external boundary extracted from TDTE image, (b) curve fitting of the extracted point from (a), (c) reference medium used for the second iteration	104
5.11	the TDTE image in second iteration and its overlapping with original bone phantom	105
5.12	(a) CT image of a cross-section of cortical bone, (b) numerical configuration	106
5.13	(a) first iteration of TDTE, (b) second iteration of TDTE	107
5.14	Left: numerical configuration, Right: corresponding TDTE image from the second iteration	109
5.15	the summation of three TDTE images, from three different angles	110
5.16	CT image from a femur neck cortical bone with osteoporosis	111
5.17	the second iterative TDTE image of osteoporosis femur neck	111
6.1	(a) the numerical setup of cortical bone when array located in 0 degree (b) the numerical setup of reference medium in specfem2D (the gray and blue areas correspond to the cortical bone and water, respectively, the green stars represent the transducer array)	121
6.2	the scheme of numerical simulation perform by Specfem2D	122
6.3	(a) K_ρ kernel (b) $K_{\hat{\rho}}$ kernel (c) K_κ kernel (d) K_α kernel (e) K_μ kernel (f) K_β kernel	123
6.4	K_α kernel	124
6.5	(a) K_ρ kernel (b) $K_{\hat{\rho}}$ kernel (c) K_κ kernel (d) K_α kernel (e) K_μ kernel (f) K_β kernel	126
6.6	the scheme of Full waveform inversion	128

List of Tables

2.1	Properties of sawbone used in the numerical simulation and water. L and T stand for longitudinal and transverse waves	36
2.2	the ultrasound parameters of sawbone, where L and T stand for longitudinal and transverse components	39
2.3	the ultrasound parameters estimated by OMP in bone phantom plate, using 1MHz excitation	40
2.4	parameters estimated by OMP on <i>in-vitro</i> tibias	43
2.5	the ultrasound parameters estimated in <i>in vivo</i> measurement at radius	44
2.6	the time delays, corresponding Co.Th. and nBUA of <i>in vivo</i> mea- surement at radius	45
2.7	Mean BUA of cortical bone and standard deviation, resulting from <i>in vivo</i> measurements and previously measurements	50
3.1	Topological asymptotic method for linear elasticity	58
3.2	Topological asymptotic for elastodynamics	58
3.3	Properties of the cortical bone phantom and water. L and T stand for longitudinal and transverse components	62
4.1	Comparison of longitudinal and transverse velocities, mass densities and attenuation coefficients between Sawbone (bone-mimicking ma- terial) and human cortical bone (mid-diaphysis of the femur), mea- sured in the plane of isotropy. L and T stand for longitudinal and transverse components.	87
7.1	the comparison of three imaging method	137
7.2	the quantify comparison of three imaging method	138

CHAPTER 1

Introduction

Quantitative ultrasonic (QUS) characterization is emerging development as an alternative to photon absorptiometry techniques in evaluating the risk of fracture and osteoporosis. The QUS parameters, known as broadband ultrasonic attenuations (BUA) and Speed of Sound (SOS), are correlated with the well-established variable bone mineral density (BMD) has been reported in previous studies. Most of development of QUS technique is still confined to cancellous bone. However, cortical bone exploration is more interested since the cortical loss is the mainly factor in the skeletal biomechanics' stability. Considering achieving each one of Cortical Thickness (Co.Th.) and SOS, the other parameter should be predefined. Using Pulse-Echo (PE) ultrasound to estimate the Co.Th by considering SOS as constant has been well investigated in vivo and in vitro. Previous work mainly focuses on tibia cortical bone, the radius cortical bone with thinner thickness and smaller variance needs higher resolution method. Benefiting from the development of sparse signal processing method recently, high resolution of ultrasound parameter can be achieved by building an over-completed dictionary in terms of possible parameters. Additionally, the BUA can be obtained by the estimated ultrasound parameter. The other challenge is that high frequency of ultrasound is limited by strong contrast and high absorbance of bone, lower frequency of ultrasound with deeper penetration in cortical bone may lead to series overlapping. The sparse method is also well performed to separate the overlapped echoes of cortical bone accurately. Orthogonal Matching Pursuit as the sparse method is introduced here to estimate the BUA and Co.Th of cortical bone at the same time, it enhances the PE ultrasound to a high resolution and efficient tool for applying ultrasound in cortical bone assessment.

To determine the structure of cortical bone is leading to an intuitionistic approach in predicting the risk of fracture and osteoporosis. Methods for assessing high resolution image of microstructure of cortical bone includes DXA and micro-CT. Ultrasound technologies provides an affordable mean to implement non-invasive solutions to imaging the cortical bone structure without ionizing radiation. However, the currently clinical ultrasound imaging methods are mainly based on travel times of transmitted pulses, they are limited in imaging of cortical bone because of its high frequency attenuation of bone and the multiple scatters including shear wave caused by cortical bone. Improving the performance of ultrasound imaging will

potentially make it to be a comprehensive clinical mean in accessing both structure information and bio-mechanical characters.

Benefiting from the development of simulation technology, Geophysics developed elegant techniques named Full Waveform Inversion (FWI). It has been shown inspiring performers in improving resolution of earth's inner imaging. Compared to traditional migration imaging, the FWI define a synthetic field, which to make its structure approaching to the inspected field by minimizing the waveform misfit between the real measured wavefield and the simulated wavefield. This kind of minimization is solving by iterative procedure based on gradient, which respects to the density and elasticity parameters of model, yielding to six kernels represented the distribution of the density, compressive wave speed and shear wave speed. The first iteration of FWI is migration, which can give us a proximate estimation without iteration. Time domain Topological energy is a similar imaging technology with the same principle, which comes from the mathematical community of shape optimization. so, it only can give the structure information, instead of quantitative image obtained from Full Waveform Inversion. The advantage compare to FWI, is high efficiency and imaging the small size defects inside the medium.

This is the first time we introduce TDTE in cortical bone imaging. By using a simple homogeneous fluid reference medium, the TDTE image can be obtained efficiently. However, this efficient choice of reference medium, only the external boundary of cortical bone can be reconstructed well, the internal boundary of cortical bone is week in the TDTE image and mismatched with its real position.

There are two different ideas to deal with this problem: one is to increase the time-delay and amplify the amplitude of the second main echo, which is corresponding to the internal boundary. This involves the signal processing of time delay estimation. By applying the OMP we used in previously part, the second main echo can be reconstructed by amplifying the amplitudes and increasing the time delays, which is the ratio between the wave velocity in cortical bone and reference medium (water). This approach can successful reconstruction the external and internal boundary of cortical bone in numerical simulation and sawbone of femur neck. However, it only can handle the regular internal boundary. For irregular internal boundary, the echoes corresponding to the internal boundary are difficult to identify. Under such circumstance, the iterative TDTE by improving the reference medium with previous iteration information is the only option. In cortical bone imaging application, the reference medium in second iteration should utilize the information from the first iteration, by setting the material under external boundary to be bone. So, the second iteration of TDTE can reconstructed the difference between the real inspected cortical bone and updated reference medium, which is

the internal boundary of cortical bone. The disadvantage of iterative TDTE is the computation and storage burden. For a homogenous reference medium, the displacement wave field can be obtained by analytical solution, for the non-homogenous medium, the displacement of wave field can be obtained only by the numerical simulation software. So, both of the forward and adjoint wavefield need to be stored. The iterative TDTE are also show a good performance in numerical simulation and sawbone of femur neck.

The TDTE with sparse signal processing or iterative TDTE can give a satisfied solution on cortical bone imagine. However, it only can give the geometry structure information, but can't give a quantitative image. In geophysics domain, migration and Full waveform inversion are widely used to give the image as well as the quantitative information of earth interior, including distribution of density, P-wave velocity and S-wave velocity. It has the familiar principle with TDTE, which is trying to minimize the difference between the reference model and inspected model. Both of them are solving minimization of misfit function by adjoint method, involving simulating the forward and adjoint field on reference model. The difference between them is the derivation of misfit function. TDTE is driven from topological optimization, the derivation of misfit function is mainly based on the structure of reference medium. In the migration and FWI, the minimization is respected on the model parameters: density, P-wave velocity and S-wave velocity. So the minimization of misfit function yields six sensitive kernel, represented the distribution of density, P-wave velocity and S-wave velocity.

The migration imaging by six sensitive kernels are produced by one step gradient minimization, which means the migration only gives a rough quantitative distribution of parameters. It tries to provide the solution which is most closed to the real model in one iteration. In the numerical simulation, we can observe that, the density and impedance kernels can provide us the internal boundary of cortical bone, but the accurate parameters distribution is not sufficient. If we want to obtain more accurate distribution, the iterative procedure is required, which is full waveform inversion.

The outline of each Chapters are concluded as follows:

Chapter two describes the sparse signal processing applying in Pulse-echo ultrasound to estimate the cortical thickness (Co.Th.) and broadband ultrasound attenuation (BUA).

Chapter three describes the scheme of TDTE and its application in *in vitro* cortical bone imaging.

Chapter four introduces the TDTE embedded with OMP to improve the internal boundary of cortical bone, and it is validated in numerical simulation and cortical bone phantom.

Chapter five introduces iterative TDTE to deal with the irregular internal boundary of cortical bone, and it is validated in numerical simulation and cortical bone phantom.

Chapter six introduces the Full Waveform Inversion, mainly migration in cortical bone imaging.

Chapter seven makes a discussion of the result and conclusion, especially compares the TDTE, migration and FWI in cortical bone imaging.

1.1 Background of QUS in cortical bone assessment

Osteoporosis has been recognized as a silent epidemic and there is increasing demand to mass screening and management. It results from a period of asymptotic bone loss and hence reduced bone strength. Currently, the mainly clinical assessment of osteoporosis relies on the Bone Mineral density (BMD) measured by dual X-ray absorptiometry (DXA) and quantitative X-ray computed tomography (QCT) (Frost et al., 2001; Kanis and Gluer, 2000; Marshall et al., 1996), which are ionizing radiation and relatively expensive and bulky.

BMD is not sufficient to evaluate the strength of bone, while the remain part is due to bone micro structure and bone mechanical properties. Since ultrasound is a mechanical wave, it can be used to represent the mechanical properties of cortical bone through the variation of speed of sound, frequency attenuation, when it is propagating through the cortical bone. It is possible that ultrasound might give some architectural information about the bone and thus improve strength estimation. There is a growing interest in potential applications of quantitative ultrasound (QUS), because it is non-ionizing, relatively portable and relatively less expensive than DXA (Barkmann et al., 2008, 2009; Bauer, 1997; Frost et al., 2001; Hans and Krieg, 2008). This chapter will give a review of ultrasound in cortical bone assessment.

1.1.1 QUS measurements

Osteoporosis mainly caused by cortical loss shown in Fig. 1.1.1 (Bousson et al., 2006; Holzer et al., 2009; Mayhew et al., 2005) is currently diagnosed by dual X-ray absorptiometry (DXA) as a standard method for assessment of bone mineral density (BMD) (Greenfield, 1998). However, the BMD is not sufficient to evaluate the cortical bone strength (Siris et al., 2004), (Briot et al., 2013). Quantitative ultrasound (QUS) can be an effective mean to investigate the bone strength, which has played an increasing role in the assessment of bone status in past decades (Grimal et al., 2013; Mano et al., 2015; Stein et al., 2013). The QUS parameters known as broadband ultrasound attenuation (BUA) and speed of sound (SOS) are well correlated with the established variable bone mineral density (BMD) reported in (Enneman et al., 2014; Krieg and Didier, 2010; Olszynski et al., 2016; Prins et al., 2008; Töyräs et al., 2002). Currently, QUS is emerging an alternative tool to absorptiometry techniques to evaluation the risk of fracture and osteoporosis, some significant innovations of applying QUS in investigating of cortical bone statues will deliberate in following context. QUS is now showing a promising probability in clinical application as a predictor of hip fracture and osteoporosis (Hans and Krieg, 2008), (Hans and Baim, 2017). However, the performance of these techniques still has a large room to improve. The rapid development signal processing techniques provide us a potential tool to improve the performance of these method in aspects of accuracy, resolution and robust.

Speed of sound

The velocity of an ultrasound wave depend on both of the properties of the medium and the propagated mode. Cortical bone is a elastic modulus where the wave propagates containing a longitudinal and shear waves. The clinical velocity measurements including pulse-echoes and transmission technology by recording the travel time in a known distance, usually measured by X-ray based imaging method. In the bone application, the traveling time is denoted as time of flight (TOF), which usually measured by detect a specific reference point in the transmitted wave. As such reference points, the first point when a fixed or relative threshold is exceeded (Haiat et al., 2005), (Langton et al., 2001), (Nicholson et al., 1999), first or second maximum (Laugier et al.), envelope maximum (Le, 1999), zero crossing (Currey, 2001), (Rossman et al., 2001), or correlation maximum (Strelitzki et al., 1999) have been used. Alternatively, the phase velocity can be calculated in the frequency domain (Droin et al., 1998). In some application, the time of flight (TOF) as a single parameter measured by assuming a constant heel thickness and therefor the velocity measured is dependent upon heel width. using the SOS to evaluate

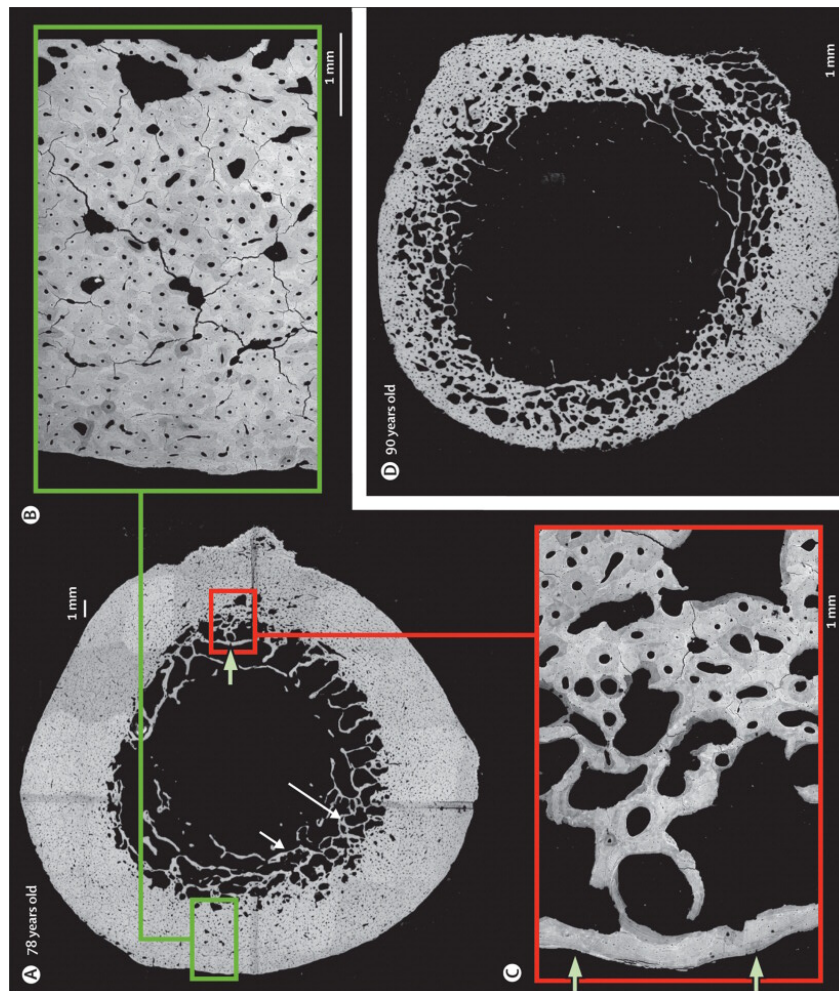


Figure 1.1: Cortical porosity in post-mortem specimens from women aged 78 and 90 years ((Zebaze et al., 2010)) (A) Micrograph of a specimen from a 78-year-old woman. Intracortical porosity is extensive and associated with cortical thinning due to transformation of the inner cortex into a trabecularised structure of cortical remnants. White arrows show areas containing cortical remnants. Cortex adjacent to periosteum (B) appears compact with enlarged pores, but without trabecularisation. (C) The preserved endocortical envelope (shown by arrows) suggests that cortical thinning occurred from within the bone. (D) Micrograph of a specimen from a 90-year-old woman. Cortex is largely porous and looks similar to a sponge.

the status of bone has been investigated for decades. The TOF measurements and pulse-echo techniques are the most common approach. In (ABENDSCHEIN and HYATT, 1972), Abendschein and Hyatt show a well correlation between the mechanical properties and elastically modulus of bovine cortical bone. Evans and Tavakoli has reported a highly significant correlation ($r = 0.85$) between velocity and physical density of bovine femur (Tavakoli and Evans, 1992). Njeh et al. and Bouxsein (Bouxsein and Radloff, 1997) have reported a significant correlation ($r = 0.82$ and 0.71) between ultrasound velocity and ultimate strength of human calcaneus.

There has also been investigated its correlation with established ionizing radiation measurements of BMD, the correlation is weak reported in these investigations due to the other aspects of bone, such as density. The first study of using velocity and BMD to measure the hip fracture is reported in (Heaney, 1989), where it is observed that the velocity in calcaneus is sensitively.

BUA

It has been demonstrated that the attenuation of ultrasound over a frequency of $0.2 - 0.6$ MHz is linear and its slope could be different between normal and osteoporotic subjects. The relationship between BUA and density of cancellous bone samples obtained from cadavers has been reported highly correlated ($r = 0.85$) in (McCloskey et al., 1990). Most applications of evaluating BUA *in vivo* focus on the heel, where the calcaneus is approximately 90% composed of trabecular bone. A number of commercial calcanea BUA systems have been reported significant difference between them ((Njeh et al., 2001)), some of them are shown in Fig. 1.2. The pulse-echo technique has also been applied to the analysis of the BUA in the calcaneus trabecular bone ((Chaffa et al., 2000; Wear, 1999)). It is a rough method based on the selection of the most appropriate time window before analysis of the echoes, this time window being evaluated from a particular depth within the calcaneus. To overcome the influence of multi-path transmission in the proximal femur of complex shape, a model-based estimation of the ultrasound parameters has been developed to evaluate the BUA ((Dencks et al., 2008)). However, the cortical bone, that represents about 80% of the human skeleton, plays an important role in the skeletal bio-mechanical stability ((Bala et al., 2014; Holzer et al., 2009; Zebaze et al., 2010)). (Han et al., 1996; Lakes et al., 1986; Lees and Klopholz, 1992; Sasso et al., 2008) has investigated the BUA of bovine femur cortical bone *in vitro* in the frequency range of $0.3-4.5$ MHz. In plenty previously works ((McCloskey et al., 1990; Prins et al., 2008; Töyräs et al., 2002)), the linear dependence of the measured at-

tenuation with frequency mainly occurs in the frequency range 200 ~ 600 kHz. On the other hand, (Sasso et al., 2008) suggest that the BUA measurements performed around 4MHz are more sensitive to the cortical bone microstructure.



Figure 1.2: Commercial devices incorporating BUA for the assessment of osteoporosis: a) Hologic Sahara (US), b) GE Achilles (US), c) Osteometer DTU-one (DK), d) DMS UBIS-5000 (DR).

Cortical thickness

Since the cortical bone is mainly strength loading part, the thickness of the cortical bone is correlated with the mechanical strength of the bone and the risk of osteoporotic fractures. The thickness of cortical bone layer has been shown to significant correlated ($r = 0.88$) with the fracture load at distal radius (Augat et al., 2009). The thickness of cortical bone can be measured by the pQCT with ionizing radiation. So a cheap, radiation free method to measure the cortical thickness is valuable in clinical application.

Pulse-echo ultrasound measurements for the assessment of cortical bone thickness was proposed in (Wear, 2003) by using autocorrelation and cepstral methods, which are evaluated in human tibia samples and one volunteer, shown in Fig. 1.3(a). Further more, considering the *in vivo* ultrasound signal is more noisier than that obtained *in vitro*, autocorrelation method will exist false peak by the interferences, the envelop and cepstral methods are evaluated in a larger range of samples *in vivo* in (Karjalainen et al., 2008a; Schousboe et al., 2016). The two methods have shown good correlation with the measurements by pQCT with almost same performance. However, the evaluation is based on the whose cortical thickness are distributed in a large range, it's difficult to observed good correlation with pQCT when the cortical thickness is narrowed in smaller range. As we know, human radius cortical shell are more thinner the the tibia's, and with smaller shift at the same time, which proposed a big challenge, caused by seriously overlapping of backscattered echoes, to envelop and cepstral methods. OMP shows promising performance to deal with serious overlapping by dividing the time delays of echoes in smaller interval and reconstructing the echo in each iteration. Firstly, the most correlated column with

residual from the last iteration is been found , it corresponds to an echoes consisted of ultrasound parameters and its index indicates the time delay. So OMP can estimate BUA and Co.Th. indicated by all the ultrasound parameters at the same time in relatively thin cortical bone, such as radius.

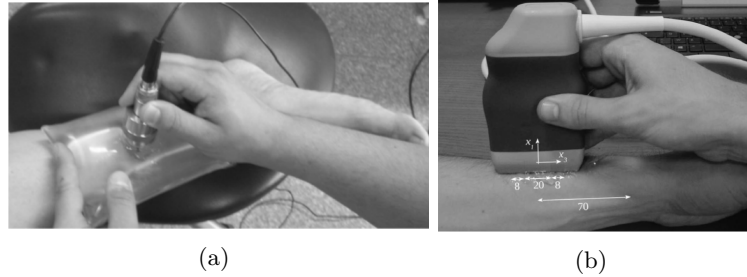


Figure 1.3: a) the first cortical thickness measured by pulse-echo ultrasound (Wear, 2003) b) a device to measure cortical thickness and elastic parameter by guided wave (Vallet et al., 2016)

(Vallet et al., 2016) have used guided wave to estimated the radius cortical thickness by considering the cortical bone as a wave-guide and achieving the dispersion curve , this system can be used to estimate both of the cortical thickness and elastic parameter, which is shown in Fig. 1.3(b).

1.1.2 three model of QUS measurement

There are three different scheme using QUS to measure the cortical bone: Transverse transmission, axis transmission, pulse-echo, which are chosen according to different site of bone and the parameter needed to be measured. The scheme of these measured approaches is shown in Fig. 1.4.

Pulse-echo Ultrasound

The pulse-echo ultrasound is limited used in QUS parameter estimation, since the strong attenuation of bone, especially the trabecular bone. However, it is popular in the estimating the thickness of cortical bone in (Karjalainen et al., 2008a; Schousboe et al., 2016; Wear, 2003), showing a good correlation with the thickness measured by pQCT. And the measured site is limited in tibia cortical bone and radius cortical bone, with a thin soft tissue. However, the pulse-echo ultrasound is very widely used in the industry domain to measure the properties and structure of inspected medium. In this work, through combining with advanced signal processing algorithm, we try to improve the performance of pulse-echo ultrasound

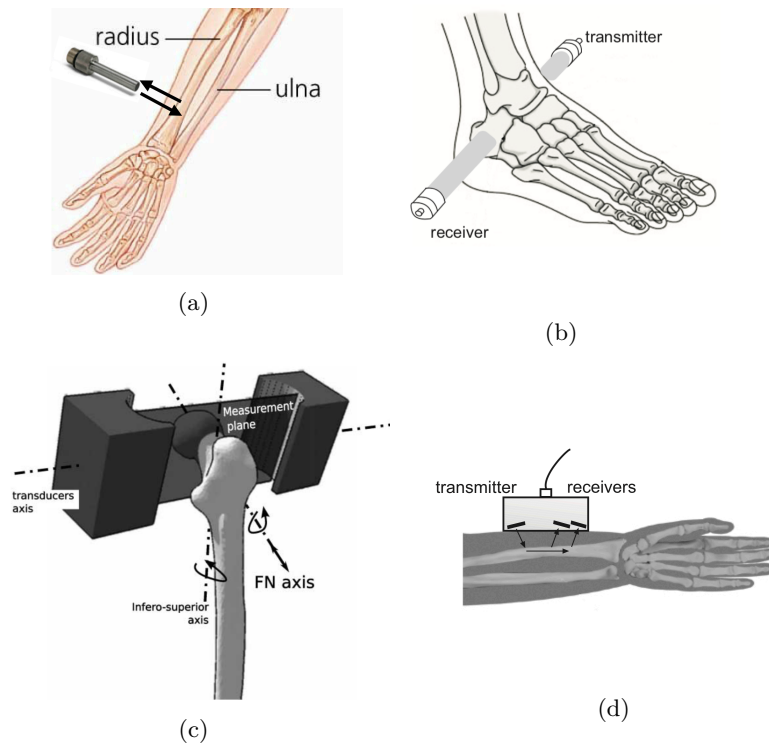


Figure 1.4: a) the Pulse-echo ultrasound, the transmitting and receiving transducers are the same. b) the through-transmission on heel, the transmitting and receiving transducers are located at opposite sides of the target object. c) the transverse transmission on femur neck. d) axial-transmission measurement at the radius.

in accessing the cortical bone. And this the first time we try to use pulse-echo ultrasound to estimate the cortical thickness and BUA at the same time.

Transverse Transmission

Transverse transmission is the most widely use in measuring the SOS, TOF, BUA of bone, since the high contrast and attenuation of bone. varieties of BUA measurement are applied with transverse transmission, (Njeh et al., 2001) has compared six commercial instruments with transmission scheme in BUA measurements. The BUA is usually be applied at the bovine in vivo measurements, since of the bovine is mainly consist of trabecular bone. An important limitation of QUS is the measurement on peripheral skeletal sites, which can provide better hip fracture risk prediction. A QUS scanner has been developed by Barkmann et al (Barkmann et al., 2007) for direct assessment of skeletal properties at the proximal femur. It has been report these transverse-transmission measurements could be used to discriminate the fractures, sharing the same performance with DXA (Barkmann

et al., 2009). In recent research, the transverse transmission through the femur sites consist of two kinds of wave, direct wave and guided wave. The direct wave is through the trabecular bone, and the guided wave acts as a circumferential guided wave when propagating through the cortical bone. The circumferential guided wave has been tested ex-vivo on femurs (Grimal et al., 2013), and indicating that the time-of-flight of the FAS signal revealed a strong relationship with femur strength ($R = 0.79$). And the simulations of ultrasound propagation through the femoral neck has shown its connection with cortical porosity and thickness (Rohde et al., 2014). However, these research of transmission measurements at the proximal femur are performed by a pair of single-element transducers. Array systems can increase the flexibility of such QUS measurements and may enable a better estimation by adjusting for the impact of bone geometry (Rohde et al., 2014).

Axis transmission

Ultrasound axial transmission has been used to measure cortical bone in-vivo for decades. The time-of-flight of the first arriving signal (FAS) was initially used in clinical to evaluate the osteoporotic fracture (Talmant et al., 2009). However, the velocity of FAS depended on various bone properties , eg, cortical thickness, porosity, bone mineral density, and elasticity (Bossy et al., 2004b), and as so for, there isn't sufficient physical interpretation of velocity of FAS connected with osteoporosis and fracture. Furthermore, to measure the FAS velocity with different frequency has been used to enhance the capacity of measuring the cortical bone properties (Egorov et al., 2014; Sarvazyan et al., 2009; Tatarinov et al., 2014). Recently, in some research the cortical bone can be considered as a waveguide for ultrasound (Lefebvre et al., 2002; Moilanen et al., 2003; Protopappas et al., 2007). More specifically, cortical bone is a multi-model waveguide when the ultrasonic range is between 100 kHz and 2 MHz. The frequency-dependent propagation speed of each mode is determined by a specific combination of stiffness coefficients and thickness of the waveguide, which are more specifically for evaluating individual bone qualities. The dispersion curve of cortical bone, compared with appropriate waveguide modeling, can provide effective stiffness coefficients and cortical thickness (Foiret et al., 2012; Lefebvre et al., 2002; Moilanen et al., 2007). The estimation of waveguide thickness and elastic coefficients has been validated on bone mimicking phantoms and on ex-vivo human radius specimens (Foiret et al., 2012). In our laboratory, a novel divided with this method has been developed to measure the cortical thickness and elastic parameter in vivo (Bochud et al., 2017;

Vallet et al., 2016).

1.1.3 the improvement of these thesis in bone parameters estimation

According to the above overview of QUS in ultrasound, it is still room to find a way which carries the balance between the efficiency and conveniency. For the parameters needed to be estimated, the cortical thickness, BUA and elastic parameters of cortical bone are the most important. In the proposed method, the pulse-echo ultrasound is the most simplify system, which only contains one transducer and the computation is very easy, but only give the cortical thickness. The axis transmission with more transducers and carry more complex algorithm can give the cortical thickness and elastic parameters. In the past decades, lots of advanced signal processing algorithms have been developed, such as sparse signal reconstruction, which have not been introduced into ultrasound bone assessment. To introduce the sparse signal processing method into a convenient ultrasound system, which is pulse-echo ultrasound here, to enhance the performance in evaluating cortical bone is the first goal of this thesis.

In the pulse-echo system, the traditional algorithm to estimate the cortical thickness is only using the time delay of different echoes. As we know, the BUA is mainly measured in cancellous bone, giving the BUA of cortical bone will be very significant. If we can obtain more information of backscattered echoes, including time delay, frequency, bandwidth and amplitude which are consisted of the waveform of echoes, the BUA of cortical bone can be calculated meanwhile. The main interest of the pulse-echo mode is that we can neglect the influence of soft tissues, since all the components (and particularly the waves coming from the external and internal boundaries of the cortical shell) travel through the same path of soft tissues. We introduce the sparse signal processing method (Orthogonal Matching Pursuit) to estimate these parameters by building an over-completed dictionary that contains all possible combinations of each parameter sampled in user-defined ranges. The cortical thickness can be estimated by the time delays, and the BUA can be estimated by the rest parameters. We have also illustrated the ability and robustness of the OMP to precisely reconstruct echoes resulting from strong interference and temporal overlapping, as it can be observed in *in vivo* and *in vitro* measurements.

Overall, the combination of OMP and pulse-echo ultrasound provides a powerful and efficient tool to evaluate the BUA and Co.Th. of the cortical bone, with a good resolution and robustness, even in the case of *in vivo* measurements.

1.2 Background of ultrasound imaging in industrial and medical domain

1.2.1 ultrasound tomography

Echography has long been the main first-line imaging technique used to diagnose various pediatric pathologies, Ultrasound reflected tomography (URT) borrows from echography physical concepts (exploitation of scattered echoes) and from X-ray tomography's image formation process (numerical reconstruction from projections). The philosophy of the imaging method is based on a linear approximation (Born approximation) of the inverse scattering problem, and then to formate the final image is a "reconstruction from projections" technique as those used in X-ray computed tomography. The inverse born approximation (Lasaygues et al., 2002; Norton, 1979), allowing to reconstruct small perturbations in a reference medium. For biological tissues with homogeneous properties, this method works straightforward. The background medium can be considered as "constant background", which the Born approximation results in angular scanning with broad-band pulses, allowing one to cover slice-by-slice the spatial frequency spectrum. In this situation, the methods is familiar with X-ray computed tomography.

However, it is not the same solution for bone tissue, since the acoustic impedance of bone is highly contrasted with that of the surrounding medium. There exist wave refraction, attenuation and scattering in wave propagation. And bone is also an elastic medium, this results in the propagation of more complex waves, such as those occurring in elastic volumes (compressional and shear waves). The weak scattering hypothesis in homogeneous medium is therefore not realistic. However, by adopting some assumptions, the field of application of URT can be extended to bone imaging. Several mode of ultrasonic computed tomography is illustrated in Fig. 1.2.1. As we know, when the frequency range of bone QUS is less than 3 MHz, the wavelength of compressional wave (propagating at velocities ranging between 2000 and 4000 m.s^{-1}) in cortical bone is typically greater than 1 mm, which remains much larger than the typical size of bone microstructures, therefore bone itself in the cortical shell can be assimilated to a weakly heterogeneous medium, only compressional

waves are taken into account. So the bone can be assumed as a homogeneous solid cylinder. The born approximation can be used here. P. Lasaygues has proposed a low frequency (< 1 MHz) method in (Lasaygues and Lefebvre, 2002) to image the cross-section of cortical bone. It was implemented by mechanical system: a main symmetric arm holds two transverse arms allowing the parallel translation of two transducers. A 2D-ring antenna with a high frequency (2.25MHz) has been developed later to imaging the cross-section of the cortical bone in (Lasaygues, 2006), allowing for accurate assessment of cortical bone.

An iterative method name Compound Quantitative Ultrasonic Tomography

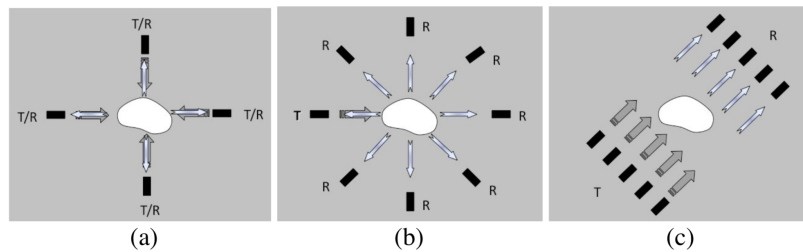


Figure 1.5: Operating modes in Ultrasonic Computed Tomography ((Lasaygues, 2006)). a) a single transducer in reflected mode, b) 2-D ring in the diffraction mode, c) two paired transducers in transmission mode

(CQUT) is proposed in (Lasaygues et al., 2011) based on taking into account the wave refraction at the bone-soft tissue interface, instead of straight rays. This approach consists in performing reflection and transmission measurements, using an iterative correction procedure, which compensates for refraction effect arising at the boundary between bone and the surrounding tissues. The experimental setup was designed to cancel out the refraction effects in order to impose straight ray propagation inside the cortical shell. And the reconstructed algorithm of tomography is base on first order born approximation in each experiment, which the main disadvantage is the heavy computational cost. There is another UCT method based on an iterative algorithm using high-order Born approximations, which is known as Distorted Born Diffraction Tomography (DBDT) (Lu et al., 2016). This strategy is different with CQUT, using iterative numerical steps and performing only one experiment. These two methods has been valid on bone-mimicking phantoms and obtained good estimation of their geometry.

From the presented results implemented on the bone-mimicking phantoms shown in Fig. 1.6, the above methods are not sufficient enough in imaging the geometry of cortical bone, which represents in the following aspect: 1) the CQUT

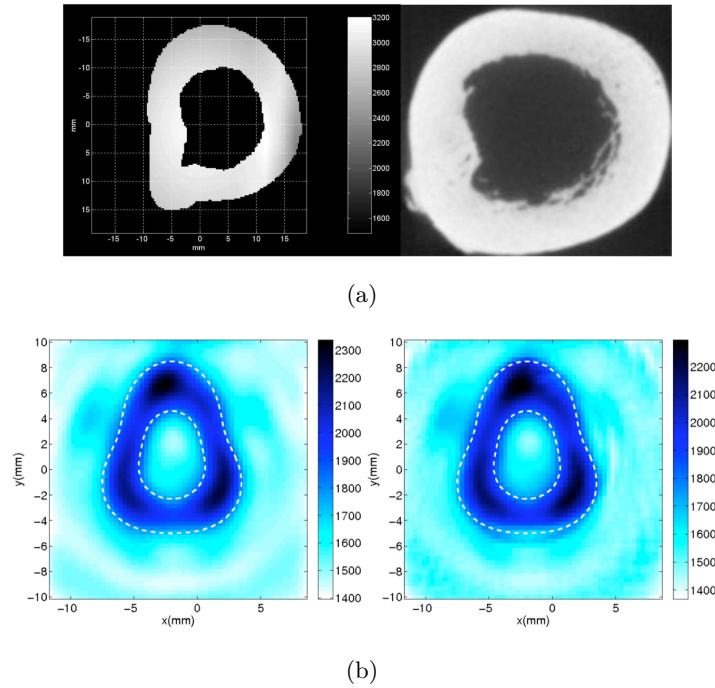


Figure 1.6: a) human thighbone: the left is CQUT image by 90 projections, 128 transducer, the right is corresponding X-ray tomography. b) DBDT image of a bone mimicking phantom, left is initial solution of DBDT at 350kHz, right is iteration at 1MHz ((Lasaygues et al., 2011))

requires multiple experience, 2) all the methods is based on the assumption of considering a fluid-like cavity (like marrow) buried in an elastic hollow cylinder (like bone) surrounded by fluid (like muscle), 3) the boundary of the estimated geometry is very blurry, it will be difficult to distinguish when the cortical thickness is relatively thin.

The main difficulty of bone Ultrasonic computed tomography (USCT) is the large impedance contrast between hard bones and the surrounding soft tissues. In that context, ray-based Born approximation methods commonly used in USCT for imaging of soft tissues ((Li et al., 2009)) do not provide quantitative images. CQUT has been proposed for high-contrast target by iterative procedure can give the quantitative images with a time-consuming iterative procedure, shown in Fig. 1.6. Recently, a Born-based inversion method was proposed to image the internal structure of long bones from reflection data acquired in an axial configuration ((Zheng et al., 2015)), but no quantitative assessment of the wave speed was obtained.

It is difficult to breakthrough in the frame of traditional method, which is based on Born approximation. And the restriction of high frequency applying in cortical bone is also need to be improved.

1.2.2 Full waveform inversion

In the committee of geophysics, Full waveform inversion (FWI), which is used to compute parametric images of the speed of waves inside the Earth, is very popular and well development in recent years. FWI is a nonlinear fitting procedure, which aims to minimize the misfit between recorded and reference seismic data by iterative updating the reference model. Non-linear gradient based optimizations are used in (Ma and Hale, 2012; Ravaut et al., 2004; Sirgue and Pratt, 2004) with complex strategies. (Tarantola, 1984, 1987, 1988), and (Mora, 1988) reduces computational cost significant, thus, increases efficiency of the model parameter estimation. So far FWI has demonstrated its ability to produce high-resolution parameter models, including the velocities of P- and S-waves ((Brossier et al., 2009)), density ((Jeong et al., 2012)), attenuation ((Bai et al., 2013)) and anisotropic parameters ((Operto et al., 2009; Plessix and Rynja, 2012))

Theoretical analyses suggest that FWI includes two modes: tomography and migration ((Mora, 1989)). Conventional acquisition geometries are dominated by reflections. Applying standard FWI on the reflections from this type of data sets is essentially equivalent to carrying out nonlinear least squares migration (e.g., (Wu et al., 2016; Yao and Jakubowicz, 2015)). Thus, the migration mode of FWI dominates the inversion. For only imaging purpose, seismic migration, which are mainly based on approximations to the seismic wave equation, plays a central role in imaging the internal spacial distribution of earth. It is actually the first iteration of FWI. It has been demonstrated in Tarantola (Tarantola, 1984) that the seismic inverse problem can be solved iteratively by numerically calculating the gradient of a waveform misfit function with respect to a set of model parameters. and this gradient can be realized by the integrate between the wavefield of reference model and a wavefield obtained by using time-reversed differences between the data and the current synthetics at all receivers. It is very correlated with the imaging principle, which was proposed by Talagrand and Courtier (COURTIER and TALAGRAN, 1987), a general concept of an ?adjoint? calculation to determine the gradient of a misfit function. Tromp et al. (Tromp et al., 2004) has illustrated the connections between seismic imaging, adjoint methods and time-reversal mirrors. And the introducing of spectral-element method in numerical simulation

provide an opportunity to tackle the full 3D inverse problem.

In the minimizing of misfit function, the introducing of adjoint method simplified the gradient minimizing procedure. The imaging method involves the time-integrated interaction between the current forward wavefield and a second adjoint wavefield generated by using the time-reversed differences between the data and the current synthetics at all the receivers that recorded the signal as simultaneous sources. Thus, the adjoint wavefield can be calculated based upon the same simulation that is used to generate the forward wavefield. The only difference is the source, which is the time reverse of the difference of real received data and forward received data. The contribution of each shot in time serials to the misfit function and its gradient may be calculated once at a time.

In recent years, FWI methods have also started to be applied in ultrasound breast tomography, see e.g. (Sandhu et al., 2015a,b; Wang et al., 2015) and Pérez-Liva et al (Pérez-Liva et al., 2017), as well as shear wave elastography, (Arnal et al., 2013). FWI is used in these contexts to improve the image quality offered by time-of-flight methods, in terms of resolution and contrast. Applications in ultrasonic non-destructive testing also exist (e.g. (Jing et al., 2016; Nguyen and Modrak, 2018)), here we give a numerical example of FWI in NDT shown in Fig. 1.2.2.

1.2.3 Time domain topological energy

In nondestructive testing domain, localization and characterization of defects or obstacles in a fluid or solid elastic medium is still an open problem. Especially, it is very challenge, when the inspected object is heterogeneous and has complex geometry. The DORT (a French acronym for Decomposition of the Time Reversal Operator) relies on the theory of iterative time reversal mirrors which was presented by (Prada et al., 1995). In another committee of mathematical community, the topological gradient approach in shape optimization can also provide an imaging approach. This method has been originated introduced by (Eschenauer et al., 1994), partially generalized by (Sokolowski and Zochowski, 1999) and then developed and extended by (Garreau et al., 2001) to linear elasticity.(Dominguez et al., 2005) develop another extension for the elastodynamic case in non-destructive testing. M. Bonnet has also develop the topological derivative (different name of topological gradient) in acoustic, elastic, anisotropic elasticity (Bonnet, 2006; Bonnet and Delgado, 2013; Guzina and Bonnet, 2004). It has been first developed by (Dominguez et al., 2005) in ultrasonic target detection with time domain topological gradient. The main principle is to minimize a cost

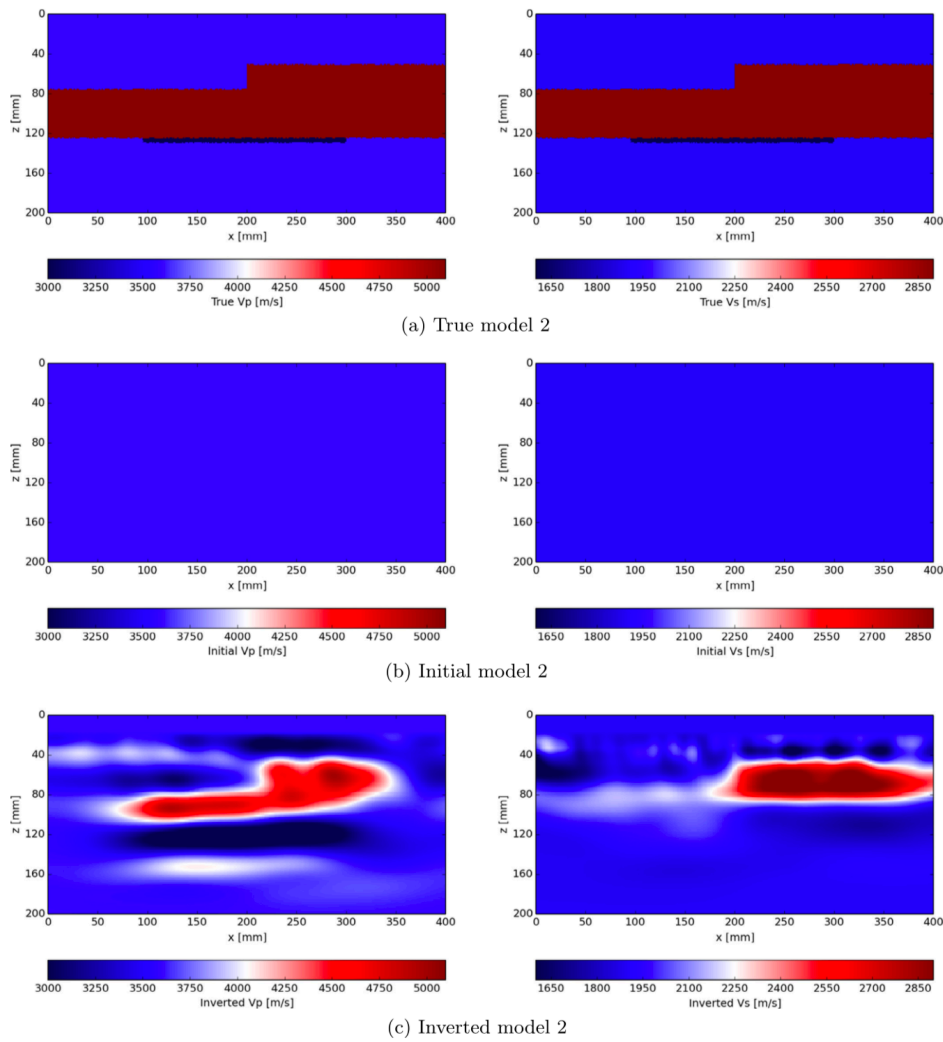


Figure 1.7: An example ((Nguyen and Modrak, 2018)) of quantitative imaging by FWI results of the synthetic test: (a) true model, (b) initial model, (c) inverted model by FWI.

function which evaluates the difference between the measurements obtained for the inspected medium and measurements performed on a reference medium, which shares the familiar principle of migration imaging in geophysics. We will illustrate the connections of the two methods later.

It is assuming a reference medium with known information, a cost function which evaluate the distance between the reference medium and inspected medium by the received waveform. To minimize the cost function is equal to add infinitesimal holes in the reference domain in physically. If we white an asymptotic

expansion of the cost function with respect to the topology of the medium, the first order terms of the asymptotic expansion give the expression of a 'topological gradient'. The topological gradient indicates the direction where to insert the hole in the reference medium could lead to the minimum of cost function. The procedure of imaging is constructed from two fields, which are forward field and adjoint field, in time domain. The forward field is the ultrasonic temporal field in reference medium, and the adjoint field is the time reversal of the difference between the ultrasonic response of the reference medium and the response of the currently inspected medium. Then these two fields are combined through an integration over the acquisition time, in an adequate way, to give rise to the image of the medium. The forward field can be seen as playing the role of a 'photographic developer' spatially intersecting the adjoint field at the focusing times (Dominguez et al., 2005). As a result, the method combines the advantages of a focusing technique, through the adjoint field and the time reversal analogy, and of a spatio-temporal correlation technique due to the developer-like role of the forward field.

Since those formulas of gradient have the common feature to involve a product of two fields in the reference medium, integrated in time from 0 to T, N. Dominguez et al. (Dominguez and Gibiat, 2010) simplify the TDTG to time domain topological energy (TDTE) by simplify the gradient to a waveform integration. Samuel Rodriguez et al. developed a fast topological imaging method (Rodriguez et al., 2012). (Gibiat et al., 2010) developed the wave guided imaging based on TDTE. P. Sahuguet has applied TDTE in biological tissue imagine (Sahuguet et al., 2010).

To have a more intuitive capacity of TDTE, we give an example performed by P. Sahuguet and V. Gibiat (2015), shown in Fig. 1.8. Now, it is clear to see that the analogy between full waveform inversion and time domain topological gradient. They share the same principle, which is to minimize the difference between the reference medium and inspected medium. The difference are presented in following aspects: 1) the TDTG (TDTE) is driven from the optimization of topological, the minimization is by accessing the gradient respected to the shape. 2) the minimization in FWI (migration) is accessing the gradient respected to the model parameters, including density, P-wave and S-wave velocities. As a consequence, the TDTG can only give the structure information and FWI can give the quantitative image, which the distribution of density, P-wave and S-wave velocities.

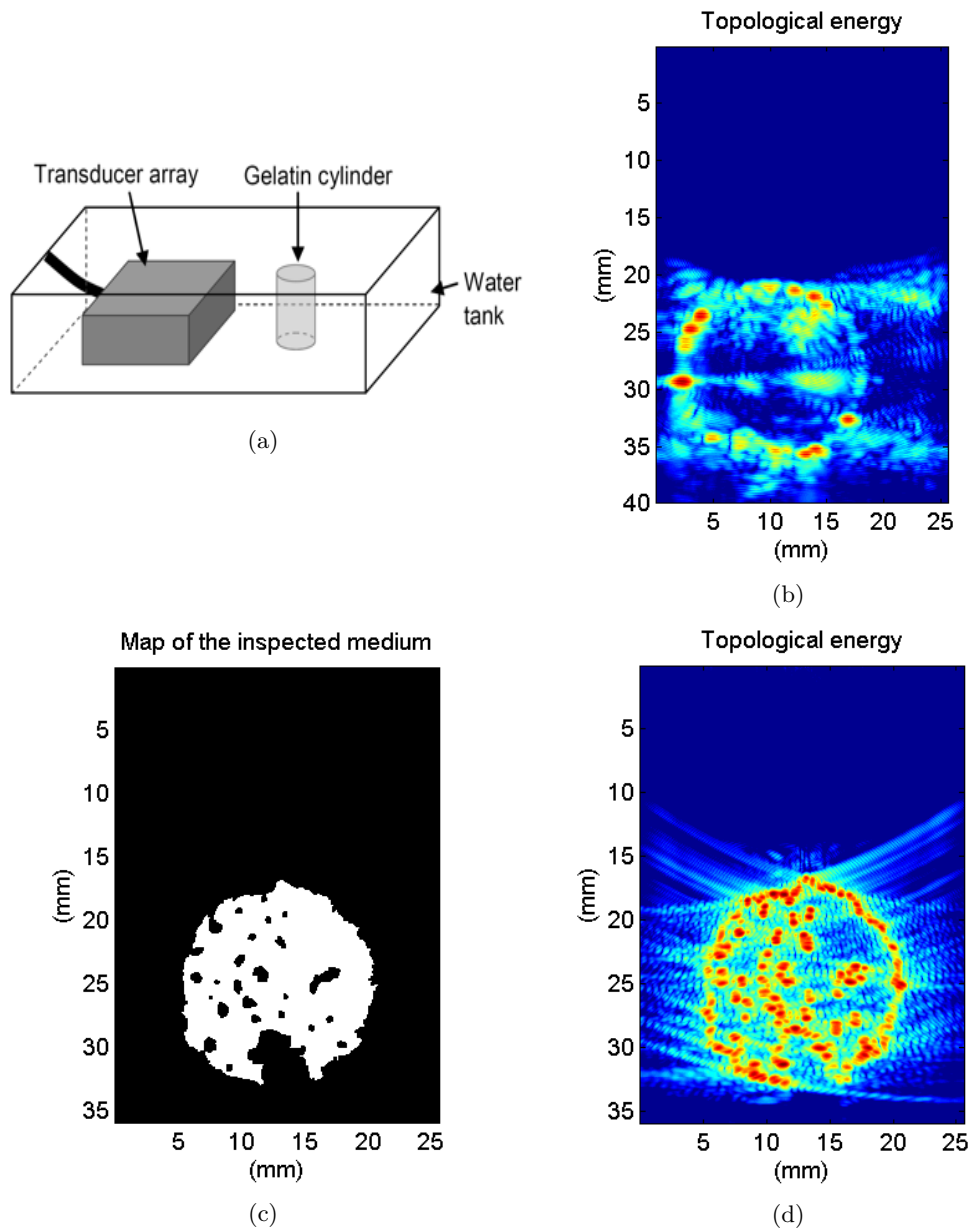


Figure 1.8: (a) Scheme of the experimental setup by P. Sahuguet and V. Gibiat (2015), (b) Resulting topological energy image with a logarithmic scale of 45dB dynamic. (c) Numerical setup of Density map of the inspected medium (in black 1000 kg/m³ and white 1051 kg/m³), (d) Image of the topological energy with a logarithmic scale of 45dB dynamic

1.2.4 The improvement of cortical bone imaging in this thesis

After the above illustration and analysis, the ultrasound tomography, FWI and TDTE shows a promising in cortical bone imaging with the disadvantage of high

computation requirements, since the wave propagation in additional reference medium need to be simulated. The high requirements of computation and appropriate medical application scenarios may be the main obstacles of these kinds of methods applying in medical imaging. The ultrasound tomography based on high-order Born Diffraction Tomography has its limitation in cortical bone imaging on the resolution. In these thesis, we mainly introduce the TDTE and FWI imaging method on cortical bone imaging, and some advanced signal processing methods have been embedded.

The most advantage of TDTE is the high efficiency of obtaining the structure information, since we chose the reference medium as a homogeneous fluid (similar with soft tissue), the displacement of wavefield can be calculated by analytical solution. And TDTE only compute the product of two displacement of wave fields, no wave filed needs to be recorded. These make TDTE if the most efficient way to obtain the structure information.

In the applying TDTE in cortical bone imaging, better resolution of cortical bone requires higher frequency. For high frequency, the internal boundary of cortical bone is difficult to observe. Meanwhile, the internal boundary exist mismatch of position, caused by the velocity mismatch between the reference medium and inspected cortical bone. To deal with the two problems, we proposed two solution: First is TDTE combined sparse signal processing, according to the characters of received signal, we design an efficient over-completed dictionary for OMP, which can successful separate the overlap and locate the time delay accurately in noise, vibration and perturbation. Consequently, the echoes corresponding to the external and internal boundary of cortical bone can be separate. This approach can benefit from the fast computation of one time TDTE with analytical solution, and obtain the internal boundary of cortical bone at same time.

The second approach is iterative TDTE, use the external boundary obtained from the first TDTE as the reference medium, and to run with TDTE again to obtain the internal boundary of cortical bone. In first iteration of TDTE, the reference medium can be considered as only homogeneous fluid. In the second iteration, the reference medium is the the cortical bone material with the shape from the last iteration, surrounding by homogeneous fluid. No analytical solution can be provided to calculate the wave-filed here, the forward and adjoint displacements require numerical simulation and huge storage. The other benefit is the small holes inside the cortical bone can be reconstructed with high frequency,

this is promising in imaging of osteoporosis in cortical bone.

Furthermore, to obtain the distributions of density, P-wave and S-wave velocities of cortical bone, we introduce FWI as well as migration in this thesis, migration, which is only taken the first iteration of FWI, can give us a rough estimation of these distribution, especially in low frequency (the wave-length is closed to cortical thickness). FWI with more iterations can give us more precise distributions of density, P-wave and S-wave velocities. The cortical bone imaging usually include the acoustic part (soft tissue) and elastic part (cortical tissue) in one domain, to reduce the computation, the TDTE can combined with FWI to give the external boundary of cortical bone. Only the elastic domain need to be update in FWI to update distribution of density, P-wave and S-wave velocities of cortical bone. Overall, The TDTE with high frequency can give the clear boundary and small holes inside cortical bones, FWI and migration can give the ultrasound quantitative image of cortical bone.

CHAPTER 2

Sparse signal processing in the evaluation of the cortical bone

Osteoporosis fracture risk prediction is assessed based on clinical factors and, in the standard approach, using dual energy X-ray absorptiometry (DXA) in order to assess bone mineral density (BMD). However, BMD assessed with DXA has strong limitations, in particular it has a lack of sensitivity (Briot and Roux, 2013; Siris, 2004). Cortical bone, the dense tissue that forms the outer shells of the bones, represents about 80% of the human skeleton mass and plays an important role in the skeletal bio-mechanical stability (Bala et al., 2014; Holzer et al., 2009; Zebaze et al., 2010). Aging and osteoporosis are associated with a thinning of the cortical shell (Nishiyama et al., 2009). It follows that including an accurate evaluation of cortical thickness (Co.Th) in skeletal status assessment could improve osteoporosis diagnosis and treatment monitoring. DXA, which provides a projection image of bone can not be used to quantitatively assess cortical bone thickness. High-resolution peripheral computed tomography (HR-pQCT) allows a quantitative analysis of the cortical and trabecular bone compartments with a physical resolution of the order of 100 μ m. It is widely used in clinical research to measure Co.Th at the distal radius and tibia. However this modality will unlikely be used as a widespread diagnostic tool for osteoporosis due to cost issues and ionizing radiations.

Quantitative ultrasound (QUS) approaches have been proposed to measure Co.Th at the radius and tibia such as pulse-echo (Karjalainen et al., 2008b), axial transmission (Moilanen, 2008), and through transmission measurements (Sai et al., 2010). The pulse-echo technique is currently implemented for the clinics with a single transducer (Karjalainen et al., 2018), but can also be used to perform an image of the cortical thickness with a transducer array (Renaud et al., 2018). In that respect, the signal processing of pulse-echo measurement is a topic of interest for the future development of bone QUS. As the ultrasound probe is placed on the skin on top of the bone, echoes can be recorded stemming from the normal-incidence reflection on the soft tissue-bone periosteal interface and bone-medular cavity endosteal interface, i.e., from the two sides of the cortical layer. The times of flight (TOF) of the echoes are recorded and used to calculate Co.Th assuming a certain value of the speed of sound in bone.

Several signal processing approaches have been implemented to retrieve the TOF of echoes *in vivo*. Wear (Wear, 2003) use autocorrelation and cepstral methods, Karjalainen et al. used envelop and cepstral methods (Karjalainen et al., 2008b; Schousboe et al., 2016) and demonstrated a good agreement between Co.Th measured with ultrasound and with HR-pQCT. The range of values of the thickness of the cortical layer (Co.Th) across individuals is typically 1 to 4 mm in radius and 1.5 to 5 mm in tibia (Karjalainen et al., 2008b; Vallet et al., 2016). These dimensions are close to the wavelength of ultrasound in bone which is about 1.7 mm at 2 MHz, a typical frequency used in bone QUS. Although echoes can be measured *in vivo* using slightly higher frequencies, e.g., of 3 MHz (Karjalainen et al., 2018), there is a compromise between a small wavelength and exploitable amplitude of echo from the endosteal surface. Because Co.Th is of the order of the wavelength, temporal overlapping of echoes occurs when measuring thin bones.

Ultrasonic absorption in bone is relatively poorly documented but is known to be related to bone density (Bernard et al., 2015) and could be indicative of the mechanical quality of bone. Ultrasonic absorption in cortical bone can be recovered *in vivo* using guided wave (Minonzio et al., 2011) and pulse-echo techniques (Zheng et al., 2007) through the measurement of broadband ultrasound attenuation (BUA), i.e. the slope of the linear regression of attenuation vs. frequency. The measurement of absorption using multiple echoes may fail in case of signal temporal overlapping. In (Dencks et al., 2008), a model-based signal processing approach was proposed to reconstruct the overlapping echoes, then the BUA can be calculated based on the shift of the central frequency of echoes (Kuc et al., 1976). Signal processing methods dedicated to the measurement of absorption need to be critically assessed with *in vivo* signals.

The Orthogonal Matching Pursuit algorithm (OMP) (Pati et al.), as an efficient sparse signal processing method, provides an accurate waveform parameter estimation. The method uses an over-complete dictionary of Gabor functions associated different combinations of a large range of waveform parameters values. The OMP method searches for the best set of Gabor functions fitting the experimental signal.

The aim of this paper is to introduce a model-based approach to retrieve the TOF and ultrasonic absorption in a pulse-echo configuration. The signal back-scattered from bone is considered to be the superposition of two echo waveforms which are reconstructed using an over-complete dictionary of model signals and the OMP method. The Co.Th calculated from TOFs retrieved *in vivo*

with the technique is compared with reference values obtained from HR-pQCT measurements. The main advantage of this approach is to obtain a precise reconstruction of the waveform of each echo. We also discuss the potential of the technique in case of temporal overlapping.

OMP provides a new perspective for the pulse-echo ultrasound system by estimating all the ultrasound waveform parameters at high frequency as well as low frequency. With these waveform parameters, the cortical thickness can be deduced from the time delay between echoes, and the BUA from the frequency and bandwidth of each individual echo. As far as we know, this is the first application of the OMP approach in reflection for the estimation of the BUA and Co.Th. The basic principle of the experiment is illustrated on Fig. 2.1

Thanks to the simplicity of the OMP approach, it can be expanded in order to separate overlapped echoes in phased array ultrasound imaging, resulting in higher resolution at low frequency.

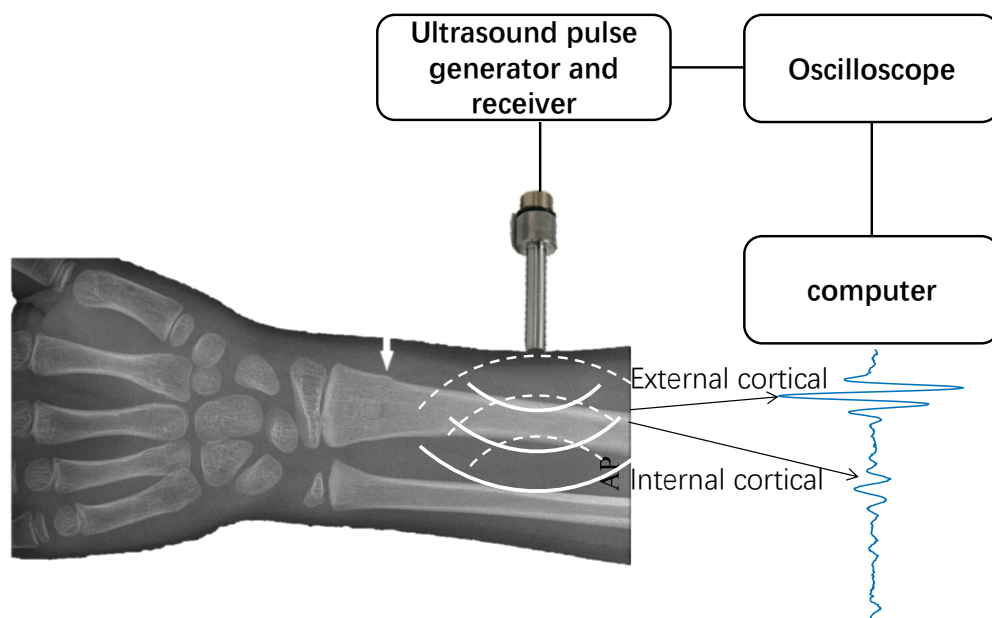


Figure 2.1: principle of the ultrasound pulse-echo measurement to estimate the thickness of the cortical bone

2.1 Sparse signal processing

2.1.1 Signal model

The ultrasonic pulse-echo method aims to characterize the physical properties of the inspected medium in terms of size, location, frequency attenuation. The variation of these parameters between the different echoes and the excitation is related to the properties of medium. For that purpose, a signal model is required to quantify this variation. The excitation can be considered as the input of a linear system, which output is made of the backscattered echoes that are influenced by the medium. This linear system includes the frequency effects of the propagation due to the frequency-dependent absorption and scattering. In the temporal domain, these effects are visible through dispersion, diffraction, phase shift, and attenuation of the original pulse-echo wavelet.

The arrival time of the backscattered echoes can be linked to the location of the target. Furthermore, the time delay between different echoes can be used to estimate the thickness of a layer structure, based on the assumption that the ultrasound velocity is known. The central frequency and bandwidth can be related to the properties of the medium, like the BUA for example. The frequency variations between the emitted and received pulses are due to the frequency-dependent absorption and scattering, which is, in turn, governed by the microstructure of the material

In pulse-echo ultrasound measurements, considering a Gaussian pulse excitation, the received signal of QUS measurements can be modeled in the time domain by superimposed Gaussian pulses. Demirli and Saniie ((Demirli and Saniie, 2001)) have introduced this model for echoes from a flat reflector, and Dencks *et al.* ((Dencks et al., 2008)) have successfully introduced this model for transmission measurements at the proximal femur.

Since Gabor functions (product of a Gaussian function with a complex sinusoid, characterized by time, frequency, and scale) are qualitatively and quantitatively very similar to the expected ultrasonic echoes, Matching Pursuit with Gabor functions has been frequently used to identify echoes in a wide range of ultrasonic signals in the domain of Non Destructive Evaluation (NDE) as well as structural health monitoring applications. Hong *et al.* ((Hong et al., 2005)) use this method for damage inspection with guided waves. Ruiz-Reyes *et al.* ((Ruiz-Reyes et al., 2006)) apply it to enhance echoes in scattered ultrasonic waves. Lu and Michaels ((Lu and

Michaels, 2007)) show the ability and efficiency of the Matching Pursuit method to identify separated and overlapped echoes from ultrasonic signals with reverberation. We use the following model (Gabor function) for the received signal

$$y(t) = \Re\left\{\sum_{i=1}^P A_i \exp[-s_i(t - \tau_i)^2] \exp[j2\pi f_i(t - \tau_i)]\right\} + n(t) \quad (2.1)$$

where $\Re\{\}$ is the real operator, P is the number of echoes, s_i denotes the bandwidth factor, f_i the central frequency, τ_i the group delay and A_i the amplitude of i -th echo. In this expression, $n(t)$ stands for the error between the model and the measured signal, including noise.

2.1.2 Dictionary

To implement the sparse signal processing method, the first issue is to discretize the Gabor function into an over-complete dictionary \mathbf{D} , where the columns are built resorting to the Gabor function basis

$$\mathbf{d}(\Theta, t) = \zeta_{\Theta} \exp[-s(t - \tau)^2] \exp[j2\pi f(t - \tau)] \quad (2.2)$$

$$\Theta = [s, \tau, f], \quad (2.3)$$

where ζ_{Θ} is a normalization parameter that ensures $\|\mathbf{d}(\Theta, t)\|_2 = 1$ (l_2 -norm). To build a suitable elementary atom of \mathbf{D} , the columns use a discretization of the different parameters that characterize each Gabor function. The possible values of the set of parameters Θ are sampled on M discrete points. For this purpose, we define an *a priori* pertinent range for s , τ and f , these ranges being subdivided into L , S and K regular intervals, respectively. And each Gabor function is sampled at N discrete times $\mathbf{t} = [t_1, t_2, \dots, t_N]$. Thus the dimension of the over-complete dictionary is $M = L \times S \times K$, with $M \gg N$. The dictionary can be represented as

$$\begin{bmatrix} y_1 \\ y_2 \\ \vdots \\ y_N \end{bmatrix} \mathbf{D} = \begin{bmatrix} d(\Theta_1, t_1) & d(\Theta_2, t_1) & \cdots & d(\Theta_M, t_1) \\ d(\Theta_1, t_2) & d(\Theta_2, t_2) & \cdots & d(\Theta_M, t_2) \\ \vdots & \vdots & \ddots & \vdots \\ d(\Theta_1, t_N) & d(\Theta_2, t_N) & \cdots & d(\Theta_M, t_N) \end{bmatrix} \begin{bmatrix} x_1 \\ x_2 \\ \vdots \\ x_M \end{bmatrix} \quad (2.4)$$

where

$$\begin{aligned} \Theta_m &= [s_l, \tau_s, f_k], \\ l &\in [1, L], s \in [1, S], k \in [1, K], m \in [1, M] \end{aligned}$$

The ranges of variations of s , τ and k are defined as follows. The range of frequency f can be obtained by choosing a portion of the largest peak in the spectrum of the received signal, as discussed in (Mor et al., 2010). Similarly, the range for the bandwidth factor s can be deduced from the bandwidth of the emitted signal. The time delays τ of the different echoes are searched around the peaks of the envelop of the received signal (obtained by Hilbert transform of the corresponding analytic signal). Overall, the selection of the parameter intervals is quite flexible due to the robustness and efficiency of the OMP method.

We evaluated the numerical cost of the OMP algorithm. For a dictionary size varying from 1000 ($N = 1000$) \times 50000 ($L = 20, K = 10, S = 250$) to 1000 ($N = 1000$) \times 80000 ($L = 20, K = 10, S = 400$), the computation time of OMP is approximatively 0.2 \sim 0.7s on a standard personal computer (Intel(R) Xeon(R) CPU E5-2620 v2 at 2.10GHz, 32Gbytes memory).

It is now important to determine the pertinent intervals for each of the three above parameters. The frequency range can be obtained by choosing a portion of the largest peak in the spectrum of the received signal, as discussed in (Mor et al., 2010). Similarly, the range for the bandwidth factor α can be deduced from the bandwidth of the emitted signal. The time delays of the different echoes are searched around the peaks of the envelop of the received signal (obtained by Hilbert transform of the corresponding analytic signal). Overall, the selection of the parameter intervals is quite flexible due to the robustness and efficiency of the OMP method.

2.1.3 Orthogonal Matching Pursuit

The Orthogonal Matching Pursuit (OMP, (Sahoo and Makur, 2015)) and Basis Pursuit (BP, (Chen and Donoho)) are two well-known recovery algorithms in compressed sensing and sparse signal recovery. OMP can recover a high-dimensional sparse signal based on a small number of noisy linear measurements. Besides OMP, there are several algorithms to solve sparse signal recovery: Sparse Bayesian Learning (SBL, (Wipf and Rao, 2004)(Zhang and Rao, 2011)) and FOCUSS ((Gorodnitsky and Rao, 1997)). OMP is an iterative greedy algorithm that selects at each step the column of the dictionary that is mostly correlated with the current residuals. Compared to BP, OMP is a more appealing algorithm due to its greater execution speed ((Sahoo and Makur, 2015)). In the next paragraphs, we give a brief introduction of the main principles of OMP.

We consider the above signal model (2.2) and assume that the measured signal $\mathbf{y} \in \mathbb{R}^N$ is a K -sparse signal: this means that we approximate the real signal $y(t)$ as the sum of K elementary basis functions from the dictionary. Thus, the objective of the algorithm is to determine the most suitable K -sparsity from the over-completed dictionary \mathbf{D} . It is a so-called ill-posed inverse problem when the dimension $N \ll M$. To solve this problem, there is an *a priori* condition, called Mutual Incoherence Property (MIP), introduced in Donoho and Huo ((Donoho and Huo, 2001)):

$$\mu = \max_{i,j} | \langle \mathbf{d}_i, \mathbf{d}_j \rangle | \quad (2.5)$$

where \mathbf{d}_i and \mathbf{d}_j are two different columns of \mathbf{D} . This coefficient μ can be interpreted as a measure of the decorrelation between the different columns of \mathbf{D} : if two columns are too much similar, μ can be near 1. Otherwise, a small value of μ implies that all pairs of columns are significantly decorrelated.

The MIP condition requires that the incoherence parameter μ is small enough to ensure a unique solution for \mathbf{x} . It has been reported in ((Tromp et al., 2004)) that $\mu \leq \frac{1}{2K-1}$ is a sufficient condition for an precise recovery in the absence of noise.

In particular, it is known that the l_1 norm minimization provides an effective way for reconstructing a sparse signal. In this case, the error results from noise and disturbance, and we finally prefer the l_2 norm constraint. Thus the problem can be illustrated as follows:

$$\hat{\mathbf{x}} = \min_{\mathbf{x}} \left\{ \frac{1}{2} \|\mathbf{y} - \mathbf{D}\mathbf{x}\|_2^2 + \lambda \|\mathbf{x}\|_1 \right\} \quad (2.6)$$

In the context of cortical bone measurement, the received signal contains two main echoes, respectively reflected by the external and internal boundaries of the bone. The precise evaluation of the cortical thickness requires that these two main echoes are recovered accurately, such that we are mainly interested in the two dominant components of \mathbf{x} . There are two different versions of the OMP, the first one is error-constrained, and the second one sparsity-constrained. In our application, the optimal sparsity is equal to 2, which are corresponding to the echo from external and internal boundary of cortical bone. So, we prefer the K -sparsity constrained version of OMP. Finally, the different steps of the OMP process are summarized in Algorithm 1.

Steps #4, #6 and #7 correspond to the main structure of the OMP algorithm. The first step consists in finding the column of \mathbf{D} that is mostly correlated with the current residual, this column is then added to the support set. The extracted coefficients are updated by computing the orthogonal projection of the signal on

the elements of the support set. This process provides better results than standard MP. It is important to observe that the current residual is always orthogonal to all the elements of the support set. Therefore, the algorithm always selects a new atom at each step.

Algorithm 1 Orthogonal Matching Pursuit algorithm

Input: $\mathbf{y} \in \mathbb{R}^N$, Dictionary $\mathbf{D} \in \mathbb{R}^{N \times M}$, target sparsity K

Output: sparse solution $\mathbf{x} \in \mathbb{R}^M$

- 1: construct \mathbf{D} with different time delays of emitted signal
 - 2: Set $I = ()$, $\mathbf{r} = \mathbf{y}$
 - 3: **while** true **do**
 - 4: $\hat{i} = \arg \max_i |\mathbf{D}(:, i)^T \mathbf{r}|$
 - 5: $\mathbf{I} = (\mathbf{I}, \hat{i})$
 - 6: $\mathbf{x}(I) = \mathbf{D}(:, I)^\dagger \mathbf{y}$
 - 7: $\mathbf{r} = \mathbf{y} - \mathbf{D}(:, I)\mathbf{x}(I)$
 - 8: **if** $\varepsilon \leq \text{threshold}$ and $\|\mathbf{x}\|_0 = K$ **then**
 - 9: break
 - 10: **end if**
 - 11: **end while**
-

2.1.4 Adapted Orthogonal Matching Pursuit

Since the columns of the dictionary defined in (2.4) are complex-valued, the corresponding steps of the OMP have to be adapted. The first step consists in searching the most matching column with the residual from the previous iteration. In the case of a complex dictionary, the matching between a particular complex column and the given signal can be found in (Lu and Michaels, 2008) as

$$\langle \mathbf{r}, \mathbf{d}^H(t) \rangle = \mathbf{d}^H \mathbf{r} = C e^{i\phi} \tag{2.7}$$

where \mathbf{r} is the residual from the previous iteration, H denotes the complex conjugate transpose operator, C indicates the matching level and ϕ is the phase of the given signal.

In the particular case of strong overlapping of echoes caused by the unknown multi-scatters (*in vivo*) or too thin cortical thickness, as illustrated in Fig. 1.1.1. To

identify the main echoes, a matching time interval contained the main echo should be defined. The derivation of the envelop can provide further information to locate the time interval, of which derivation is equal to zero. A circumstance is illustrated in Fig. 2.2, eq. (2.7) is used instead

$$\langle \mathbf{r}, \mathbf{d}^H \rangle = \mathbf{d}^H(t_1 : t_2) \mathbf{r}(t_1 : t_2) = C e^{j\phi} \quad (2.8)$$

where the match procedure is limited in a time interval $[t_1, t_2]$ which only contains the waveform of main echo, as shown in Fig. 1.1.1. This can avoid OMP processing two overlapping echoes as a single one in the matching step.

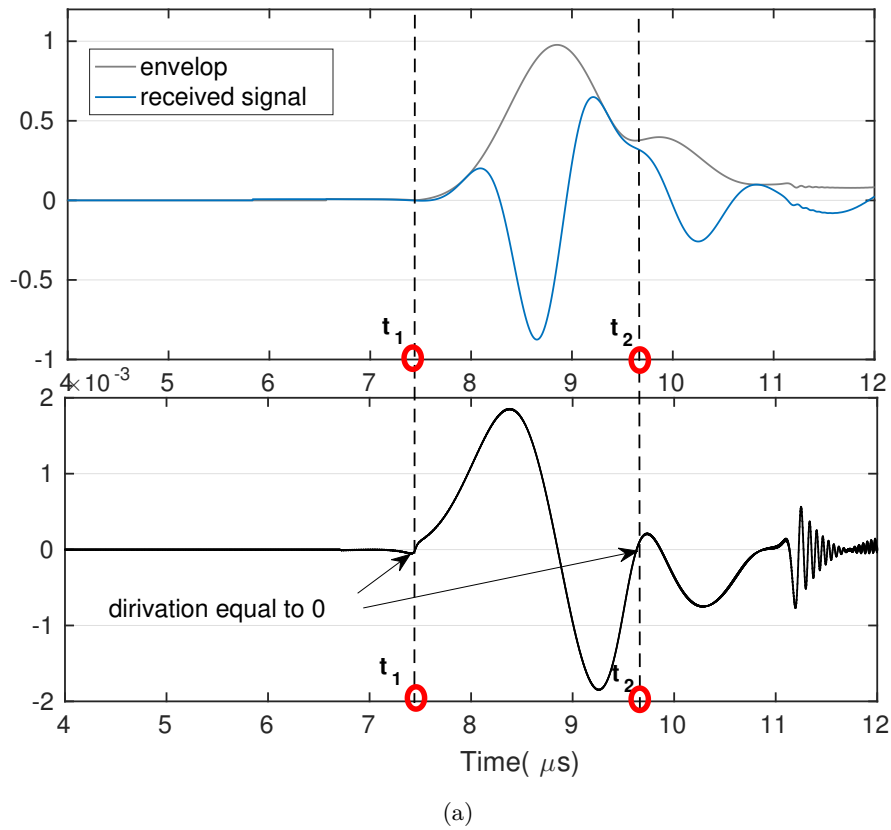


Figure 2.2: OMP for strong overlapping case: up: the received signal from simulation and its envelop, down: derivation of the envelop and its correspond time matching interval

The best correlated column from the dictionary \mathbf{D} corresponds to the largest value of $|C|$, where $|\cdot|$ denotes the modulus. The corresponding position index in vector \mathbf{x} is denoted

$$i_{max} = \max_i \{ |\mathbf{D}(:, i)^H \mathbf{r}| \}. \quad (2.9)$$

and the phase is given by

$$\phi = \text{angle}\{\mathbf{D}(:, i_{max})^H \mathbf{r}\}. \quad (2.10)$$

It should be noticed that the residual can not be iterated directly, since it is defined as the linear combination of two real Gaussian pulses instead of complex-values Gabor functions as introduced in (2.1). After computation of (2.9) and (2.10), we can return to the real Gaussian pulses $\mathbf{D}_r(i_{max})$ by the relationship

$$\mathbf{D}_r(:, i_{max}) = \Re\{\mathbf{D}(:, i_{max})e^{-i\phi}\}. \quad (2.11)$$

The adapted OMP is illustrated in Algorithm 2.

Algorithm 2 Adapted Orthogonal Matching Pursuit algorithm

Input: $\mathbf{y} \in \mathbb{R}^N$, $\mathbf{D} \in \mathbb{R}^{N \times M}$, target sparsity=2

Output: sparse solution $\mathbf{x} \in \mathbb{R}^M$

- 1: Set $I = ()$, $\mathbf{r} = \mathbf{y}$
 - 2: **for** target sparsity **do**
 - 3: $i_{max} = \max_i |\mathbf{D}(:, i)^H \mathbf{r}|$
 - 4: $\mathbf{I} = (\mathbf{I}, i_{max})$
 - 5: $\phi = \text{angle}\{\langle \mathbf{r}, \mathbf{D}(:, i_{max})^H \rangle\}$
 - 6: $\mathbf{D}_r(:, i_{max}) = \Re\{\mathbf{D}(:, i_{max})e^{-i\phi}\}$
 - 7: $\mathbf{x}(I) = \mathbf{D}_r(:, I)^\dagger \mathbf{y}$
 - 8: $\mathbf{r} = \mathbf{y} - \mathbf{D}_r(:, I)\mathbf{x}(I)$
 - 9: **end for**
-

2.2 Estimation of the Cortical Thickness and Broad-band Ultrasound Attenuation

Pulse-echo ultrasound measurements for the assessment of the cortical bone thickness are proposed in (Wear, 2003) by using autocorrelation and cepstral methods, which are evaluated with human tibia samples and one volunteer. As *in vivo* ultrasound signals are usually more noisy than *in vitro* signals, the autocorrelation method may exhibit false peaks. Also, in (Karjalainen et al., 2008a) (Schousboe et al., 2016), the envelop and cepstral methods are evaluated on a large range of thickness for the *in vivo* samples. The two methods show a good correlation with

the measurements obtained by pQCT, with almost same performance. However, if we reduce the range of possible cortical thicknesses, it is observed that the correlation with pQCT decreases. As we know, human radius cortical shell has a smaller thickness than tibia, therefore resulting in a smaller time delay between the two main echoes. This is a quite important challenge for envelop and cepstral methods, due to the strong overlapping effect of backscattered echoes. The OMP algorithm appears as a promising tool in such situation, by dividing the time delays between echoes in smaller intervals and performing an iterative reconstruction of the signal. The algorithm first determines the most correlated column with the residual from the last iteration. This column is associated with a unique set of possible ultrasound parameters from the sampling used to build the dictionary (time-delay, frequency and bandwidth). It results therefore that OMP can estimate the BUA and Co.Th., even in the particular case of the thin cortical bone, such as radius. This sparse method to estimate the ultrasound parameters of the cortical bonet, BUA and Co.Th., will be evaluated *in vivo* and *ex vivo*.

After the completion of OMP, two Gabor functions matching the two echoes from the external and internal bone boundaries are characterized. In particular τ_1 and τ_2 denote the time delays and f_1 and f_2 denote the central frequency of the two echoes. The Co.Th. is obtained by following equation

$$\text{Co.Th.} = \text{SOS} \cdot \frac{\tau_2 - \tau_1}{2} \tag{2.12}$$

where SOS is the speed of sound which is assumed to be a constant (Grimal and Laugier, 2019; Karjalainen et al., 2008b).

In appendix, we will formally illustrate the advantages of *in vivo* BUA evaluation in reflection configuration, compared to transmission configuration. In most published studies ((McCloskey et al., 1990; Prins et al., 1998; Töyräs et al., 2002)), BUA was measured in the frequency range 200 ~ 600 KHz. On the other hand, (Sasso et al., 2008) suggest that the BUA measurements performed around 4MHz are more sensitive to the cortical bone microstructure.

The BUA parameter is obtained from the slope of the frequency-dependent attenuation ratio between the amplitude response of the received signal and the reference signal within a characteristic frequency range of 200 ~ 600 kHz, using a logarithmic scale. Traditional *in vivo* BUA measurements are mainly performed in transmission through the heel, where the calcaneus is approximately 90% composed of trabecular bone.

In the next paragraph, we formally illustrate in what sense the BUA evaluation can be more efficient in reflection than in transmission, as illustrated on Fig. 2.3.

For the *in vivo* measurement of the BUA through the heel in transmission, the

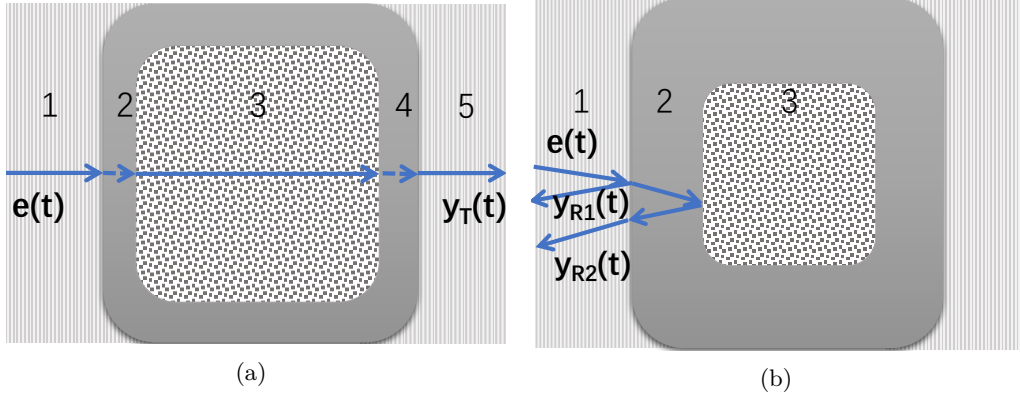


Figure 2.3: (a) measurement of the BUA in transmission: 1 and 5 correspond to soft tissues, 2 and 4 to the cortical bone and 3 to the trabecular bone (b) measurement of the BUA in reflection

influence of the cortical bone is usually considered as negligible, and the received signal can be formally written in the frequency domain as follows:

$$\tilde{y}_T(f) \propto T_{13}T_{35}\tilde{e}(f)\tilde{H}_1(f)\tilde{H}_3(f)\tilde{H}_5(f) \quad (2.13)$$

$$\left| \frac{\tilde{y}_T(f)}{\tilde{e}(f)} \right| \propto T_{13}T_{35}|\tilde{H}_1(f)| \times |\tilde{H}_3(f)| \times |\tilde{H}_5(f)| \quad (2.14)$$

where T_{ij} represents the transmission coefficient from medium i to j and $\tilde{H}_i(f)$ the transmission function (propagation) of medium i . If the influence of the cortical thickness 2 and 4 is effectively negligible, T_{13} and T_{35} do not depend on frequency and describe the transmission between two propagation media, involving the mechanical parameters (density and ultrasound velocities) of each layer.

Using the reflection mode to measure the BUA, the received signal $y_T(t)$ is now replaced by the echo coming from the internal cortical boundary $y_{R2}(t)$, while the reference signal is now the echo coming from the external cortical boundary $y_{R1}(t)$. This new measurement protocol can be formally described as follows:

$$\tilde{y}_{R1}(f) \propto \tilde{e}(f)\tilde{R}_{12}\tilde{H}_1(f)^2 \quad (2.15)$$

$$\tilde{y}_{R2}(f) \propto \tilde{e}(f)T_{12}R_{23}T_{21}\tilde{H}_1(f)^2\tilde{H}_2(f)^2 \quad (2.16)$$

$$\left| \frac{\tilde{y}_{R2}(f)}{\tilde{y}_{R1}(f)} \right| \propto \frac{T_{12}R_{23}T_{21}}{R_{12}}|\tilde{H}_2(f)|^2 \quad (2.17)$$

2.3. Numerical simulation of the OMP in the cortical bone assessment

where R_{ij} is the reflection coefficient in medium i at the interface between medium i and medium j . Here, the transfer functions describing the propagation $\tilde{H}_1(f)$ and $\tilde{H}_2(f)$ are squared because the wave travels each medium twice. If we compare the two formal models, we observe that the calculated ratio only depends on the bone characteristics in reflection, while an additional term appears in transmission, corresponding to perturbations induced by soft tissues. Consequently, we can expect a better determination of the BUA in reflection than in transmission.

In plenty previously works ((McCloskey et al., 1990; Prins et al., 2008; Töyräs et al., 2002)), the linear dependence of the measured attenuation with frequency mainly occurs in the frequency range 200 ~ 600 kHz. On the other hand, (Sasso et al., 2008) suggest that the BUA measurements performed around 4MHz are more sensitive to the cortical bone microstructure. Also, it is of course easier to separate the echoes at higher frequency.

In this study we used pulse centered at 3.5 MHz and the parametric BUA estimation proposed by (Kuc et al., 1976). This method assumes that the attenuation in the propagation medium varies linearly with frequency such that the relative bandwidth remains unchanged. It follows that BUA can be estimated from the shift of the center frequency of the Gaussian pulse. This parametric estimation is well adapted in both transmission and reflection, (Dencks et al., 2008) have successfully applied this method to evaluate the BUA in transmission in *in vitro* measurements. In reflection, the parametric estimation of the nBUA (normalized BUA, which is the BUA divided by distance of wave propagation) can be written as

$$\text{nBUA} = -17.4 \cdot \frac{\pi^2}{2\text{Co.Th.} \cdot s_1} \cdot (f_2 - f_1) \quad (2.18)$$

where s_1 denotes the bandwidth of the echo reflected by the external boundary of the cortical bone, f_1 and f_2 are the central frequencies of the echoes from the external and internal boundaries, respectively. It should be noted that the nBUA is divided by two times of cortical thickness, which is the distance of wave propagating.

2.3 Numerical simulation of the OMP in the cortical bone assessment

2.3.1 2D numerical simulation

To evaluate the performance OMP for the evaluation of cortical bone thickness, a 2D numerical simulation has been performed with a Finite-Difference Time-Domain

(FDTD) numerical scheme implemented in SimSonic2D (Bossy et al., 2004a,b). We simulated the propagation of an ultrasonic pulse in a plate of bone material immersed in water, shown in Fig. 2.4. The parameters considered for these simulations are summarized in Table 2.1 (Foiret et al., 2014). A mono-element transducer (size: 1.5mm, 100% -6dB bandwidth) emits a Gaussian pulse and records the reflected echoes. The central frequency of Gaussian pulse was chosen as $\{0.5, 0.75, 1, 2, 4\}$ Mhz to reach the corresponding ratio Co.Th./ λ relevant for cortical bone is $\{0.25, 0.38, 0.5, 1, 2\}$. The grid step of simulation field is 0.025 mm, which corresponds to $\lambda_w/60$ (λ_w is the wavelength in water).

Table 2.1: Properties of sawbone used in the numerical simulation and water. L and T stand for longitudinal and transverse waves

	Co.Th. (mm)	v_L (mm/ μ s)	v_T (mm/ μ s)	density (g/cm ³)
water		1.5	0	1.0
bone	2	4	1.8	1.85

The precision of estimated Co.Th. according to (2.12) is shown in Fig. 2.5(a) under different ratio thickness/wavelength. Looking at this figure, we observe that OMP reaches a $\geq 95\%$ precision as long as the ratio thickness/wavelength is larger than 0.38. The corresponding Mean Square Error (MSE) between the received and reconstructed signals is shown in Fig. 2.5(b). Here we illustrate the overlapping case, which the ratio Co.Th./ λ is 0.25 and 0.38. It can be observed that the ratio 0.35 is the limitation in Fig. 2.6. Without attenuation in this simulation, the nBUA suppose to be zero.

2.3.2 Application of OMP in imaging with a phased array transducer

The OMP can be also applied to ultrasound imaging to increase the resolution. Once the different echoes have been separated by determination of the time delays, the received signal can be reconstructed by increasing the frequency. To perform a numerical simulation, a 64 elements transducer array is placed in front of a tube of bone-mimicking material, as described in Table 2.1. The signals, received by the 64 channels after reflection by the tube, is shown on Fig. 2.7(a). In this simulation we have considered a plane wave illumination. The OMP algorithm, applied on these signals, allows to evaluate the temporal delay between the different echoes.

2.3. Numerical simulation of the OMP in the cortical bone assessment 17

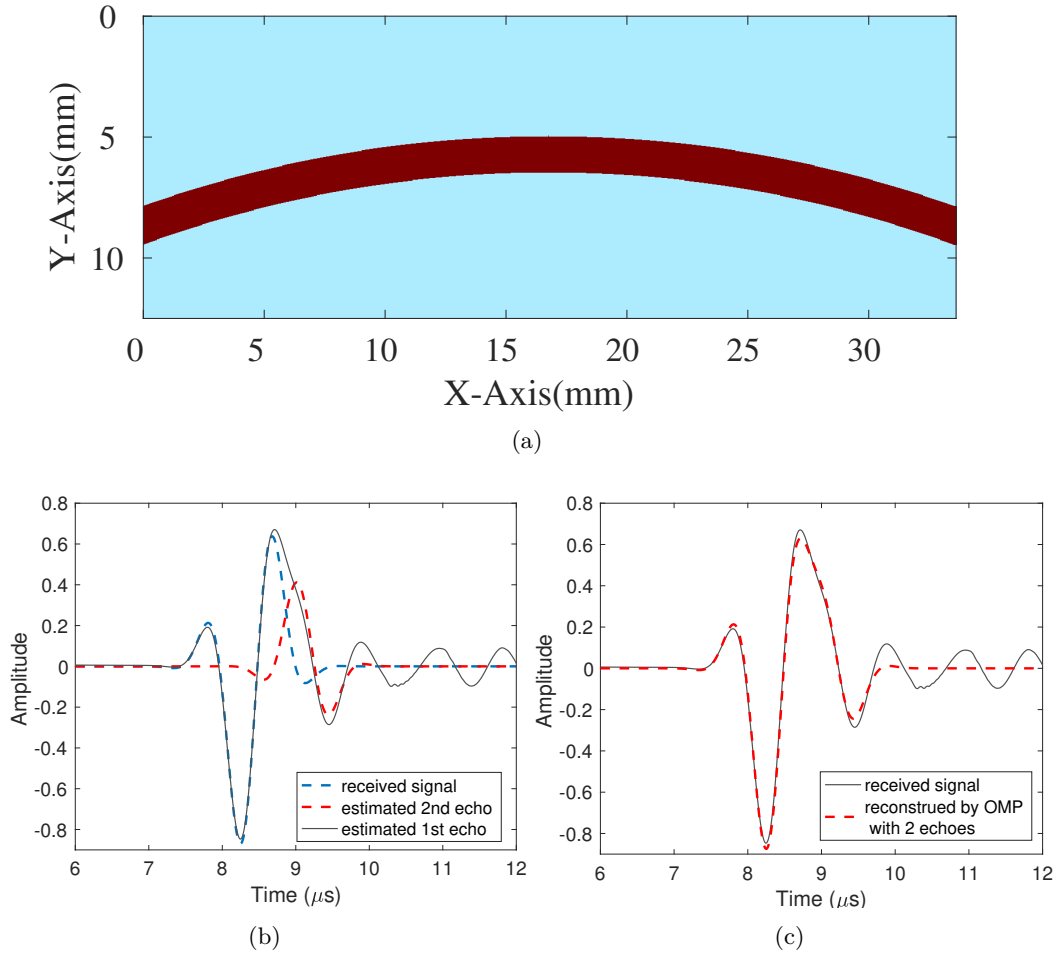


Figure 2.4: (a) the numerical map of a tube with sawbone-equivalent material immersed in water, (b) the received signal when the frequency is 1MHz (c) its reconstruction by OMP

Then we can simulate the reconstructed signal from a 3MHz Gaussian pulse with the same time delays, as shown on Fig. 2.7(b), and the two echoes are now well separated in space and time. Meanwhile, the second echo from the internal boundary of the tube (or cortical bone in a real experiment) is usually highly attenuated, it can be enhanced in the reconstruction. To validate the accuracy, the same simulation is run, using now a plane wave with a 3MHz Gaussian pulse. The obtained signals are shown on Fig. 2.7(c). On Fig. 2.7(d), we have superposed the time delays calculated by OMP and the reflected signals from the 3MHz excitation. This figure illustrates a good correspondence.

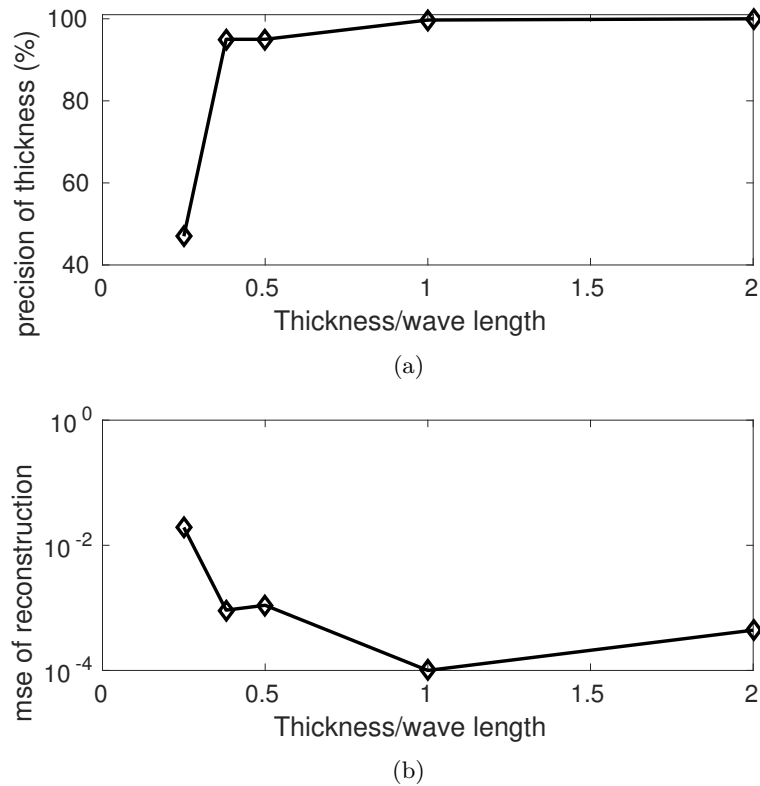


Figure 2.5: (a) mean square error of the reconstructed signal for different values of the ratio thickness/wavelength (b) estimated thickness precision in percentage

The successful separation of overlapped components in the reflected signals provides makes this process an interesting tool in ultrasound cortical bone imaging, and ensure that the ultrasound imaging of thin cortical bone is possible, like at the femoral neck or radius. It can also be used in other medical and industrial domains to image layer-based structured.

2.4 Experimental validation

The OMP in pulse-echo ultrasound to evaluate the Co.Th. and the BUA has been validated experimentally with plane plates of sawbone, and real bones (*ex-vivo* and *in vivo*).

2.4.1 The sawbone plates

The bone-mimicking material used in this experiment is a transverse isotropic composite made of short glass fibers embedded in an epoxy matrix (Sawbone,

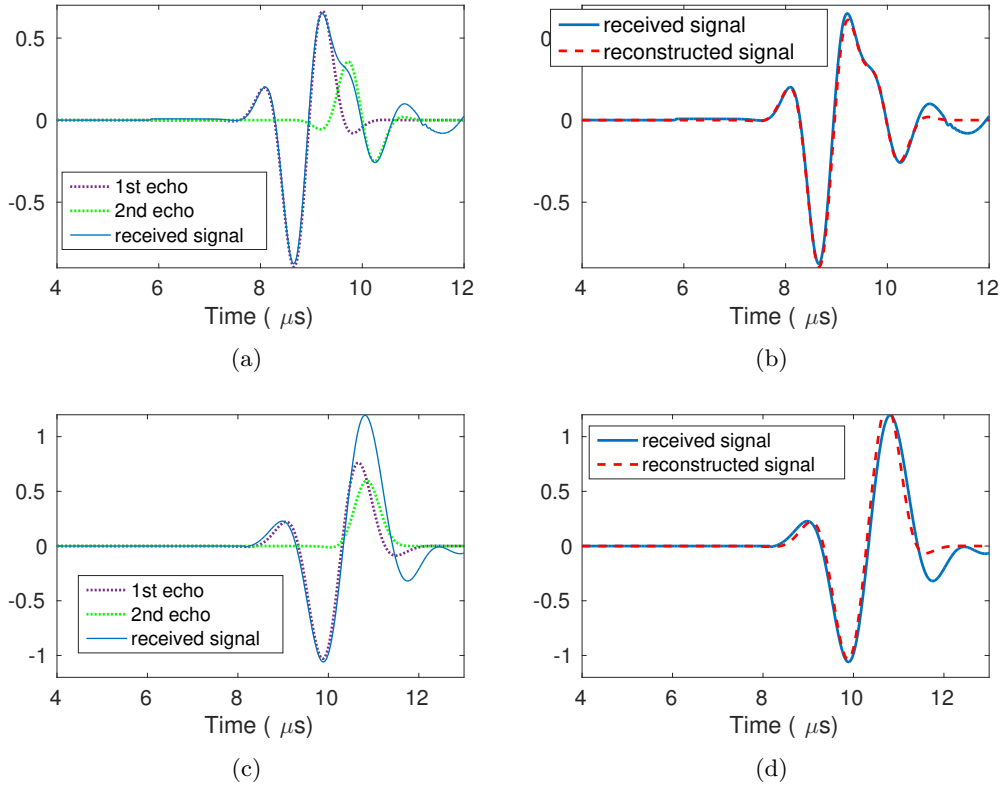


Figure 2.6: (a) the separation of two echoes when the $\text{Co.Th.}/\lambda$ is 0.38, (b) its reconstruction, (c) the separation of two echoes when the $\text{Co.Th.}/\lambda$ is 0.25, (d) its reconstruction.

Pacific Research Laboratories Inc., Vashon Island). The plane plates have a thickness of 3 millimeters and its ultrasound properties is illustrated in Table 2.2. An ultrasound transducer (Olympus) with central frequency 1MHz is used to produce the ultrasound excitation and record the reflected signal. The plate and transducer are both immersed in water. The transducer is connected to a Olympus 5077PR SQUARE wave pulser/receiver and a PicoScope 5000 Series Oscilloscope, which is shown on Fig. 2.8(a).

Table 2.2: the ultrasound parameters of sawbone, where L and T stand for longitudinal and transverse components

$c_L(m \cdot s^{-1})$	$c_T(m \cdot s^{-1})$	$\rho(kg \cdot m^{-3})$	$\alpha_L(dB \cdot cm^{-1} \cdot MHz^{-1})$
2870	1520	1640	2.63

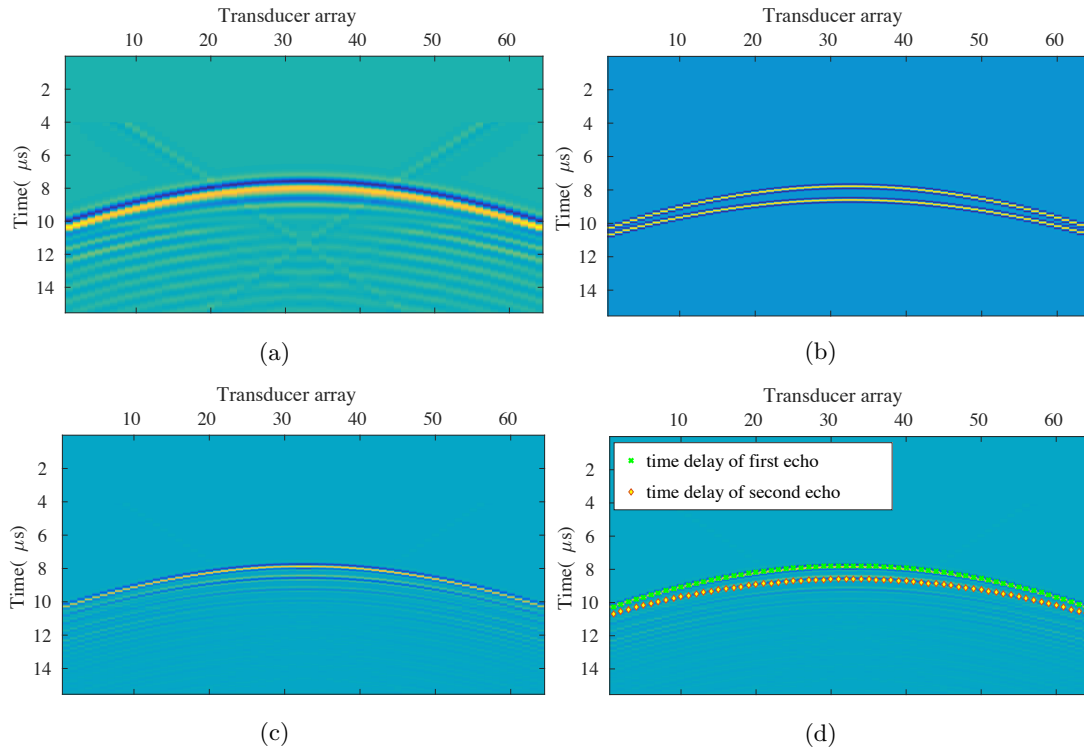


Figure 2.7: numerical validation of OMP in B-scan view: a) the received signals from a 1MHz excitation, b) the reconstructed signals by OMP with a 3MHz pulse, c) the received signals from a 3MHz excitation and d) superposition of (b) and (c)

The estimated parameters and corresponding Co.Th. and nBUA are shown in Table 2.3. Under 1MHz excitation, the ration of thickness/wavelength is 1.05 for sawbone plant, the corresponding precision of Co.Th. is 93%, and the nBUA is comparable to the parameter given in Table. 2.2.

Table 2.3: the ultrasound parameters estimated by OMP in bone phantom plate, using 1MHz excitation

	Co.Th(mm)	f_1 (MHz)	f_2 (MHz)	α_1	nBUA(dB MHz ⁻¹ cm ⁻¹)
sawbone plate (3mm)	3.2	0.89	0.87	1.45	3.94

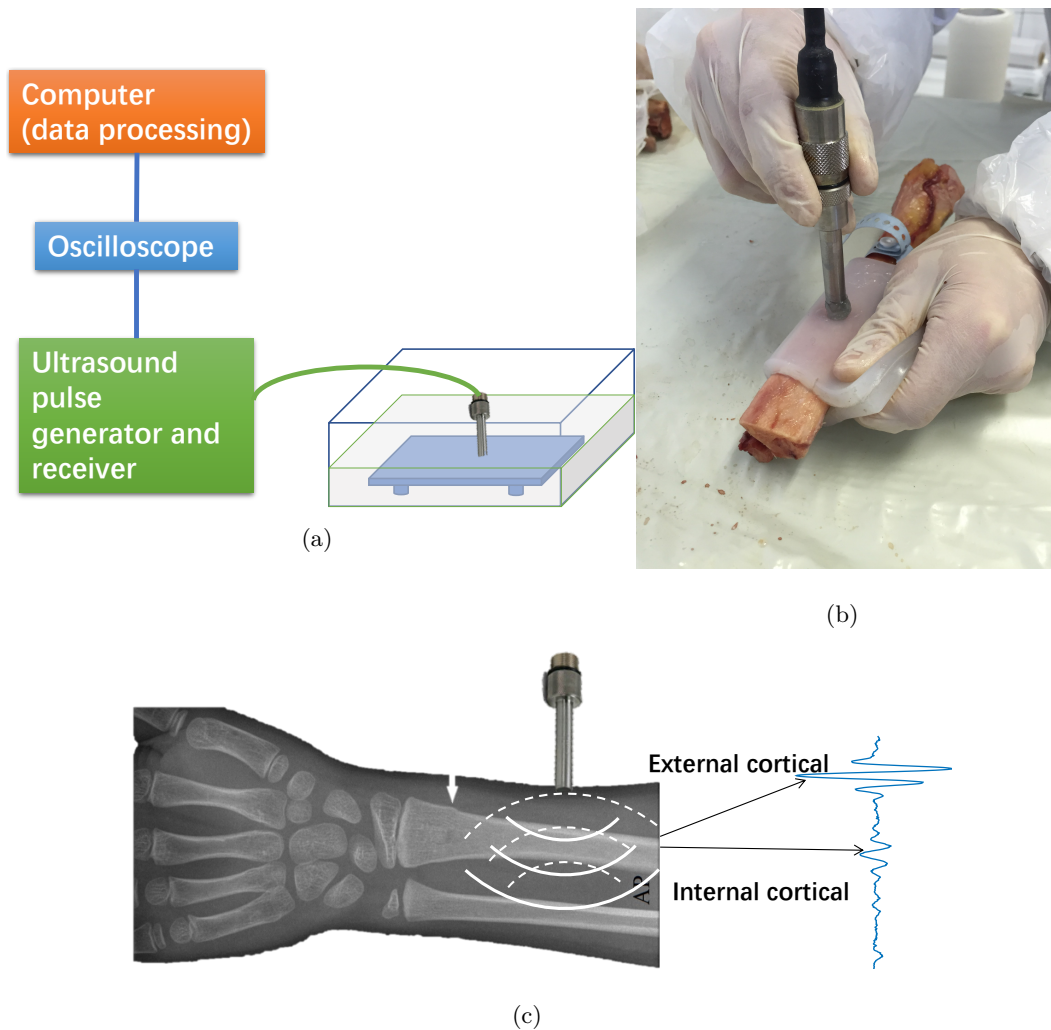


Figure 2.8: pulse echo ultrasound experimental setup for (a) bone phantom (b) tibia (*ex-vivo*) and (c) radius (*in-vivo*)

2.4.2 *Ex-vivo* measurement of the cortical bone

The *ex-vivo* validation has been performed on human tibia specimens provided by the B2OA laboratory (Bioingénierie et Bioimagerie Ostéo-Articulaire) at the Lariboisière hospital in Paris, according to the French program for voluntary corpse donation to science. The donors have been informed and have signed a written consent, in accordance with legal clauses stated in the French code of public health. Three tibia specimens without overlying soft tissues have been tested in this work. These samples are stored in a freezer before performing tests, and returned to the room temperature in a natural way. During the measurement, the tibia samples are covered by a 5mm-thick soft tissue-mimicking layer made of a solid water-

based polymer (CIRS, Norfolk, Virginia, USA), whose ultrasonic properties ($c_F = 1540m \cdot s^{-1}$, $\rho_F = 1.03g \cdot cm^{-3}$, and $\alpha_F = 0.52dB/cm$ at 1 MHz) are close to those of soft tissue ((Culjat et al., 2010)). The experiment protocol is the same as above with the sawbone plates, shown on Fig. 2.8(b). The only difference is the central frequency of the transducer that is now 3.5MHz. This higher frequency is preferred as M. Sasso *et al.* ((Sasso et al., 2008)) suggest that the BUA measurements performed around 4MHz are more sensitive to the cortical bone microstructure, because the wavelength is close to the typical size of the bone heterogeneities. Meanwhile, the attenuation of the amplitude of the second echo coming from the cortical internal boundary remains acceptable. This explains that the cortical bone measurements (*ex vivo* and *in vivo*) are done at this frequency. An example of received signal and its OMP reconstruction is illustrated on 2.9.

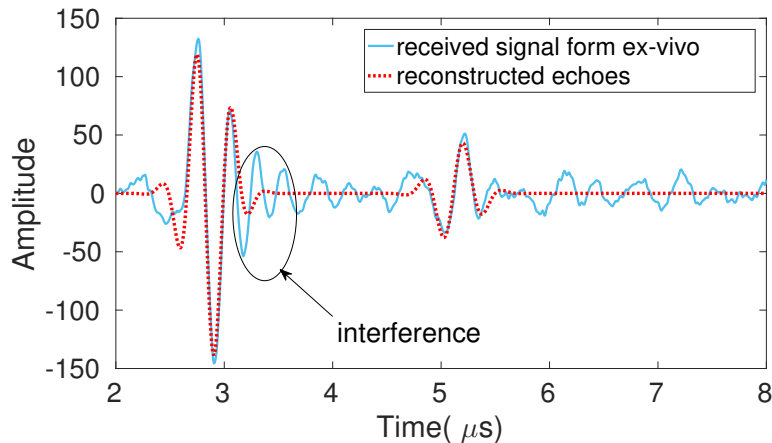


Figure 2.9: the two main echoes reconstruction, *ex-vivo* tibia measurement, using a 3.5MHz excitation

The estimated parameters and the corresponding Time delays and BUA are shown in Table 2.4

For some reason, only the cortical thickness of Sample #2 (No.331) has been measured by High resolution X-ray peripheral computed tomography (HRpQCT), which is 4.4 mm. the Co.Th. of Sample #2 (No.331) estimated by OMP is 4.3 mm, by using the $SOS = 3710$ m/s evaluated by the cepstrum method reported in (Karjalainen et al., 2008b). Its corresponding nBUA is 2.95 ($dB \cdot MHz^{-1} \cdot cm^{-1}$) normalized by its thickness 4.4 mm.

Table 2.4: parameters estimated by OMP on *in-vitro* tibias

	Time delay(μ s)	α_1	f_1 (MHz)	f_2 (MHz)	BUA(dB MHz $^{-1}$)
Sample #1 (No.388)	2.19	6.0345	2.8947	2.7368	4.4934
Sample #2 (No.331)	2.31	10.4138	2.8947	2.7368	2.6038
Sample #3 (No.414)	2.28	16.8966	3.0526	2.5000	5.6168

2.4.3 *In-vivo* measurement of the cortical bone

Five healthy subjects (24-38 years old) were recruited to be included in this study and signed a written consent in accordance with legal clauses stated in the French Code of Public Health. Subjects were firstly scanned with High resolution X-ray peripheral computed tomography (HR-pQCT, XtremeCT, Scanco Medical, Bruttisellen, Switzerland) using the standard manufacturer's *in vivo* parameters (60kVp, 1000mA, 100ms integration time), the measurements are located at the one-third distal left radius. Each section encompassed 100 slices and correspond to 9.02 mm measured with an 82 μ m voxel size. Cortical thickness and vBMD (Dcomp) are automatically provided by the device software, averaging the values obtained in the 3D matched volume (Boutroy et al., 2005). The ultrasound measurements have been performed at the same site with a mono element transducer (Olympus No.:V384, element size: 25 in DIA., bandwidth(-6dB): 2.03MHz) with a central frequency of 3.5 MHz. At this frequency, the thickness to wavelength ratio is 2.62 for a 3 mm radius cortical bone, which is a favorable ratio to obtain thickness with a good precision according to simulation results presented above. On the other hand, at this frequency, the attenuation of the amplitude of the echo coming from the cortical internal boundary remains acceptable for the experimental measurement. The transducer is connected to an Olympus 5077PR SQUARE wave pulse/receiver and a PicoScope 5000 Series Oscilloscope. The experimental configuration is illustrated in Fig. 2.1, 30 measurements are performed for each subjects. The received signals which contain two main identified echoes are remained to process by OMP, and 5 examples for each subject are shown in Fig.2.13 (Appendix), where an excellent match is obtained between them.

2.4.4 Results

For *in vivo* measurements, the received signal is very sensitive for slight movement of transducer by hand. In order to remove the abnormal data, the following strategies has been used here. Firstly, only the half shortest time delays are taken into consideration, which can avoid the influence when the transducer is not perpendicular to the cortical bone, and the time delays exceeded the interval $[\mu_\tau - 2\sigma_\tau, \mu_\tau + 2\sigma_\tau]$ will be removed, where μ_τ , σ_τ are the mean value and standard derivation of the half shortest time delays. Secondly, nBUA are exceeded the interval $[\mu_b - \sigma_b, \mu_b + \sigma_b]$ will be removed, where the μ_b and σ_b are the mean value and standard derivation of all the nBUA. Finally, the signals of which satisfy the both criterions used to analysis. The number of selected signals by the two criterions are [13, 12, 4, 8, 9] for subject 1~5 correspondingly. The mean and standard derivation values of the parameters for each subject is reported in Table. 2.5.

Table 2.5: the ultrasound parameters estimated in *in vivo* measurement at radius

Subject No.	Time delay (μs)	f_1	f_2	s_1
	(μs)	(MHz)	(MHz)	
1 (n=13)	1.71±0.03	3.1±0.04	2.92±0.04	16.18±1.29
2 (n=12)	1.73±0.04	3.0±0.18	2.68±0.08	14.76±3.51
3 (n=4)	1.71±0.02	2.84±0	2.34±0.05	12.35±0.24
4 (n=8)	2.04±0.10	2.95±0	2.60±0.16	16.85±1.47
5 (n=9)	2.32±0.01	2.88±0.06	2.46±0.23	14.39±0.75

In order to obtain Co.Th from the time delays, the value of the SOS in Eq. (2.18) must be chosen. Following (Karjalainen et al., 2008b), we used a value of SOS (the same for all subjects) which minimized the bias between Co.Th determined from ultrasound signals and from HR-pQCT measurements. Precisely, we solved the minimization problem by a linear fitting between the value of SOS and the thickness determined form HR-pQCT; the slope of the linear model is equal $2 \times \text{SOS}$. The calculated SOS is 3500 m.s^{-1} , which is used here to achieve the cortical thickness by Eq. (2.12). nBUA of each subject calculated using Eq. (2.18) based on the data of Tab. 2.5 is given in Tab. 2.6.

Table 2.6: the time delays, corresponding Co.Th. and nBUA of *in vivo* measurement at radius

Subject No.	OMP		HRpQCT	
	Co.Th. (mm)	nBUA (dB MHz ⁻¹ cm ⁻¹)	Co.Th. (mm)	vBMD (g cm ⁻³)
1	3.00±0.06	3.20±0.56	3.11±0.08	1.226±20
2	3.03±0.078	6.25±1.34	3.13±0.02	1.125±22
3	3.00±0.029	8.12±2.51	3.28±0.06	1.056±26
4	3.57±0.18	5.68±2.74	3.43±0.02	1.144±21
5	4.05±0.019	6.47±1.78	3.79±0.03	1.158±25

Highly Pearson correlation were found between Ct.Th. determined by OMP and HRpQCT at the one-third distal radius ($r^2 = 0.92$, $p < 0.009$, RMSE = 0.22), shown in Fig. 2.10(a). Meanwhile a significant correlation between nBUA and vBMD was observed at same site ($r^2 = 0.90$, $p < 0.013$, RMSE = 0.64), shown in Fig. 2.10(b), the linear regression between them is: $\text{nBUA} = -27.6 \text{ vBMD} + 37.5$.

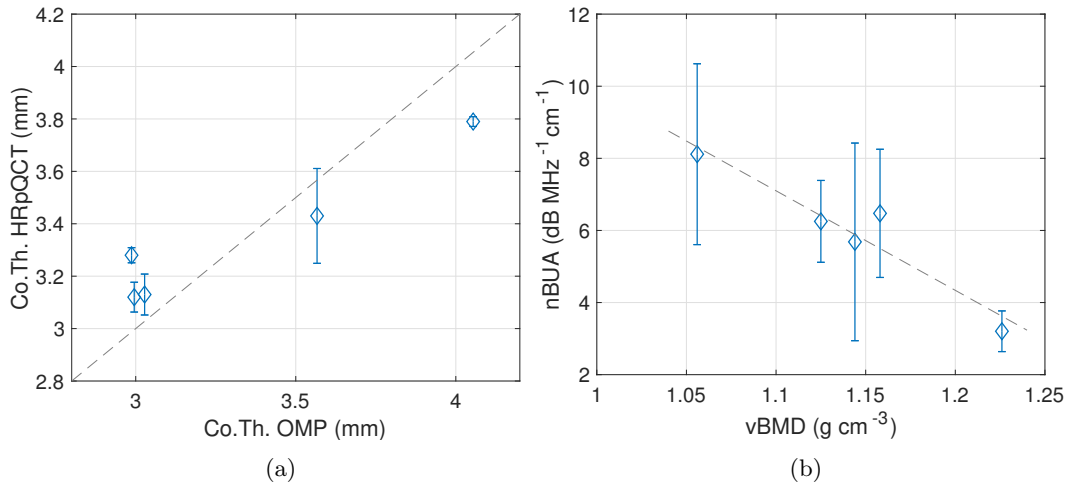


Figure 2.10: (a) linear correlation between the values of the cortical thickness by HRpQCT and OMP ; (b) linear correlation between the vBMD by HRpQCT and nBUA by OMP

2.5 Discussion

In numerical simulation, the OMP show promising reconstruction in small ratio of $\text{Co.Th.}/\lambda = 0.38$. However, deformation and unknown multi-scatters are frequently overlapped on the main echo *in vivo* measurement. It is better to avoid the overlapping between two main echoes corresponding to the cortical interface, meanwhile the amplitude of echo from the endosteal surface need to be exploitable. Consequently, 3.5 MHz pulse is considered in this study. Pulse-echo ultrasound is mainly used for tibia based on the envelop method. The OMP based on estimation of all the waveform parameters at the same time, provides better precision to overcome the deformation of signal, which makes the measurement on radius possible.

The OMP increases the resolution in the experimental determination of physical parameters of the bone, by building an over-completed dictionary that contains all possible combinations of each parameter sampled in user-defined ranges. Combining with the information obtained by difference of envelop, OMP shows good robust in dealing with the deformation and unknown scatters of *in vivo* signal. In this study, the OMP has been used in cortical bone assessment by QUS to estimate both the cortical thickness and broadband attenuation. As far as we know, this is the first application of such advanced sparse signal processing method in the domain of cortical bone evaluation by QUS, and it exhibits promising performances (better resolution in cortical thickness estimation and successful estimation of the BUA *in vivo*). The traditional method for cortical thickness estimation by envelop and cespral method are performed on bones with a thickness from 1.5~6mm in (Karjalainen et al., 2008a), it shows good correlation ($r = 0.96$) in this wide range with 59 samples, as shown on Fig. 2.11. If the range is decreased to 3~4mm (domain identified by the two red lines, and corresponding to most radii), the correlation is not so good. However, the OMP still can provide a good correlation ($r^2 = 0.92$) in such a small range. And the SOS obtained by linear fit between the time delays and the thickness measured by pQCT is 3770m/s, which is close to 3800m/s, reported in (Karjalainen et al., 2008a).

The calculation of nBUA were started from the formulation given in (Kuc et al., 1976), and is now adapted to the pulse-echo mode. For *in vivo* measurements, the main interest of the pulse-echo mode is that we can neglect the influence of soft tissues, since all the components (and particularly the waves coming from the external and internal boundaries of the cortical shell) travel through the same path

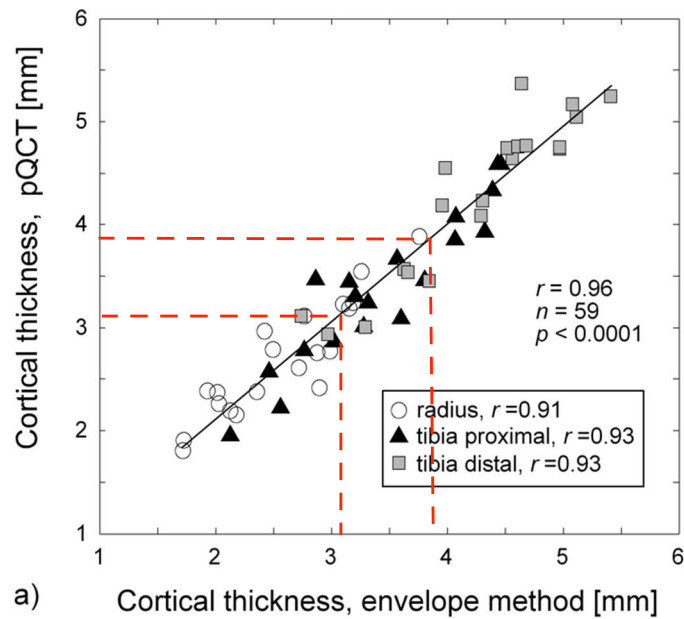


Figure 2.11: The linear fit between the cortical thickness determined by pQCT and time delay estimated in (Karjalainen et al., 2008a)

of soft tissues.

Simon *et al* (Bernard et al., 2015) has illustrated that the axial shear damping ratio Q_{44} (approximately equal to the damping factor of the first resonant peak) shows a linear negative correlation with the bone mass density. Sasso *et al* (Sasso et al., 2008) has reported nBUA is correlated with both vBMD ($r^2 = 0.57$, $p < 10^{-5}$, RMSE=1.6) in the radial direction for *in vitro* bovine femur, and the linear regression between them is $\text{nBUA} = -25.2\text{vBMD} + 40.6$, which are comparable to our results ($r^2 = 0.90$, $p < 0.013$, RMSE=0.64, $\text{nBUA} = -27.6\text{vBMD} + 37.5$). Meanwhile, the Mean value and standard derivation of nBUA between the 5 subjects are $6.65 \pm 2.83 \text{ dB MHz}^{-1} \text{ cm}^{-1}$, which are comparable with the one obtained from *in vitro* measurements and perviously reported in (Han et al., 1996; Lakes et al., 1986; Lees and Klopholz, 1992; Sasso et al., 2008; Zheng et al., 2007), summarized in Tab. 2.7.

From these results, we can conclude that the values of the cortical thickness determined by HRpQCT and OMP are highly correlated, as well as the vBMD determined by HRpQCT and the nBUA determined by OMP. Overall, the combination of OMP and pulse-echo ultrasound provides a powerful and efficient tool to evaluate the nBUA and Co.Th. of the cortical bone, with a good resolution

and robustness *in vivo*. This work is a primary study which shows promising and reasonable result, a more wide volume study is needed for further validation.

2.6 Appendix: Comparison between OMP and the envelop method

The traditional methods for cortical thickness measurement consist in envelop and cesprtral methods, which show similar performance. The envelop method is performed on bone samples with a thickness in the range 1.5 ~ 6mm in (Karjalainen et al., 2008a), and a good correlation is obtained (correlation coefficient $r = 0.96$) in this wide range made of 59 different samples. If the thickness range is decreased to 3 ~ 4mm (this corresponds to the usual thickness of the radius), the correlation decreases significantly. Here we give an example for *in vivo* signal, there is always exist some interference such as multi-scatters and reverberations, which will influence the shape of the envelop. Consequently, the maximum of envelop is not always refer to the time delays of echoes. Since the OMP search the best match of signal by a Gabor function, which consists of all best matches parameters, it will absolutely give a more precisely estimations. It can be observed in Fig. 2.12, the time delay between two echoes by OMP is $\tau = \tau_2 - \tau_1 = 7.384 - 5.08 = 2.304\mu s$, however, the time delay between two echoes by envelop is $\tau = \tau_2 - \tau_1 = 7.464 - 5.12 = 2.344\mu s$. The time delay between the two echoes and themselves by envelop are mismatch with the OMP.

2.7 Appendix: Received *in vivo* signal and reconstruction by OMP

Here is the example of received signal of each subject and its reconstruction by OMP, illustrated in Fig. 2.13.

In the *in vivo* data acquisition, 30 measurements are recorded for each subjects. The received signals which contain two main identified echoes are remained to process by OMP, the selected signal are processed by adapted OMP, the corresponding Co.Th and nBUA are illustrated in Fig. 2.14 for each subject. It can be observed that the parameter are sensitive with the movement of transducer, so it is important to ignore the bias data, and use the mean value. The criterions for choosing data used in this study are: firstly, only the half shortest time delays

2.7. Appendix: Received *in vivo* signal and reconstruction by OMP 49

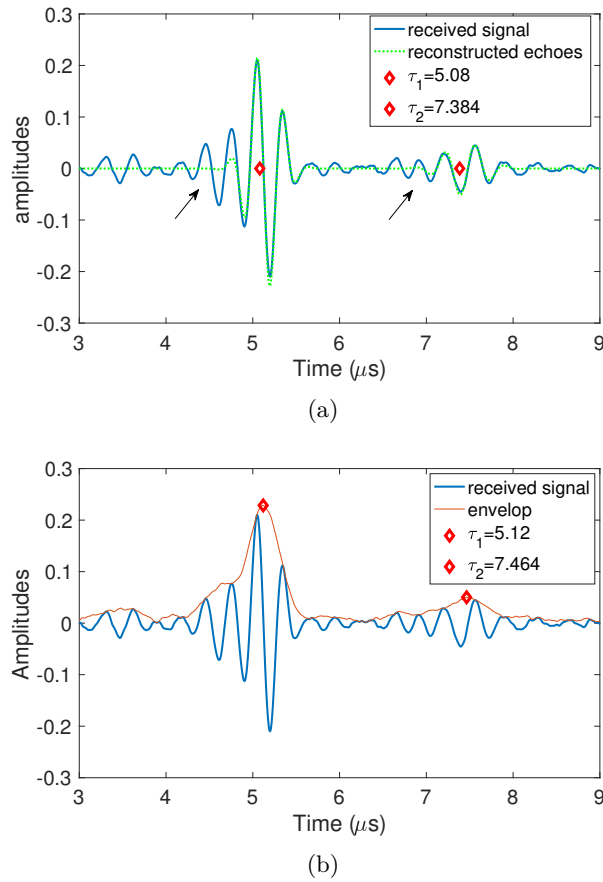


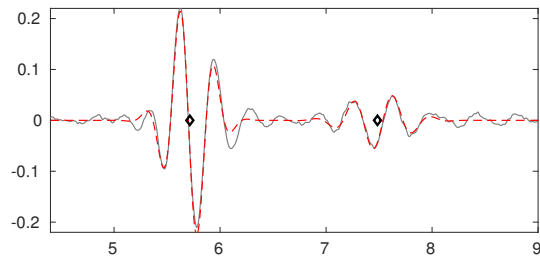
Figure 2.12: Up: the time delays estimated by OMP (*in vivo* signal), the black arrow indicates the reverberations. Down: the time delay estimated by the envelop method (*in vivo* signal)

are taken into consideration, which can avoid the influence when the transducer is not perpendicular to the cortical bone, and the time delays exceeded the interval $[\mu_\tau - 2\sigma_\tau, \mu_\tau + 2\sigma_\tau]$ will be removed, where μ_τ , σ_τ are the mean value and standard derivation of the half shortest time delays. Secondly, nBUA are exceeded the interval $[\mu_b - \sigma_b, \mu_b + \sigma_b]$ will be removed, where the μ_b and σ_b are the mean value and standard derivation of all the nBUA.

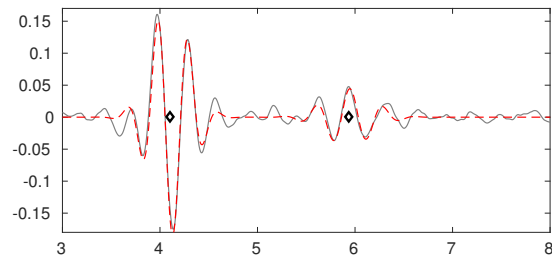
Table 2.7: Mean BUA of cortical bone and standard deviation, resulting from *in vivo* measurements and previously measurements

Reference	Type of bone	Number of samples	Frequency range (MHz)	nBUA (dB MHz ⁻¹ cm ⁻¹)
Lakes et al. (1986)(Lakes et al., 1986)	bovine femur (<i>in vitro</i>)	1	1-7	~3
Lees and Klopoltz (1992)(Lees and Klopoltz, 1992)	bovine femur (<i>in vitro</i>)	4	0-30	~4
Han et al. (1996)(Han et al., 1996)	bovine femur (<i>in vitro</i>)	5	0.3-0.7	5~12
Zheng et al.(2007)(Zheng et al., 2007)	bovine femur (<i>in vitro</i>)	8	2.25	4.91±0.65
Sasso et al.(2008)(Sasso et al., 2008)	bovine femur (<i>in vitro</i>)	40	3.5-4.5	4.2±2.4
This paper	radius (<i>in vivo</i>)	5	3.5	6.65± 2.83

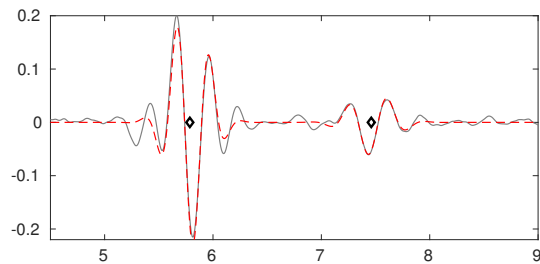
2.7. Appendix: Received *in vivo* signal and reconstruction by OMP 51



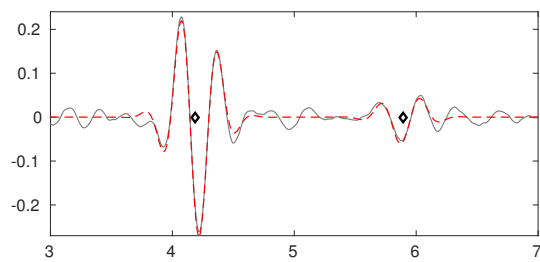
(a) qv



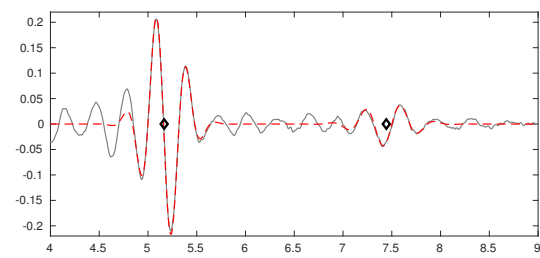
(b)



(c)



(d)



(e)

Figure 2.13: 5 samples of received signals in-vivo (gray line) and its reconstruction (red dashed line) by OMP, the line array indicates the unknown deformations and multi-scatters

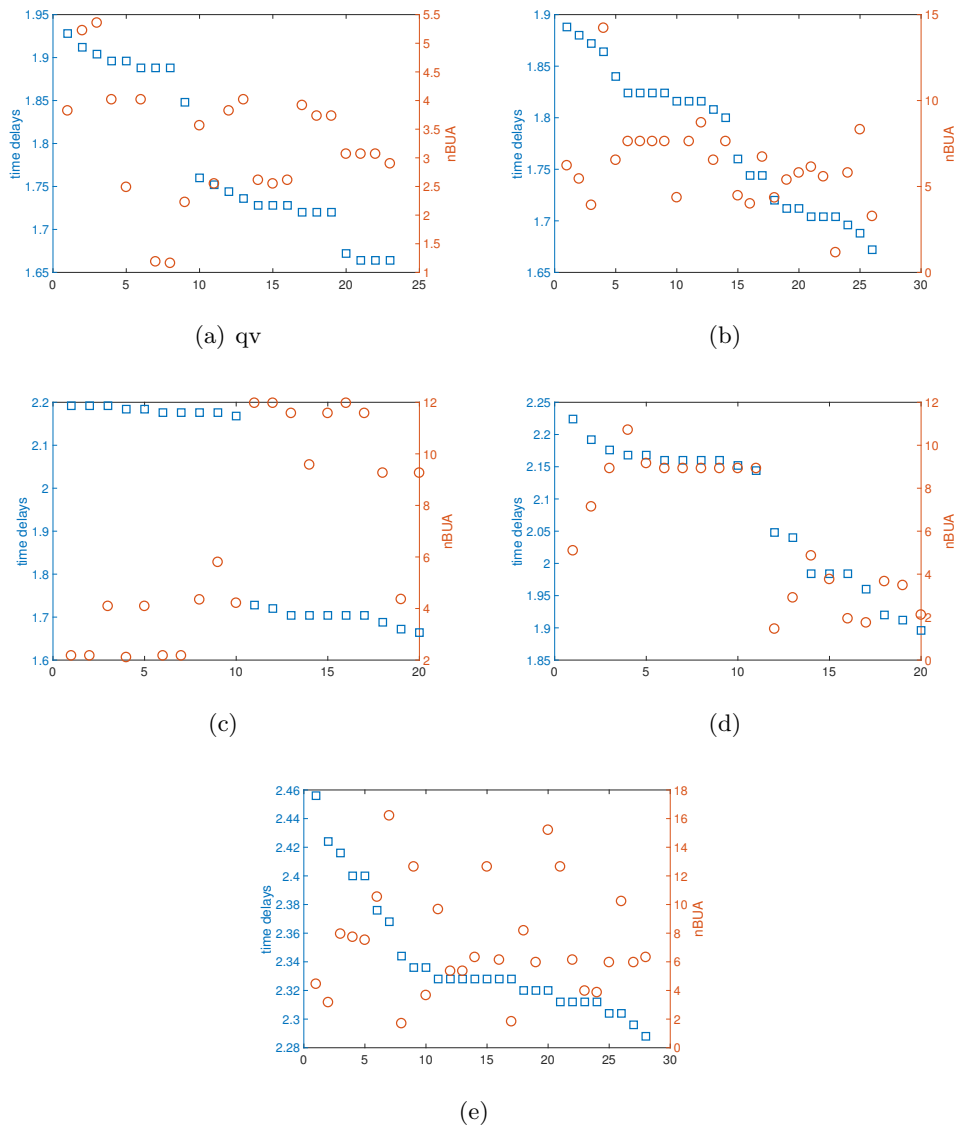


Figure 2.14: 5 samples of received signals in-vivo (gray line) and its reconstruction (red dashed line) by OMP, the line array indicates the unknown deformations and multi-scatters

CHAPTER 3

Cortical bone imaging by Time Domain Topological Energy

The structure of the cortical bone has a great influence on the skeletal bio-mechanics stability. Thus, the determination of this structure and the material properties of the bone is important in predicting the risk of fracture and osteoporosis. Ultrasound tomography technologies have been developed as an alternative to X-ray methods for bone quality assessment of the mechanical characteristics of the bone, as well as geometrical image. However, these technologies are limited by the poor resolution and are highly time-consuming, due to the large impedance contrast between hard bones and the surrounding soft tissues. Improving the resolution of ultrasound tomography and decreasing time-consuming are two essential targets to converge to a comprehensive clinical mean in accessing bone structure information. During the last decades, the Time Domain Topological Energy (TDTE) has been developed and used in Non Destructive Testing ((Dominguez and Gibiat, 2010)). Here, we introduce the TDTE method and two necessary additional strategies in imaging of the cortical bone at the femoral neck. The first strategy consists in using the combined sparse signal processing to enhance the echoes coming from the internal boundary of the cortical bone in the image resulting from the first iteration of TDTE. As for some relevant irregular shape of the internal boundary of the cortical bone, this sparse signal processing is limited and an iterative TDTE (second strategy) is required to obtain the cortical internal geometry, and this step is much more time-consuming than the first iteration. The validation of these two adapted TDTE approached has been studied through 2D numerical simulations using a bone-mimicking phantom of the real femoral neck, with promising results.

In literature, we can find that the geometry and microstructure of the bone are significantly more correlated with bone fractures than bone mineral density ((Beck et al., 2006; Ritchie et al., 2009; Snedeker et al., 2006)), particularly for the cortical bone, where most osteoporotic fractures occur. Methods for assessing the microstructure and geometry of the cortical bone with high resolution include DXA and microCT ((Donnelly, 2010; Hangartner and Short, 2007; Ström et al., 2011)). The main inconvenience of these methods is i) the exposition to ionizing radiations and ii) the lack of availability and accessibility compared to ultrasound systems. Quantitative Ultrasound (QUS) appears as a promising tool to access

Chapter 3. Cortical bone imaging by Time Domain Topological Energy

the quality of the cortical bone by providing information on the bone mechanical parameters (speed of sound and/or attenuation), as well as geometrical information ((Laugier, 2008; Laugier and Haiat, 2010)). With the two considerable advantages of non-ionizing and low cost device, QUS appears as an attractive approach of the cortical bone imaging.

The localization and characterization of flaws or obstacles in a fluid or solid elastic medium is the most classical problem in domains like non-destructive testing, medical imaging and geophysics. This often involves solve an inverse problem, which is still an open question that is widely studied in many research teams. The Time Domain Topological Gradient (TDTG) is based on the same main principle as Full Waveform Inversion, which consists in minimizing the misfit between the signals coming from the inspected medium and the ones from the reference medium, but the formulation has been adapted by the mathematical community interested in shape optimization. The method has been first initiated by (Eschenauer et al., 1994), and (Sokolowski and Zochowski, 1999). Then it has been extended by (Garreau et al., 2001; Masmoudi et al., 2005) to electromagnetics and linear elasticity. (Dominguez et al., 2005) develop another extension for the elastodynamic case in non-destructive testing. M. Bonnet has also develop the topological derivative (different name of topological gradient) in acoustic, elastic, anisotropic elasticity (Bonnet, 2006; Bonnet and Delgado, 2013; Guzina and Bonnet, 2004). The TDTG method consists in the computation of the gradient relying on the combination of two simulated ultrasonic fields (forward and adjoint fields), similar to the adjoint problem used in FWI. The gradient has different formulations depending on the boundary conditions, including Neumann and Dirichlet conditions, also depending on the kind of defects that may exist in the material. An alternative solution consists in using another quantity derived from the gradient, and called Time Domain Topological Energy (TDTE, (Dominguez and Gibiat, 2010)). This alternate approach is less rigorous and precise, but is faster and more representative. (Sahuguet et al., 2010) have first applied TDTE in biological soft tissues imaging. TDTE has also shown promising performances in experiments with porous and weakly reflective materials, and carbon epoxy composite materials ((Dominguez and Gibiat, 2010)). Based on these experiments, we can expect some potential performance of this approach for the cortical bone imaging.

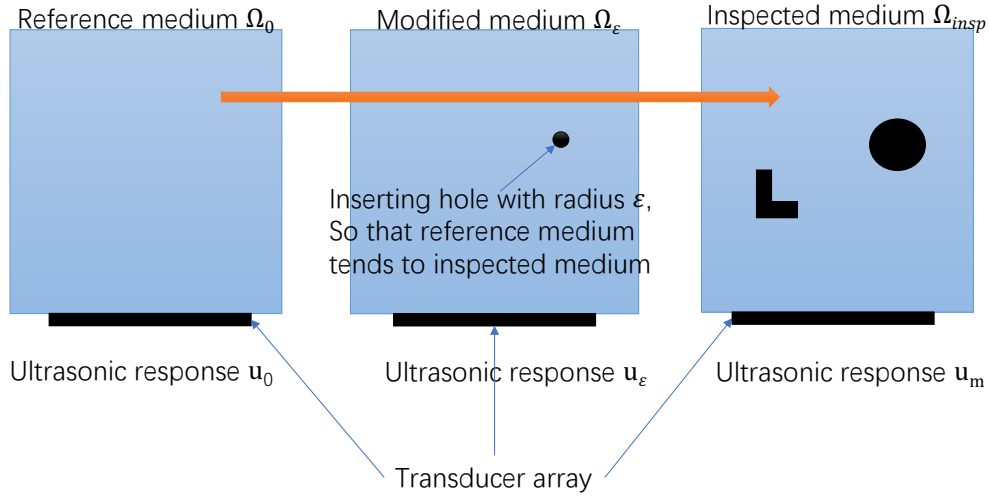


Figure 3.1: principle of the topological asymptotic method

3.1 Time Domain Topological Gradient

3.1.1 Cost function

The Time Domain Topological Gradient (TDTG) was derived from the mathematical concept of topological optimization developed by Schumacher ((Eschenauer et al., 1994)), and partially generalized by Sokolowski ((Sokolowski and Zochowski, 1999)). In this section, we introduce the major principles and notations of the topological asymptotic method, the details of the mathematical demonstrations can be found in the reference (Dominguez et al., 2005) (Sokolowski and Zochowski, 1999). The process is initialized with an initial guess, denoted as the reference domain Ω_0 . The aim is to modify the topology of this initial reference domain by inserting zones with strong contrast of the elastic properties (or density) with the rest of the medium. This optimization process is repeated until the modified topology of the reference domain tends to the topology of the inspected medium Ω_{insp} , which is illustrated on Fig. 3.1.1.

The initial guess and inspected medium are not observed directly, but through their response to an incident an acoustic wave. We use a cost function $j(\Omega)$ to estimate the distance between the two media. Starting from Ω_0 and building Ω_ε by adding a small hole of radius ε at position x , the variation of the cost function can be written at the first order as

$$j(\Omega_\varepsilon) = j(\Omega_0) + f(\varepsilon)g(x) + o(f(\varepsilon)) \quad (3.1)$$

Chapter 3. Cortical bone imaging by Time Domain Topological Energy

with $\lim_{\varepsilon \rightarrow 0} f(\varepsilon) = 0$ and $f(\varepsilon) > 0$.

In this expression, the gradient $g(x)$ represents the sensitivity of the cost function to the insertion of a small hole at location x . In other words, the more g is negative at x , the higher is the possibility to insert a hole of radius ε at x . To quantify the gradient of the cost function, we use the ultrasound response of the corresponding domain. Then the cost function is written as follows

$$j(\Omega) = \frac{1}{2} \int_0^T \left(\int |\mathbf{u}_\Omega - \mathbf{u}_m|^2 dx \right) dt \quad (3.2)$$

where the \mathbf{u}_Ω is the ultrasound response of reference medium Ω , and \mathbf{u}_m the ultrasound response of the inspected domain.

3.1.2 The topological gradient for linear elasticity and elastodynamics

First of all, the physical meaning of creating a hole depends on the condition imposed on its boundary. The type of boundary condition on the edge of the hole is essential in establishing the topological asymptotic expansion. In the case of flaw investigation with ultrasound in acoustic or elastic media, three types of boundary conditions can be considered:

- the Dirichlet condition corresponds to the insertion of an infinitely rigid ball and imposes the displacements at the medium/ball interface to be zero,
- the Neumann condition models a cavity (a hole) and imposes the normal stress at the boundary of the hole to be zero
- the impedance type boundary condition corresponds to an elastic inclusion, this case is not considered in this work.

For the case of a classical linear elasticity problem with the following conditions:

$$\begin{aligned} -\operatorname{div}\sigma(u) &= 0 \quad \text{in } \Omega \\ \sigma(u)\mathbf{n} &= F \quad \text{Neumann condition on the boundary of } \Omega \\ u &= 0 \quad \text{Dirichlet condition on the boundary of } \Omega \end{aligned}$$

where σ denotes the stress tensor. To calculate the topological gradient, we need both the solutions of the forward and adjoint problems in the reference medium Ω . Garreau *et al.* ((Garreau et al., 2001)) give the expression of the topological gradient in the case of linear elasticity, solved using the adjoint method. The results are shown in Table 3.1, where

- u_0 and $\sigma(u_0)$ are respectively the displacement and stress field solutions of the forward problem in the reference medium Ω_0 ,
- u_0^\dagger and $\varepsilon(u_0^\dagger)$ are respectively the displacement and strain field solutions of the adjoint problem in the reference medium Ω_0 ,
- λ and μ are the Lamé coefficients of Ω_0 , ε is the radius of the 'hole'.

For the case of elastodynamics, the topological gradient based on the same principle has been deduced by (Dominguez et al., 2005), where the formula are shown in Table 3.2. From these expressions of the topological gradient, we can observe that the dominant terms are scalar products of the solutions to the forward and adjoint problems at every point of the space domain and integrated over the acquisition time. In the particular case of rigid ball inclusions, the scalar products involve the displacement fields, while in the case of cavities, they involve the tensorial products of the stress tensors. Practically, the solutions are available in a time interval $[0, T]$. In such case, T must be chosen such that the displacement fields in the domain after T are weak enough to be neglected in the computation of the topological gradient.

To implement the computation of the Topological Gradient, we need the displacement fields and/or stress tensors for the forward and adjoint problems. The forward problem can be formulated in the time domain as

$$\frac{\partial^2 u}{\partial t^2} + Au = F \quad t \in [0, T] \quad (3.3)$$

with the initial condition $u(\mathbf{x}, 0) = 0$, where $A = \Delta + k^2$, k is the wave number. The associated adjoint problem is described by

$$\frac{\partial^2 u^\dagger}{\partial t^2} + A^* u^\dagger = -D_u J(u_0) \quad t \in [T, 0] \quad u^\dagger(\mathbf{x}, T) = 0 \quad (3.4)$$

where u_0 is the solution to the forward problem, $D_u J$ the derivative of J with respect to the variable u , and A^* the adjoint operator of A . In both cases of Laplacian and elastodynamics, this operator is self-adjoint ($A^* = A$), and adjoint operator of $(\partial_t^2 + A)$ is $(\partial_t^2 + A^*)$. The initial condition of the associated adjoint

Table 3.1: Topological asymptotic method for linear elasticity

Boundary condition on $\partial\omega$	$f(\varepsilon)$	Topological gradient: $g(x)$
2D Dirichlet	$-\frac{2\pi}{\log(\varepsilon)}$	$\frac{2\mu(\mu+\eta)}{2\mu+\eta} u_0 \cdot u_0^\dagger$
3D Dirichlet	$4\pi\varepsilon$	$\frac{3\mu(\lambda+2\mu)}{2\lambda+5\mu} u_0 \cdot u_0^\dagger$
2D Neumann	$\pi\varepsilon^2$	$-\frac{\mu+\eta}{2\mu\eta} (4\mu\sigma(u_0) : \varepsilon(u_0^\dagger) + (\eta - 2\mu)\text{tr}\sigma(u_0)\text{tr}\varepsilon(u_0^\dagger))$
3D Neumann	$3/4\pi\varepsilon^3$	$-\frac{3(\lambda+2\mu)}{4\mu(9\lambda+14\mu)} (20\mu\sigma(u_0) : \varepsilon(u_0^\dagger) + (3\lambda - 2\mu)\text{tr}\sigma(u_0)\text{tr}\varepsilon(u_0^\dagger))$

Table 3.2: Topological asymptotic for elastodynamics

Boundary condition on $\partial\omega$	$f(\varepsilon)$	Topological gradient: $g(x)$
2D Dirichlet	$-\frac{2\pi}{\log(\varepsilon)}$	$\int \left(\frac{2\mu(\mu+\eta)}{2\mu+\eta} u_0 \cdot u_0^\dagger \right) dt$
3D Dirichlet	$4\pi\varepsilon$	$\int \left(\frac{3\mu(\lambda+2\mu)}{2\lambda+5\mu} u_0 \cdot u_0^\dagger \right) dt$
2D Neumann	$\pi\varepsilon^2$	$\int \left(-\frac{\mu+\eta}{2\mu\eta} (4\mu\sigma(u_0) : \varepsilon(u_0^\dagger) + (\eta - 2\mu)\text{tr}\sigma(u_0)\text{tr}\varepsilon(u_0^\dagger)) - \rho\partial_t u_0 \cdot \partial_t u_0^\dagger \right) dt$
3D Neumann	$3/4\pi\varepsilon^3$	$\int \left(-\frac{3(\lambda+2\mu)}{4\mu(9\lambda+14\mu)} (20\mu\sigma(u_0) : \varepsilon(u_0^\dagger) + (3\lambda - 2\mu)\text{tr}\sigma(u_0)\text{tr}\varepsilon(u_0^\dagger)) - \rho\partial_t u_0 \cdot \partial_t u_0^\dagger \right) dt$

problem can be set occurring at $t = T - t$ (Dominguez et al., 2005). By assuming no intrinsic attenuation in the medium, A is self-adjoint and (3.4) becomes:

$$\frac{\partial^2 u^\dagger(\mathbf{x}, T - t)}{\partial t^2} + Au^\dagger(\mathbf{x}, T - t) = -D_u J(u_0)(\mathbf{x}, T - t) \quad t \in [T, 0] \quad u^\dagger(\mathbf{x}, T) = 0 \quad (3.5)$$

From this expression, it can be observed that the adjoint problem in the time domain is identical to the forward problem, except that time evolves in the opposite direction. In other words, the adjoint problem can be solved using the forward solver, with time-reversed sources. So the adjoint problem becomes:

$$\frac{\partial^2 u^\dagger(\mathbf{x}, T - t)}{\partial t^2} + Au^\dagger(\mathbf{x}, T - t) = -(u_0 - u_m)(\mathbf{x}, T - t) \quad t \in [T, 0] \quad (3.6)$$

where u_0 is the solution of the forward problem in the reference medium Ω_0 and u_m the measurement obtained from the inspected medium Ω_{insp} .

3.1.3 Iterative process for the Time Domain Topological Gradient

From the above discussion, we can now give the iterative procedure of the time domain topological gradient method:

- measurement from the unknown medium Ω_{insp} with a linear array of ultrasonic transducers, and record the response $u_m(t)$, $t \in [0, T]$,
- numerical resolution of the forward problem in the reference medium Ω_0 with the same excitation as used experimentally, and record the response $u_0(\mathbf{x}, t)$, $\mathbf{x} \in \mathbb{R}^{\Omega_0}$,
- numerical resolution of the adjoint problem in the reference medium Ω_0 with the source $(u_m - u_0)(T - t)$, for $t \in [0, T]$, and record $u^\dagger(\mathbf{x}, T - t)$ on Ω_0 , $\mathbf{x} \in \mathbb{R}^{\Omega_0}$,
- computation of the topological gradient according to the formulas given in Tables 3.1 and 3.2,
- update the reference domain Ω_0 : modify the state of the $\beta\%$ most negative points.

Rigorously, applying the TDTG requires an iterative procedure to extrude the most negative point. The parameter β controls the speed of convergence. High values of β give a quick but poorly accurate solution, while small values of β yield a slow but very accurate solution. There are several methods to choose the proper value of β , including Tikhonov regularization (Engl et al., 1996), etc. The iterative

Chapter 3. Cortical bone imaging by Time Domain Topological Energy

process is expensive in terms of memory resources and computation time, since at each iteration, the forward and backward simulations need to be performed and the resulting displacement fields in time and space should be stored. As one step of the TDTG process corresponds to time reversed propagation, the natural refocusing of time reversal avoids falling in a local minimum, which means that the optimization procedure follows the physical solution as iterations increase. This iterative process will converge to a topology that is finally very close to the real one. However, it has been observed through simulations and experiments that TDTG provides good imaging results without iterating the process. This makes it a very promising method since it is very few time consuming and numerical instabilities due to the ill-posed nature of the inverse problem are avoided.

To avoid the iterative procedure of the topological gradient method, an alternative approach, called "Time Domain Topological Energy" (Dominguez and Gibiat, 2010), has been proposed, based on the common property of the different formulas given in Tables 3.2, which all involve a product of two simulated fields integrated over a given temporal interval.

TDTE gives a faster result, it is defined as the product of the energies of the forward and adjoint wavefields, integrated in time:

$$K_{TE}(\mathbf{x}) = \int_0^T \|\mathbf{u}^\dagger(\mathbf{x}, T-t)\|^2 \|\mathbf{u}(\mathbf{x}, t)\|^2 dt \quad (3.7)$$

where $\|u\|$ is the Euclidean norm of the vector u . This quantity K_{TE} removes the natural oscillations of the topological gradient. It has been proved in (Dominguez et al., 2005) that the isometric curves of the topological energy give a good idea of the sizes and positions of the flaws in the medium. The topological energy is straightforward, and gives an approximate but usually sufficient distribution of the flaws with only one iteration, therefore reducing the computation time. The TDTE imaging procedure can be illustrated as follows:

- measurement of the response $\mathbf{y}(t)$ from the unknown medium Ω_{insp} to a transient plane wave with an array of ultrasonic transducers during a given time T ,
- measurement of the response $\mathbf{u}^\dagger(\mathbf{x}, t)$ from a reference medium to the same ultrasonic excitation, the reference medium should be defined as close as possible to the inspected medium,

- computation of the time reversal of the difference $(\mathbf{u}^\dagger - \mathbf{y})(T-t)$, which is used as adjoint source term to obtain the resulting field $\mathbf{u}^\dagger(\mathbf{x}, t)$ in the reference medium,
- the kernel of topological energy is finally evaluated by integrating the product of $\|\mathbf{u}^\dagger(\mathbf{x}, T-t)\|^2$ and $\|\mathbf{u}(\mathbf{x}, t)\|^2$ over time, as expressed in equation (3.7).

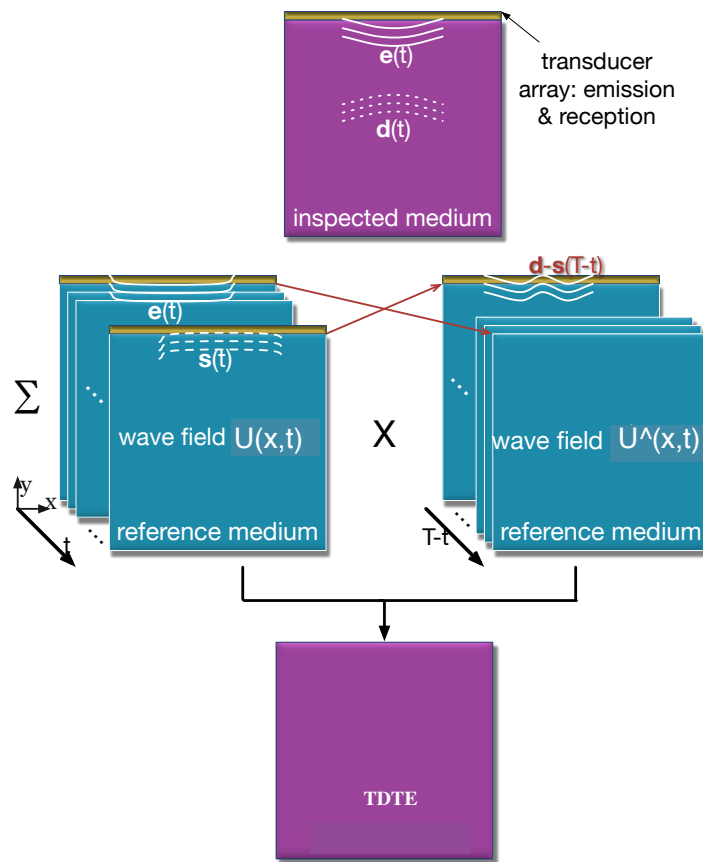


Figure 3.2: numerical scheme of TDTE

The spatial resolution of the method is governed by parameters such as the limited aperture of the sensor array and its discretization sharpness. Moreover, the focusing effect of the time reversal operation is not perfect, even in the case of a time reversal cavity, due to the absence of acoustic well at the location of the flaw. In such conditions, a focal spot of half the wavelength can be reached at best (Fink, 1992).

3.2 Numerical simulations

3.2.1 Image of a 2D cross-section of cortical bone

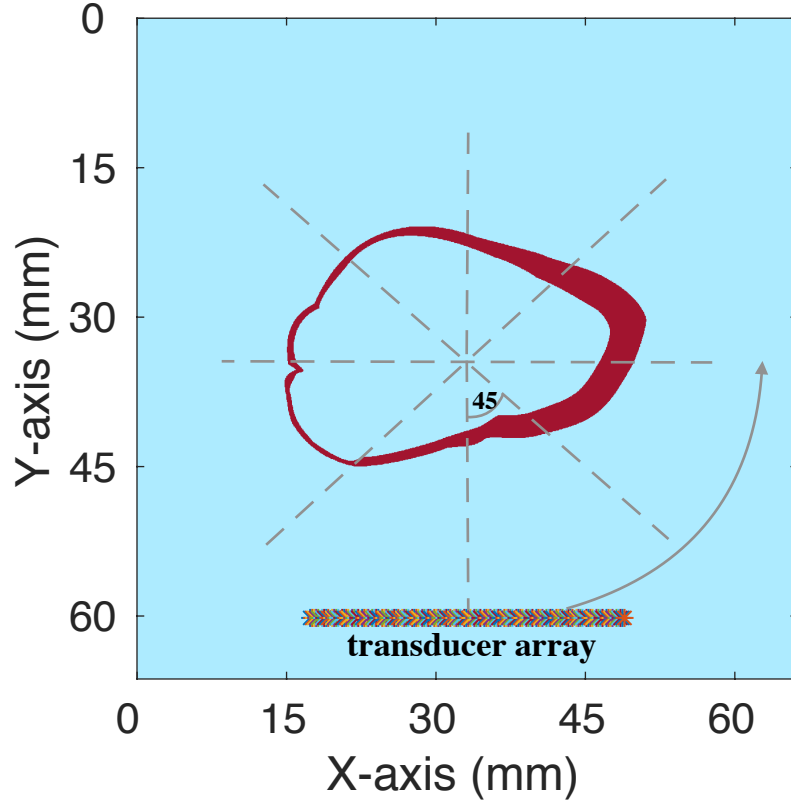
To validate the imaging capacity of the adjoint method and the advantages of the combination of the above strategies, we have run various numerical simulation. We first started with a thin slice of a real femoral neck sample obtained from an X-ray image and used to represent the cortical shell in the numerical simulation. The material properties of the cortical bone (Foiret et al., 2014; Laugier and Haiat, 2011) and its surrounding and inside medium, assumed to be water, are given in Table 3.3.

Table 3.3: Properties of the cortical bone phantom and water. L and T stand for longitudinal and transverse components

	elastic parameters				velocity		volumic mass
	c_{11}	c_{22}	c_{12}	c_{33}	v_L <i>mm/μs</i>	v_T <i>mm/μs</i>	ρ <i>g/cm³</i>
water	2.25	2.25	2.25	0	1.5	0	1.0
cortical bone	29.6	29.6	17.6	6.0	4	1.8	1.85

In the numerical simulation, a linear array of 128 ultrasonic elements is used to transmit and receive signals. It is located at a proper distance from the cortical shell, and then rotated by steps of 45 degrees as shown on Fig. 3.3(a). This gives 8 positions of the transducer array surrounding the bone phantom. Considering the special geometry of the bone phantom considered here, an additional position, corresponding to a rotation of 160 degrees, shown in Figure 3.4(a), has been considered to enhance the quality of the final reconstructed image. The emitted signal is a 3.5MHz sinusoid pulse modulated by a Gaussian envelop, with a bandwidth of 1MHz. We use SimSonic2D (Bossy et al., 2004a) to simulate the wave propagation and record the temporal signals measured by the transducer array. The simulation grid is set as the 1/60 of the wavelength in water, which is enough to avoid numerical dispersion. The reference is simply defined as homogeneous water, and the boundary conditions are PML (Perfect Matching Layer).

Here, SimSonic2D is used only to simulate the propagation in the inspected medium. For the forward and adjoint problems in the reference medium (homogeneous water), we have preferred an analytic formulation based on the following assumptions:



(a)

Figure 3.3: the numerical simulation setup

- the elements of the transducer array are small enough and can be considered as point-like sources,
- the 3D free space Green's function is usable, although the SimSonic simulation is 2D.

These assumptions allow to perform this simulation step without computational cost compared to the purely numerical approach. The analytic formulation is governed by the following expressions:

$$u_0(\mathbf{x}, \mathbf{x}_e, t) = e(t) \cdot \frac{\delta(t - r/v)}{r} \quad (3.8)$$

$$u_0^\dagger(\mathbf{x}, \mathbf{x}_e, t) = y(T - t) \cdot \frac{\delta(T - t + r/v)}{r} \quad (3.9)$$

$$r = \|\mathbf{x} - \mathbf{x}_e\| \quad (3.10)$$

Chapter 3. Cortical bone imaging by Time Domain Topological Energy

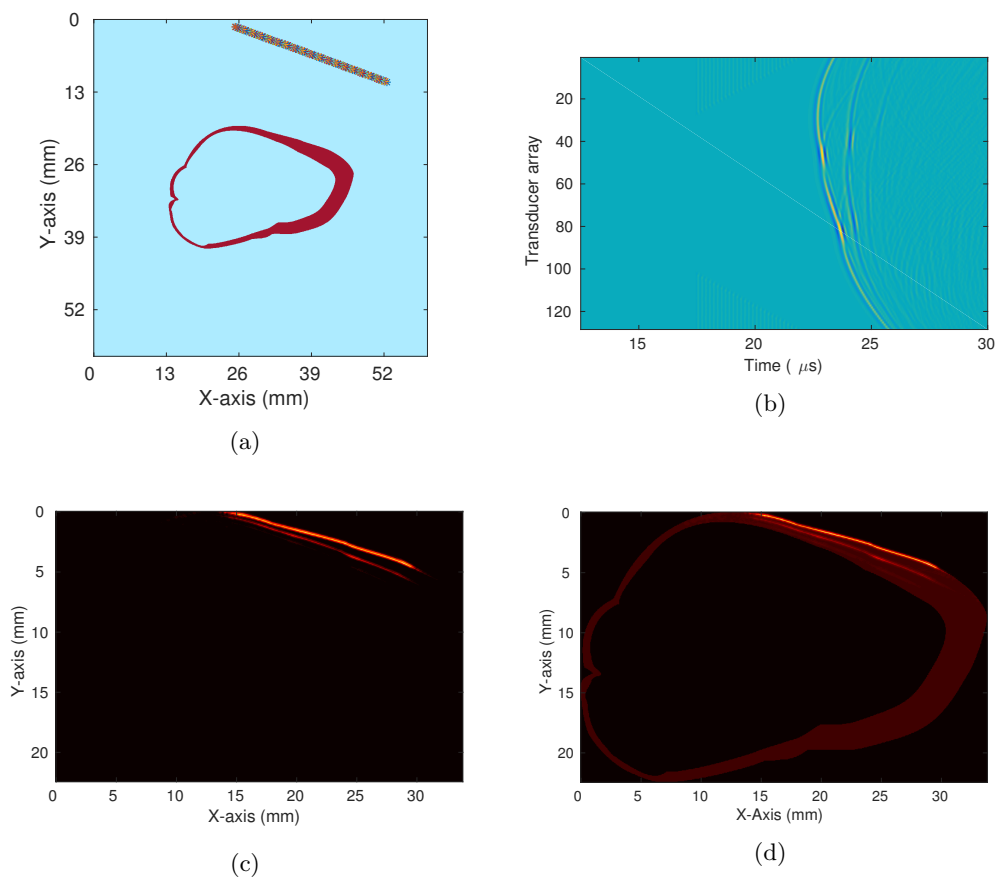


Figure 3.4: (a) numerical simulation setup with the transducer array at 160 degrees, (b) received signals (c) TDTE image and (d) TDTE image and original map

where $u_0(\mathbf{x}, \mathbf{x}_e, t)$ is the field generated at \mathbf{x} by an array element at \mathbf{x}_e (same notation for u_0^\dagger), $e(t)$ is the excitation, and $y(T - t)$ represents the time reversal of the received signal from the inspected medium (the received signal from the reference medium in the forward problem is 0). Then, the TDTE image is calculated by the formula 3.73.8. Fig. 3.4(a) illustrates the considered configuration when the transducer array angle is 160 degrees. The B-scan view of the received signals is shown on Fig. 3.4(b). The resulting TDTE image is shown on 3.4(c), overlapped with the original Map on Fig. 3.4(d).

For each position of the probe with respect to the cortical shell, an independent image is obtained by applying one-time adjoint method at this position. For all positions, the reference medium remains unchanged, made of homogeneous water. We finally sum all the images obtained for each angle to reconstruct the complete image shown on Fig.3.5(a). To validate this result, the obtained image

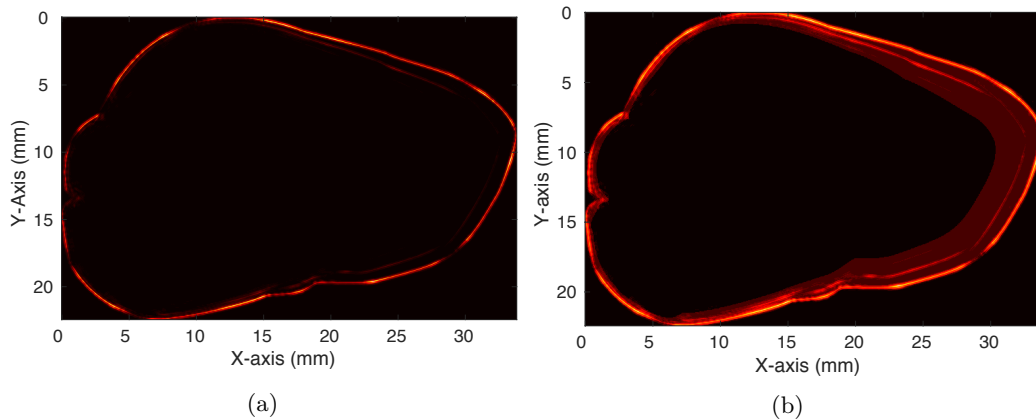


Figure 3.5: (a) reconstructed image of the cortical bone by TDTE, (b) reconstructed and original images of the cortical bone

is superposed with the original image on Fig.3.5(b). We clearly observe that the external boundary is reconstructed precisely. However, the internal boundary is not clearly visible, due to the strong contrast between the cortical bone and water.

3.3 Result Discussion

By applying directly TDTE to cortical bone imaging, we can see some impressive result, with the external boundary that is recovered precisely. The remaining difficulty is that the interior structure of the cortical bone is difficult to identify and is not found at the correct position. In the next section, we will discuss the reason of this mismatch of the internal boundary, and also the influence of the time interval and the sampling frequency in the integration of (3.7).

3.3.1 Velocity mismatch

On Fig. 3.5(b), we can observe that the internal boundary is weak and not located at the correct position, while the external boundary appears correct. To understand this situation, we need go back to the reference medium, which is assumed to be water materials. In the reference medium, the waves travel in water, while the echoes reflected from the internal interface propagate in bone with a larger velocity. Here is the mismatch between the real experiment and the reference medium. This explains why the external boundary is correct, while the internal boundary is misplaced.

Chapter 3. Cortical bone imaging by Time Domain Topological Energy

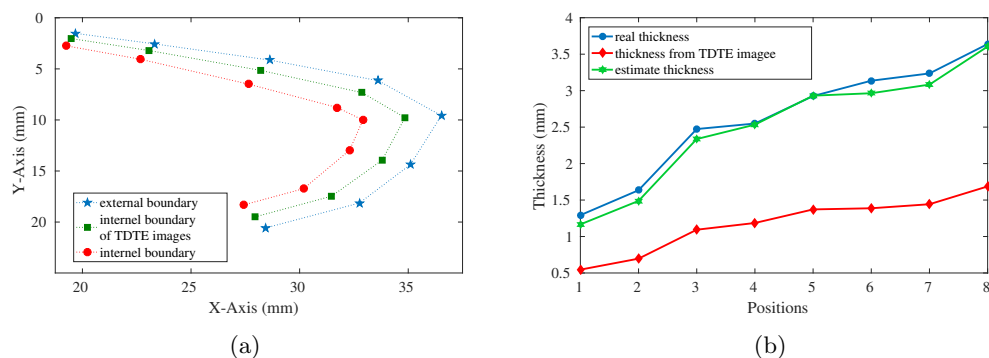


Figure 3.6: (a) the points locations chosen in TDTE image and original image, (b) the estimated cortical thickness and real thickness corresponding to the chosen points

According to this principle, the position mismatch ratio can be approximated by the velocity ratio $\sigma = v_b/v_w \approx 2.67$ from Table 3.3. In order to validate this ratio, we select several points on the external boundary of the TDTE reconstructed image. The corresponding positions are shown on Fig. 3.6(a), where the red circles describe the internal interface obtained from the numerical map, while the blue stars correspond to the internal interface resulting from the reconstructed image. On Fig. 3.6(b), the red solid line represents the thickness obtained from the adjoint method, and the green solid line the thickness corrected by applying our correction factor σ . This green line appears to be very close to the blue line that corresponds to the real thickness, which demonstrates that mismatch of internal boundary is caused by the velocity mismatch.

Another approach to validate this explanation is to replace water material by a homogeneous fluid whose longitude wave-speed is 4000 m/s, which is same with cortical bone. By keeping the rest parameters unchangeable, we run the above simulation again. The corresponding TDTE image and its reconstruction with original images of the cortical bone is shown in Fig. 3.7, where it can be observed no more mismatched reconstruction on both external and internal boundary. However, in the real experiment, the longitude wave-speed cannot be changed as our expectation, two strategies have been proposed in next Chapters to solve the mismatch problem.

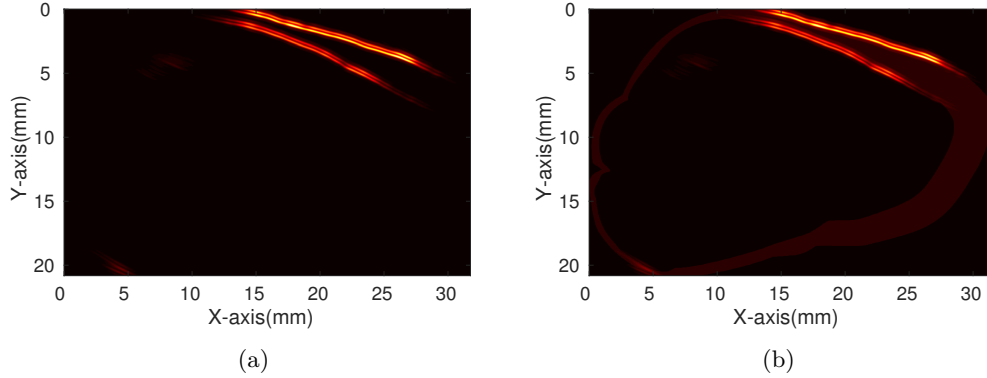


Figure 3.7: the water is changed by homogeneous fluid longitude wave-speed is 4000 m/s: (a) the TDTE image, (b) its superposition with original map

3.3.2 Sampling frequency and time interval in TDTE integration

Basically, TDTE imaging calculates the integration of two wave-fields in space and time domain. In this chapter, the numerical simulation of two wave-field is taking place in a homogenous fluid, where exist an analytical solution of wave-filed displacement, instead of recording by the numerical simulation software. If the reference medium is not a mono-medium, there is no analytically solution for wave-field displacements, which must be recorded by the simulation software. This will require a significant storage for the forward and adjoint simulation. So, the down sampling of wavefield on the time domain and decrease the time interval of integration are very important, which could reduce the required storage.

The spatial resolution of the TDTE image is obviously influence by the simulation grid, that represents an important parameter of the numerical simulation. The space resolution in simulation should be chosen according to the stable condition of the SimSonic2D. The following discussion is based on this precondition. Another two impact factors of TDTE is the time interval of integration and the sampling frequency of wavefield in time domain. In order to evaluate the two influence factors, we considering the above numerical simulation when the array located in 160 degree. According to Eq 3.8, the wave field is in the form of amplitude of received signal, so the sampling of wavefield in time domain can be represents by the sampling of received signals.

To evaluate the influence of the sampling frequency during the temporal integration step, we keep the length of time interval constant, and reduce the sampling frequency to $f_e/10$, $f_e/30$ and $f_e/100$, where f_e is the initial sampling frequency

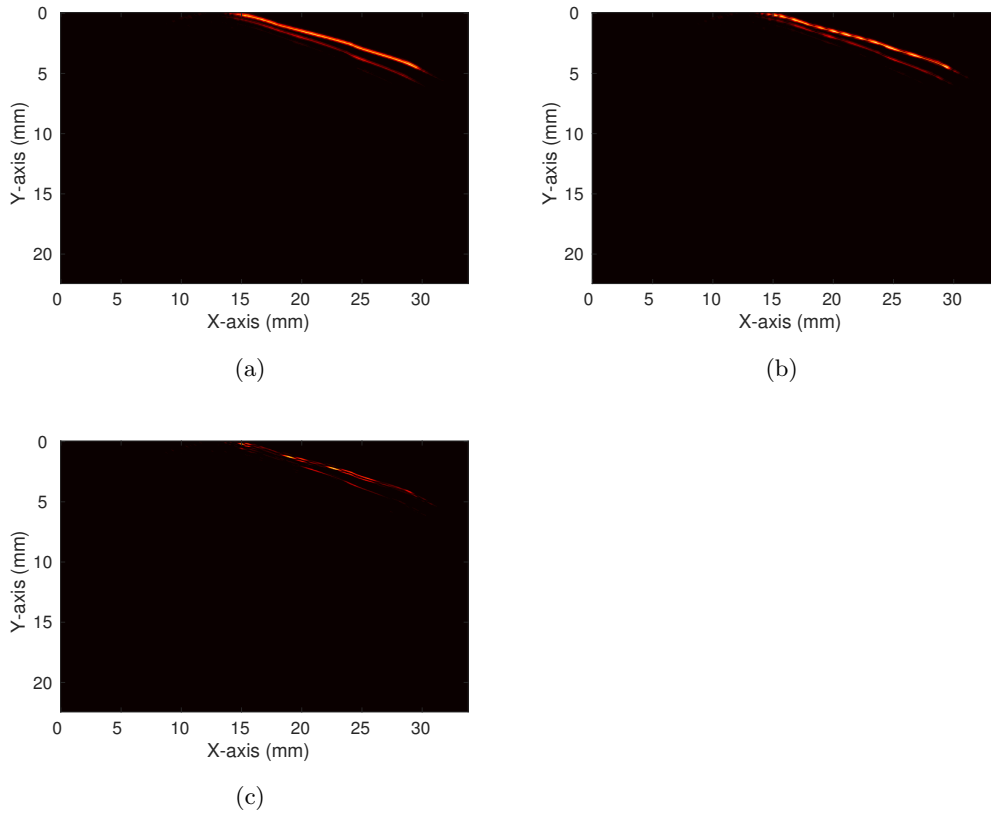


Figure 3.8: TDTE image for an integration frequency (a) $f_e/10$, (b) $f_e/30$ and (c) $f_e/100$

of the received signal used in previous section . The obtained result under such sampling frequencies are shown on Fig. 3.8, we observe here that the intermediate frequency $f_e/30$ can be considered as acceptable. It means that under the situation of assuring the imaging resolution, the storage requirements are decreased 30 times.

Since the two main echoes are main interest in cortical bone imaging, the influence of long coda after the main echoes is unknown. To evaluate the influence of time duration of coda, we chose three different time intervals. We start with a time interval that is only contains the two main echoes, which is $[0, 30]\mu s$, the corresponded TDTE image and its logarithm scale are shown in Fig. 3.9, where the cortical bone can be observe in both linear and logical scale.

Then, we increase the time interval to $[0, 40]\mu s$, the corresponded results are shown in Fig. 3.10, where the linear scale TDTE image is same with Fig. 3.9(b), the logarithm scale contains more information, marked by white arrow.

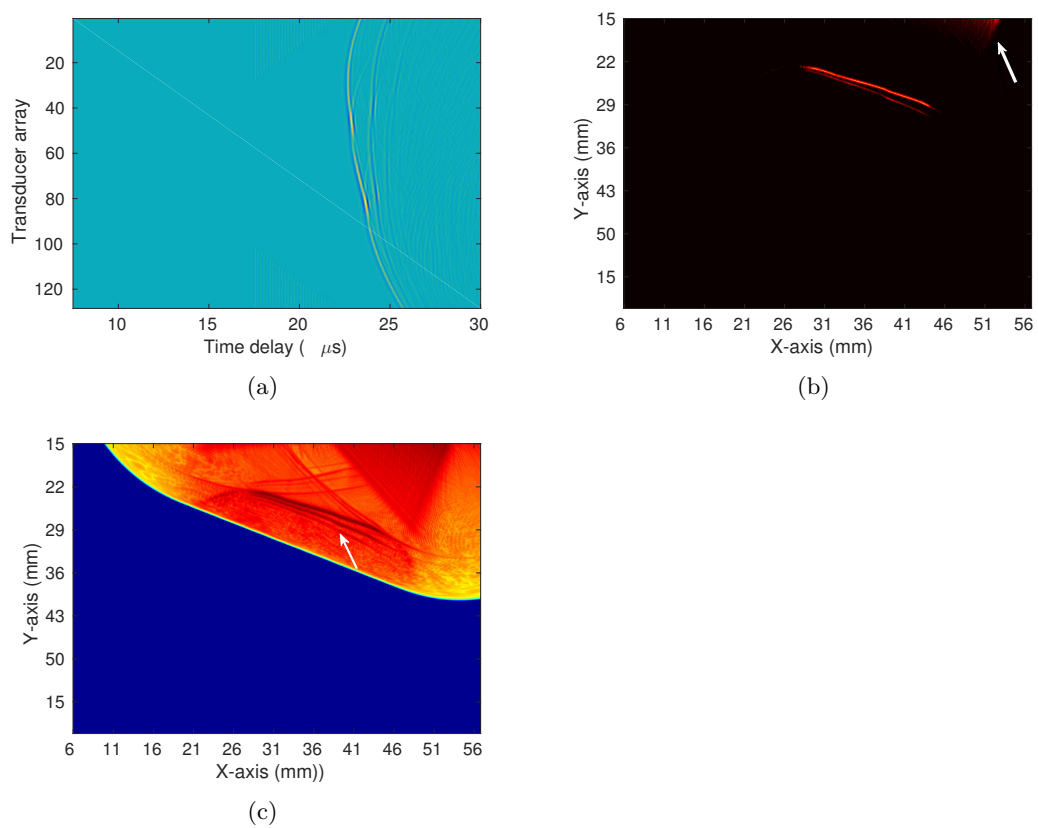


Figure 3.9: the received signal with short time duration and its TDTE image

Chapter 3. Cortical bone imaging by Time Domain Topological Energy

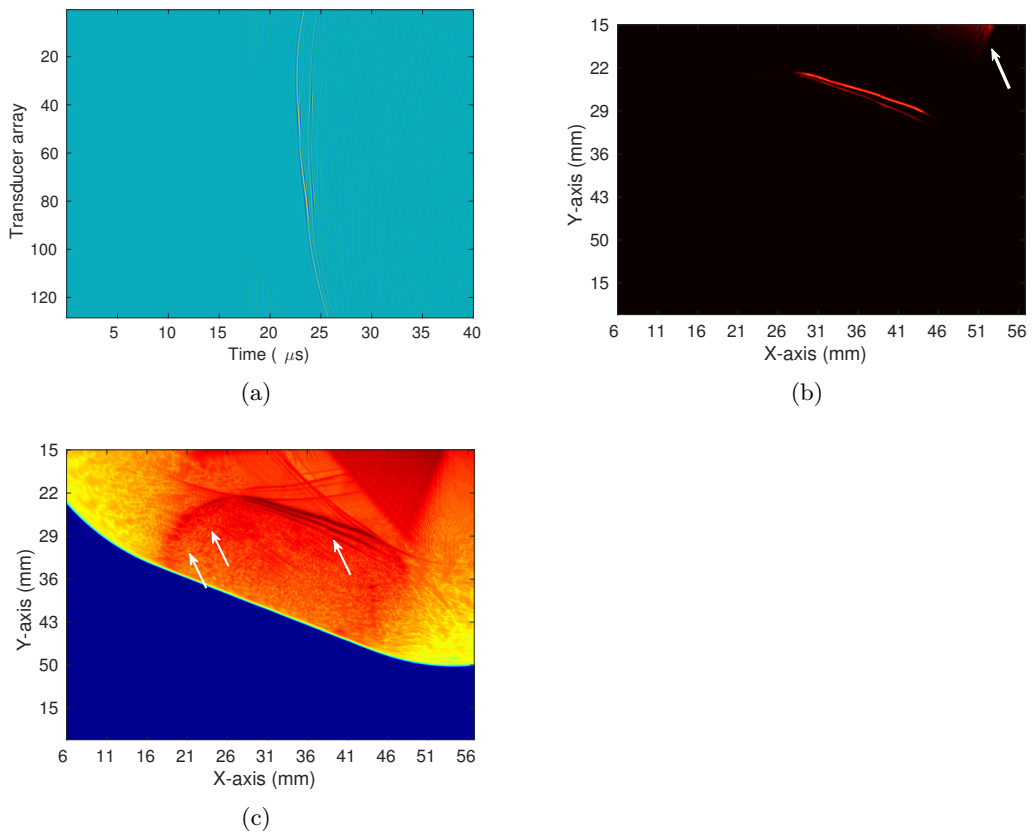


Figure 3.10: the received signal with medium time duration and its TDTE image

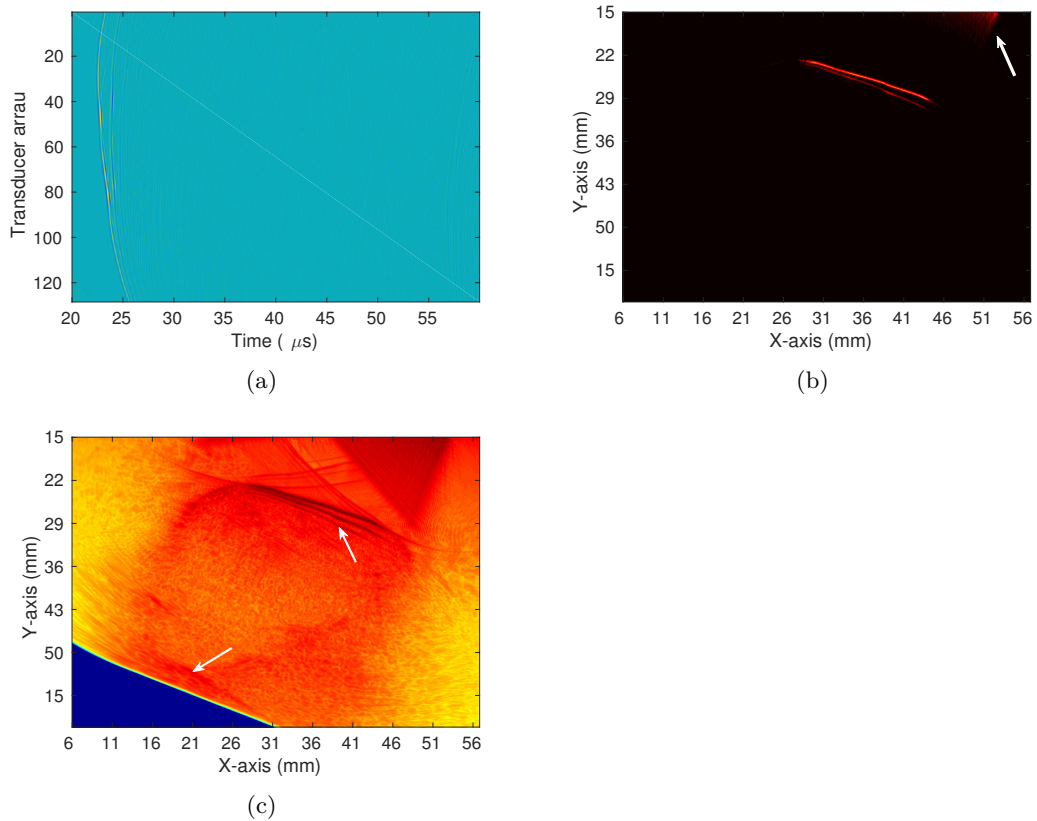


Figure 3.11: the received signal with long time duration and its TDTE image

To exam if the logarithm scale TDTE can provide deeper structure, we continue increase the time interval to $[0, 60]\mu s$, the corresponding results are shown in Fig. 3.11, where the TDTE image is also the same the Fig. 3.9(b). The logarithm scale TDTE image can provide more information of deeper structure, which is the contrary side of cortical bone. However, it is very rough imaging for the deeper structure, with some certain degree of deformation .

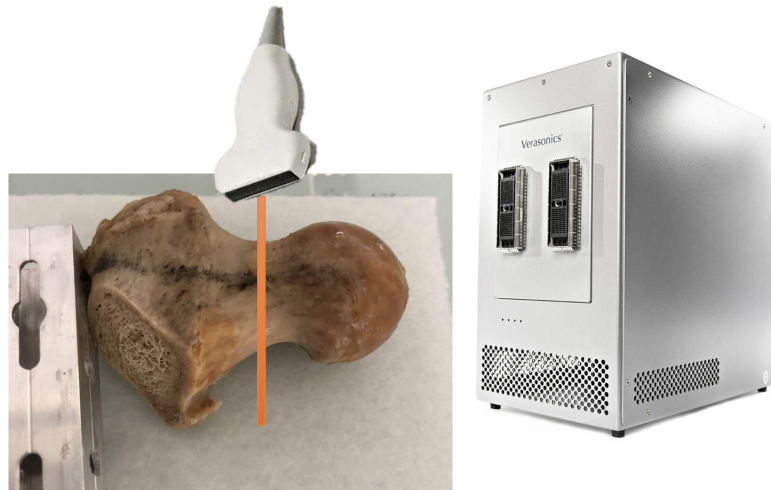
Looking at these figures, we observe that the longer time integration we used, the deeper information of structure we can obtain, and the precision is decrease along to the deeper structure. If we only need the front portion of cortical bone, the received signal only contains the two main echoes is sufficient.

3.4 *in vitro* femur neck cortical bone validation

The numerical simulation of TDTE shows a promising results on imaging of cortical bone, we will evaluate the TDTE imaging on the femur neck cortical bone

Chapter 3. Cortical bone imaging by Time Domain Topological Energy

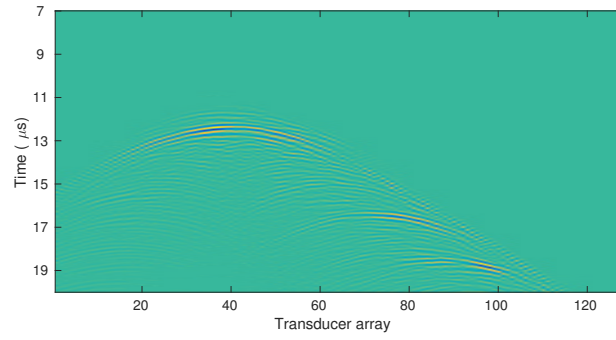
in vitro. in this subsection. The in-vitro validation performs on human femur neck specimens, which are provided by LIB (Laboratoire d’Imagerie Biomedicale), according to the French program for voluntary corpse donation to science. The donors provide their tissues are informed written consent in accordance with legal clauses stated in the French code of public health. The soft tissue of femur has been removed. The femur was placed in a water tank, and the ultrasound probe was immersed in water for signal acquisition. The probe was placed along the orange line, illustrated in Fig. 3.12(a), in order to produce an image in the cross-section view of femur neck. The inter-element pulse-echo signals were recorded using a fully programmable ultrasound system (Vantage 64LE, Verasonics Inc., Redmond, WA, USA) equipped with a 5.2 MHz linear array transducer (L7-4 ATL, Bothell, WA, USA; pitch 0.298 mm, 128 elements).



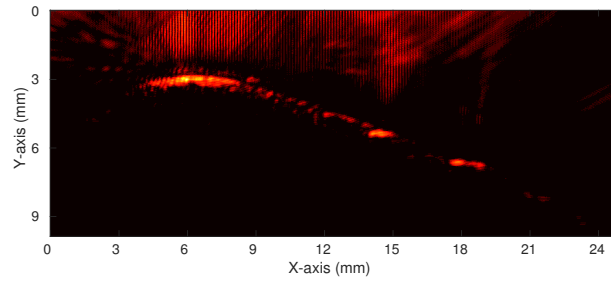
(a)

Figure 3.12: the experimental setup for *in vitro* cortical bone imaging

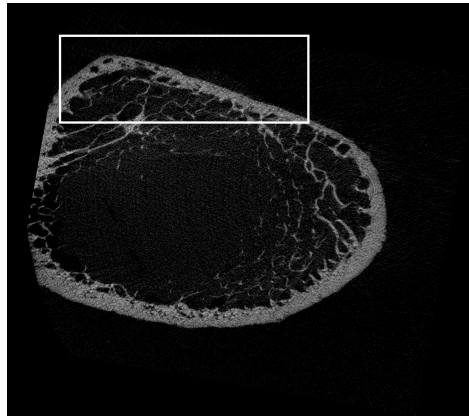
The reference medium is set to be water material, which is same with the numerical simulation. We make signal acquisition in one specific location with micro CT image has been measured and process the received signal to obtain TDTE image. The B-scan view of received signal and the corresponding TDTE image are shown in Fig. 3.13. It should be noticed that the CT measurements contain more than 1000 image slices, which is difficult to locate the precise slice corresponded to the position of TDTE measurement. As a consequence, some slight mismatch may exist between them.



(a)



(b)



(c)

Figure 3.13: (a) the B-scan view of received signal in position 1, (b) the corresponding TDTE image, (c) the micro CT image of femur neck, where the white rectangular is the reconstructed area

Chapter 3. Cortical bone imaging by Time Domain Topological Energy

The TDTE reconstruction is shown in Fig. 3.13(b), which the external can be reconstructed well. Since this cortical bone of femur neck is with osteoporosis shown in Fig. 3.13(c), where the endosteal interface is irregular and discontinuous, the internal structure is poorly imaging by TDTE at such circumstance. This result indicates that the iterative procedure of TDTE is required.

CHAPTER 4

TDTE with Sparse Signal Processing for Cortical Bone Imaging

When we try to use TDTE for the cortical bone imaging, the interior structure of the bone remains a challenge due to i) the strong contrast between the bone material and the surrounding soft tissues, and ii) the strong attenuation in bone. Meanwhile, there exist a mismatch of internal boundary of the TDTE reconstruction, caused by the pre-defined reference medium, of which velocity is different from cortical bone. To overcome these difficulties, one possible idea consists in artificially enhancing the echoes reflected from the internal boundary and increase their time delays using adapted signal processing methods. Another strategy is second iteration TDTE by considering the area inside external boundary as cortical bone material in reference medium, which can illuminate the influence of velocity mismatch. However, in the first TDTE iteration, we can use a simplified numerical solver based on an analytical formulation as the reference medium reduces to a homogeneous fluid, and the computation requirement is small. For the second iteration, the reference medium is modified and now includes a domain made of bone material, resulting from the identification of the external interface of the cortical bone. Consequently, the solver is now based on a purely numerical approach, and the storage and computation requirements increase significantly.

In this chapter, we will introduce the first strategy to enhance the internal boundary and amend its position mismatch by sparse signal processing method. For only this purpose, the second step of TDTE is no more required.

During the last years, the sparse signal processing appears as an attractive approach, particularly in signal and image reconstruction. In our case, the objective is to localize the echoes from the internal boundary, mainly through time delays. For that purpose, we use the Orthogonal Matching Pursuit (OMP) (Mor et al., 2010) introduced in Chapter 2 to separate the two main echoes corresponding to external and internal boundary. Once we have identified the second main echo that corresponds to the internal boundary, it becomes possible to artificially amplify its amplitude and increase its time delay before applying TDTE.

4.1 Sparse Signal Processing

4.1.1 Signal Model

In ultrasound echography, given a Gaussian pulse excitation illuminating the cortical bone sample, the received signal of QUS measurements can be modeled in the time domain by P superimposed Gaussian pulses, as follows:

$$y(t) = \sum_{i=1}^P A_i \exp^{-s_i(t-\tau_i)^2} \cos[2\pi f_i(t - \tau_i) + \phi_i] + n(t) \quad (4.1)$$

where s_i denotes the bandwidth factor, f_i the central frequency, τ_i the time delay, ϕ_i the phase and A_i the amplitude of the i -th echo. In this expression, $n(t)$ evaluates the error between the simplified model and the effective measurement.

4.1.2 Simplified version of OMP

In Chapter 2, we have proposed a complex version of OMP, which is used to estimate the parameters of the Gaussian pulses: bandwidth, time delay and frequency. In TDTE imaging, our objective consists in the reconstruction of weak and overlapped echoes, and the practical estimation of all parameters is expensive and unnecessary in this case. Since the amplitude spectrum of a Gaussian pulse reduces to its envelope, the Gaussian pulse can be characterized by only two parameters, bandwidth and time delay. Consequently, the complex-valued version of OMP proposed in Chapter 2 can be simplified here. The main difference between the two approaches is that we do not need the complex formulation steps. Meanwhile, the size of dictionary is only containing the possible combinations of time delays and bandwidth, which is smaller than the dictionary in Chapter 2.

Thus, the model (4.1) can be simplified as follows:

$$\tilde{\mathbf{y}}(t) \approx \sum_{i=1}^M A_i \mathbf{d}(s_i, t - \tau_i) + n(t) \quad (4.2)$$

where $\tilde{\mathbf{y}}(t)$ represents the envelop of the received signal $\mathbf{y}(t)$. It should be noticed that there is an approximated relation in Eq. (4.2), which will be deliberated in Appendix. The envelop of the i -th echo is expressed as

$$\mathbf{d}_i \equiv \mathbf{d}(s, t - \tau_i) = \zeta e^{-s_i(t-\tau_i)^2}. \quad (4.3)$$

where ζ is a normalized constant. It results therefore that the discrete signal model can be represented as

$$\mathbf{y} = \mathbf{D}\mathbf{x} + \mathbf{n} \quad (4.4)$$

where $\mathbf{y} = [\tilde{y}(t_1), \tilde{y}(t_2), \dots, \tilde{y}(t_N)]$ is the sampled envelop of the received signal, $\mathbf{x} \in \mathbb{R}^M$ is the vector of coefficients, which indicates the amplitudes and locations of the different echoes, $\mathbf{D} \in \mathbb{R}^{N \times M}$ is the dictionary made of the columns \mathbf{d}_i . In Chapter 2, we have seen that the dictionary results from all the possible combinations of the Gaussian parameters, including bandwidth s , frequency f and time delay τ , and how to seek the suitable sampling intervals for each of these parameters. In the simplified version used here, only s and τ are required.

As described in Chapter 2, the possible values for each parameter are sampled on M discrete points. We define an *a priori* pertinent range for s and τ , these ranges being subdivided into L and S regular intervals, respectively. Thus, the dimension of the over-completed dictionary is $M = L \times S$, with $M \gg N$. Each coefficient of \mathbf{x} corresponds to a specific combination of s and τ , and (4.2) can be rewritten as follows:

$$\mathbf{y} = [\mathbf{d}(\Theta_1) \quad \mathbf{d}(\Theta_2) \quad \cdots \quad \mathbf{d}(\Theta_M)]\mathbf{x} \quad (4.5)$$

where

$$\Theta_m = [s_l, \tau_s],$$

$$l \in [1, L], s \in [1, S], \mathbf{x} \in \mathbb{R}^{1 \times M}$$

Meanwhile, since the signal model is only the envelop in real form, the complex-valued version of OMP needs to be modified to the real version, which is the standard version of OMP shown in Algorithm 2-1.

We have applied this new OMP treatment to the temporal signal shown on Fig. 4.1(a) with a signal model that reduces to two Gaussian pulses. The obtained result is illustrated on Fig. 4.1(b) and we can conclude that the two overlapped pulses in the initial signal are correctly reconstructed.

4.1.3 Model based OMP without building dictionary

Considering in the array signal processing for imaging purpose, the possible interval of time delay will be much larger than mono transducer in Chapter 2, leading to

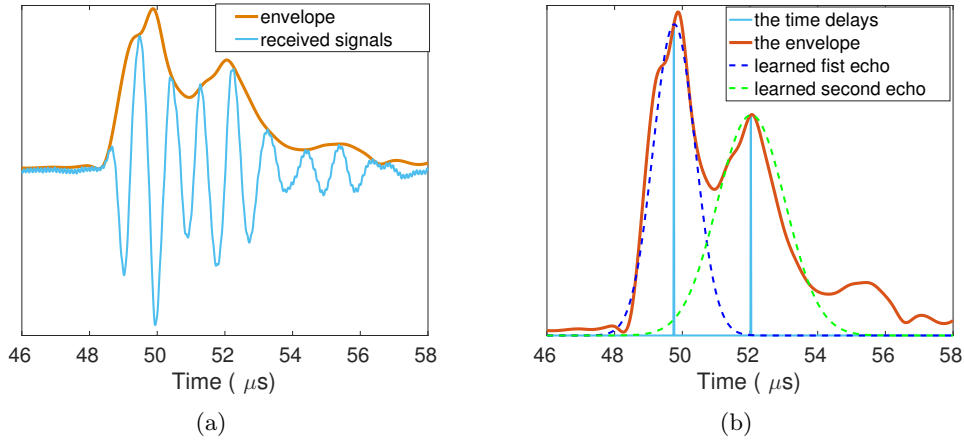


Figure 4.1: (a) received signal and envelop, (b) envelopes reconstructed by OMP

a large dimension of dictionary. To avoid the computation burden, there is another version of OMP combining dictionary learning, which can avoid to build the over-complete dictionary containing all the possible combinations of the parameters.

Physically we can consider that the different echoes coming from the external and internal interfaces of the cortical bone look similar, up to a time delay and possible small deformation. Mathematically, the time delay with respect to the emitted signal can be realized by a unitary shift operator in the time domain. And the deformation can be adapted by least square minimized optimization. Doing this, it is no more necessary to build a complete dictionary.

Firstly, the signal model from (4.1) can be interpreted in terms of a linear combination of time delayed versions of the emitted signal $e(t)$, without distortion. Concerning the dictionary \mathbf{D} , each column is obtained from a unitary time delay applied to the former one, up to the first column \mathbf{d}_1 that corresponds to the emitted signal. This operation can be illustrated by applying a right unitary-shift operator

defined by the following matrix:

$$\mathbf{T} = \begin{pmatrix} 0 & 1 & \dots & 0 \\ 0 & 0 & \ddots & \vdots \\ \vdots & \vdots & \ddots & 1 \\ 0 & 0 & \dots & 0 \end{pmatrix} \quad (4.6)$$

In this case, the columns are built as follow:

$$\begin{aligned} \mathbf{d}_1 &= \text{emitted signal} \\ \mathbf{d}_i &= \mathbf{T}\mathbf{d}_{i-1}, \quad i \geq 2 \end{aligned} \quad (4.7)$$

However, the version of the dictionary considers that the different echoes are just time-delayed and keep a constant temporal shape. In our case, it is necessary to take into account a possible deformation of the echoes. By applying standard OMP, the error of reconstruction will be large if we chose the K-sparsity constrained OMP, and the sparse solution will contain more non-zeros entries than expectation if we chose error constrained OMP. Obviously, due to the excessive simplicity of the dictionary built by (4.7), it will result in wrong time delays of the echoes, or more columns of the dictionary need to be superimposed to match the received signal.

For that purpose, we introduce a column updating method to deal with the deformation of the echoes, least mean square optimization is used here to searching the right value of bandwidth factor. The principle under the procedure is: firstly, an initial uncompleted dictionary is assumed, where the most correlated column with target signal is chosen; secondly, the least mean square optimization is used to minimize the difference between the chosen column and target signal by searching the bandwidth factor.

As discussed in the above section, the echoes can be characterized by their bandwidth and time delay, the envelop of the i -th echo being expressed as

$$\mathbf{d}(s, t - \tau_i) = \exp\{s_i(t - \tau_i)^2\}. \quad (4.8)$$

Updating the selected column consists in modifying its bandwidth factor s . During the k -th iteration of OMP, the most correlated column $\mathbf{d}^{(k)}$ and the corresponding $\mathbf{x}^{(k)}$ have been obtained. then the selected column is modified in the frame of the Gaussian model according to the following relationship:

$$\hat{\mathbf{d}}^{(k)} = \arg \min_s \{\mathbf{r}^{(k-1)} - x^{(k-1)}\mathbf{d}^{(k-1)}(s)\} \quad (4.9)$$

where $\mathbf{r}^{(k-1)}$ and $x^{(k-1)}$ represent the residual and vector of coefficients from the $(k - 1)$ -th iteration. This minimization can be easily solved by first order derivative-based search algorithm.

This Least square minimization embedded with OMP is called Model Based OMP, which have the same reconstruction with the previous OMP (over-completed dictionary). The advantage of model based OMP is the smaller dimension of dictionary. Both OMP have the similar performance.

4.2 Additional processing

4.2.1 Envelope processing

There are several ways to determine the envelop of the received signal $\tilde{\mathbf{y}}(t)$ such as peak connection, Hilbert transform, root-mean-square. Since the received signal may include some temporal deformations and high frequency noise, a hybrid approach should be applied to obtain an acceptable envelope for processing with the model based OMP. The hybrid approach is described as:

1. use the Hilbert transform to obtain a roughly envelope with high frequency noise,
2. perform peak interpolation to eliminate the high frequency noise: a smooth envelope $\tilde{\mathbf{y}}(t)$ can be obtained using spline interpolation between local maxima separated by enough sample points.

An example of this hybrid approach is illustrated on Fig. 4.2.

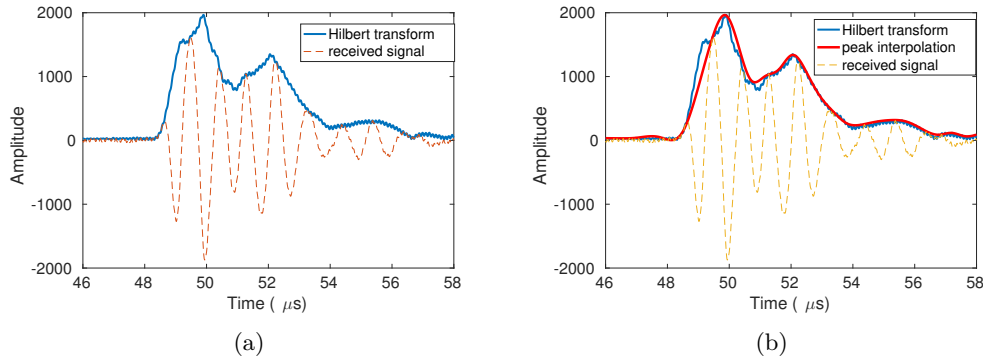


Figure 4.2: (a) the envelope by Hilbert transform (b) peak interpolation of the Hilbert transform

4.2.2 Curve fitting

By applying the OMP to the received signal, we cannot be sure to obtain correct time delays in case of strong overlap between the different echoes that may come from different angles. For example, the received signals illustrated on Fig. 4.3(a) correspond to the transducer array located at an angle of 225 degrees in the numerical simulation presented in the previous chapter. By applying the OMP method, the time delay for the first echo (corresponding to the external boundary of the bone) is shown on Fig. 4.3(c), similarly Fig. 4.3(d) represents the time delay for the second echo (corresponding to the internal boundary of the bone). On these two figures the evaluated time delays are compared to a high order polynomial curve fit over the different elements of the array. We can observe a mismatch, particularly in the domain between element #100 and element #120, that can be interpreted as a consequence of the overlap between echoes coming from different angles. To correct these time delays estimated by OMP, curve fitting is introduced here to fitting the times delays. The fitted time delays of two echoes are shown in Fig. 4.3.

4.3 Numerical simulation

In this section, we use the received signal calculated by the numerical simulation presented in the previous chapter. The objectives here are

1. identify the echo corresponding to the internal interface of the cortical bone,
2. amplify its amplitude to the same level as the echo corresponding to the external interface,
3. back-propagate the modified received signal in the reference medium (homogeneous fluid, classical first step of TDTE).

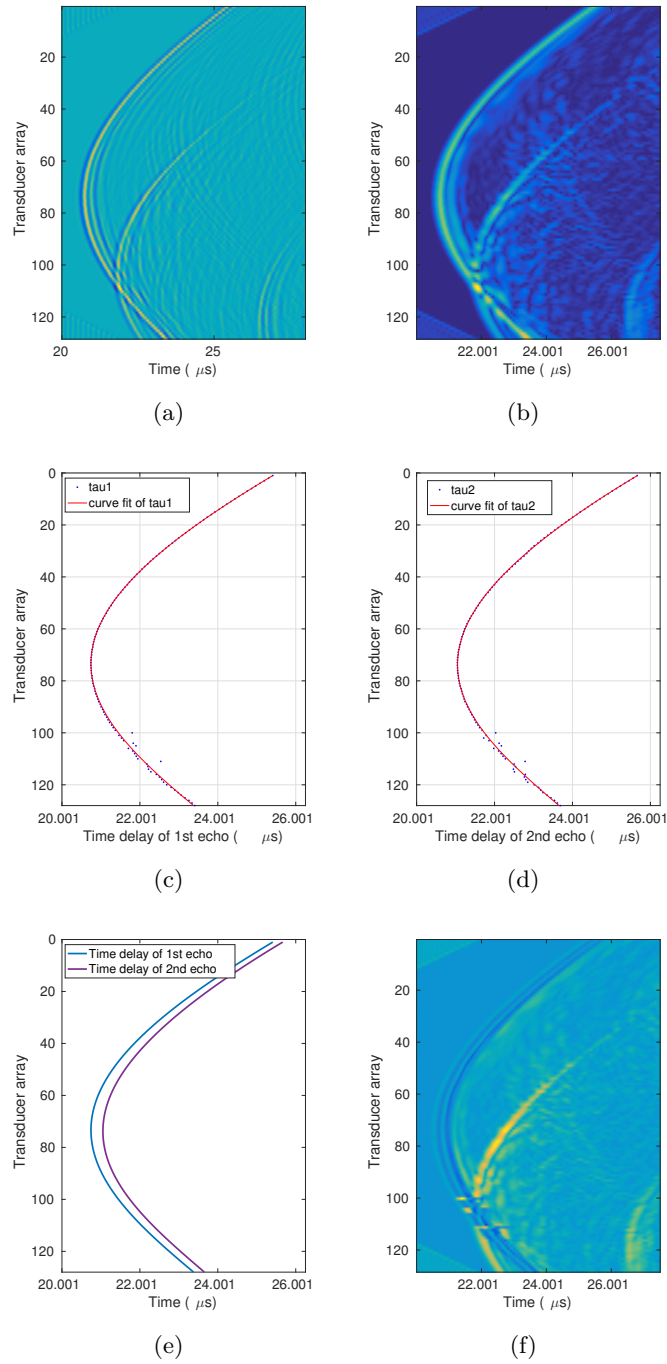


Figure 4.3: (a) received signals for the array located at an angle of 225 degrees (b) its envelop (c) time delays corresponding to the first echo by OMP and fit (d) time delays corresponding to the second echo by OMP and fit (e) time delays after curve fit (f) difference between original and reconstructed envelopes

This process is applied with two different geometrical configurations: continuous part and discontinuity part. Here we give two examples represent two different configurations, which are the array located in 315 degree and 270 degree.

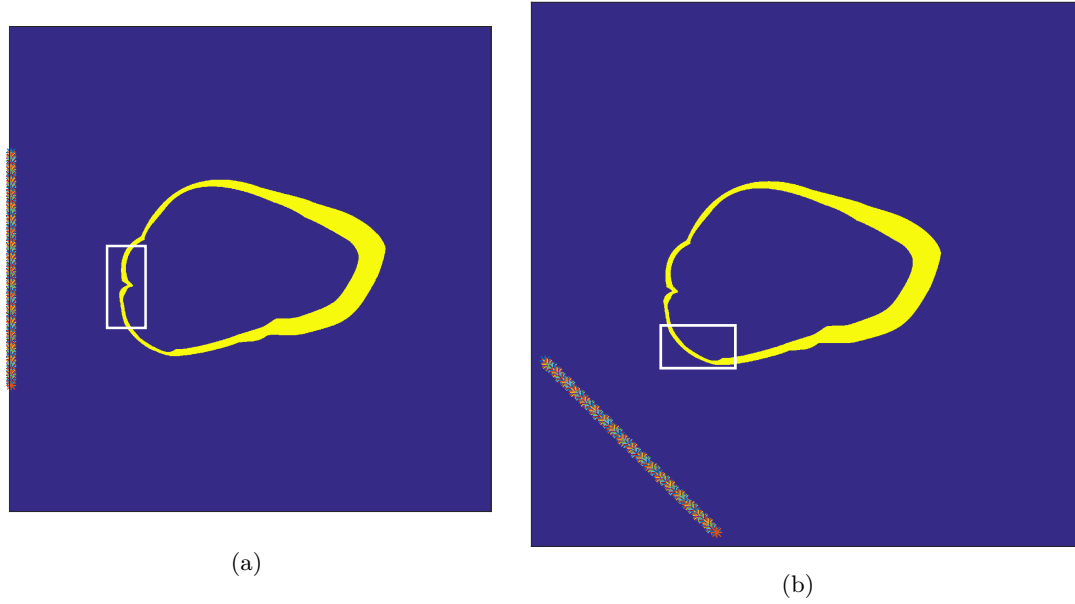


Figure 4.4: the configurations when the array located in (a) 270 degree and (b) 315 degree

We first start with the transducer array located at an angle of 315 degrees, corresponding to a region of continuous external boundary of the cortical bone. The corresponding B-scan view on Fig. 4.5(a) shows the temporal signals received by the different elements of the array. This figure shows a regular wavefront, such that OMP does not have any real difficulty to evaluate the time delays correctly, as shown on Fig. 4.5(b). As discussed in the previous chapter, the location of the internal boundary of the cortical bone does not mismatch the original image, due to the fact that the propagation in reference medium is performed in water, therefore resulting in a propagation velocity mismatch between water and bone. Using the mismatch ratio defined as $\sigma = v_L\{water\}/v_L\{bone\} \approx 2.67$, we can recalculate the second time delay τ_2 according to the expression $\tau_2 = (\tau_2 - \tau_1) * \sigma$. Applying this correction, the modified temporal signals are shown on Fig. 4.5(c), and the image resulting from TDTE and original map on Fig. 4.5(d). On this figure, we observe that both the external and internal boundaries are correctly obtained.

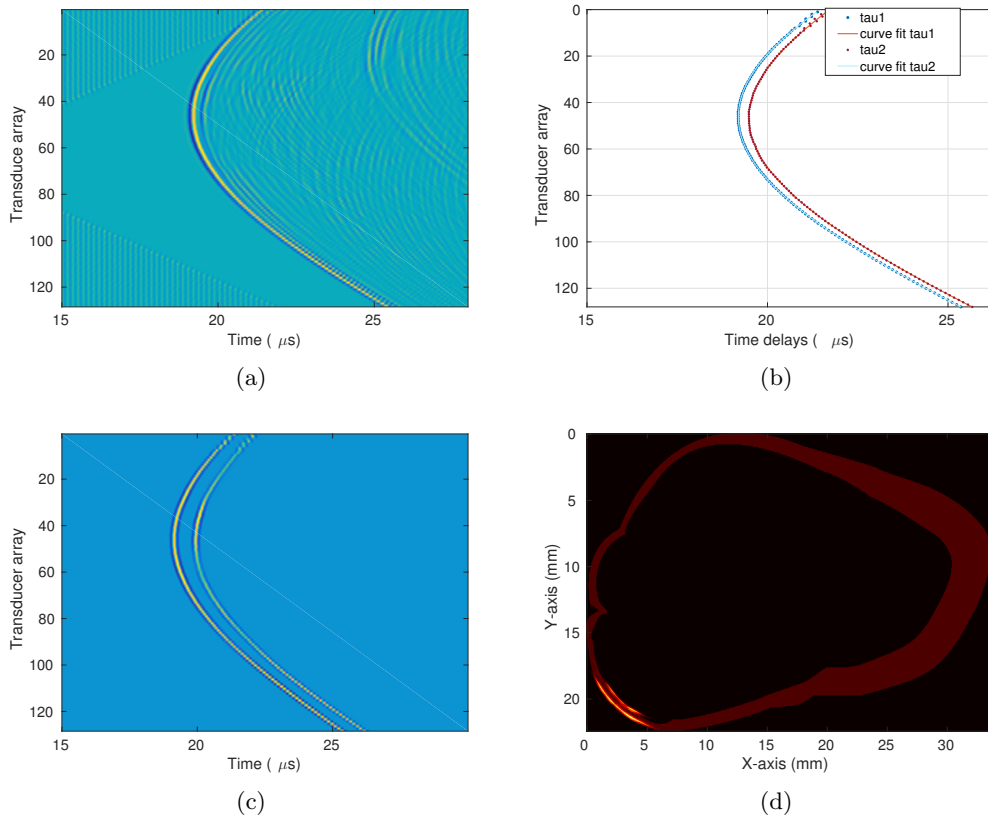


Figure 4.5: (a) received signals for the array located at an angle of 315 degrees, (b) time delays by OMP, (c) corrected time delays and amplitudes, (d) reconstructed TDTE image

The second geometrical configuration corresponds to the array located at an angle of 270 degrees, where the front interface of the cortical bone sample shows a spatial discontinuity. The corresponding B-scan view of received signals shown on Fig. 4.6(a): we clearly see that the wavefronts are significantly more complex, compared to the previous case. In particular, we can visually identify two different wavefronts, and an intersection zero between elements #60 and #70. The presence of two wavefronts can be easily understood as resulting from the inflection of the external boundary of the sample for this particular angle. Due to the finite thickness of the bone sample, this means that the received signals are mainly made of four echoes, and the sparsity of OMP has to be reset to 4 consequently. The time delays obtained by the 4-sparsity OMP process are shown on Fig. 4.6(b). Applying the same correction to the second series of time delays as in the previous case, the modified received signals are shown on Fig. 4.6(c). Fig. 4.6(d) shows the reconstructed image obtained by TDTE: once again we clearly see that both the external

and internal boundaries are correctly obtained, on both sides of the geometrical inflection.

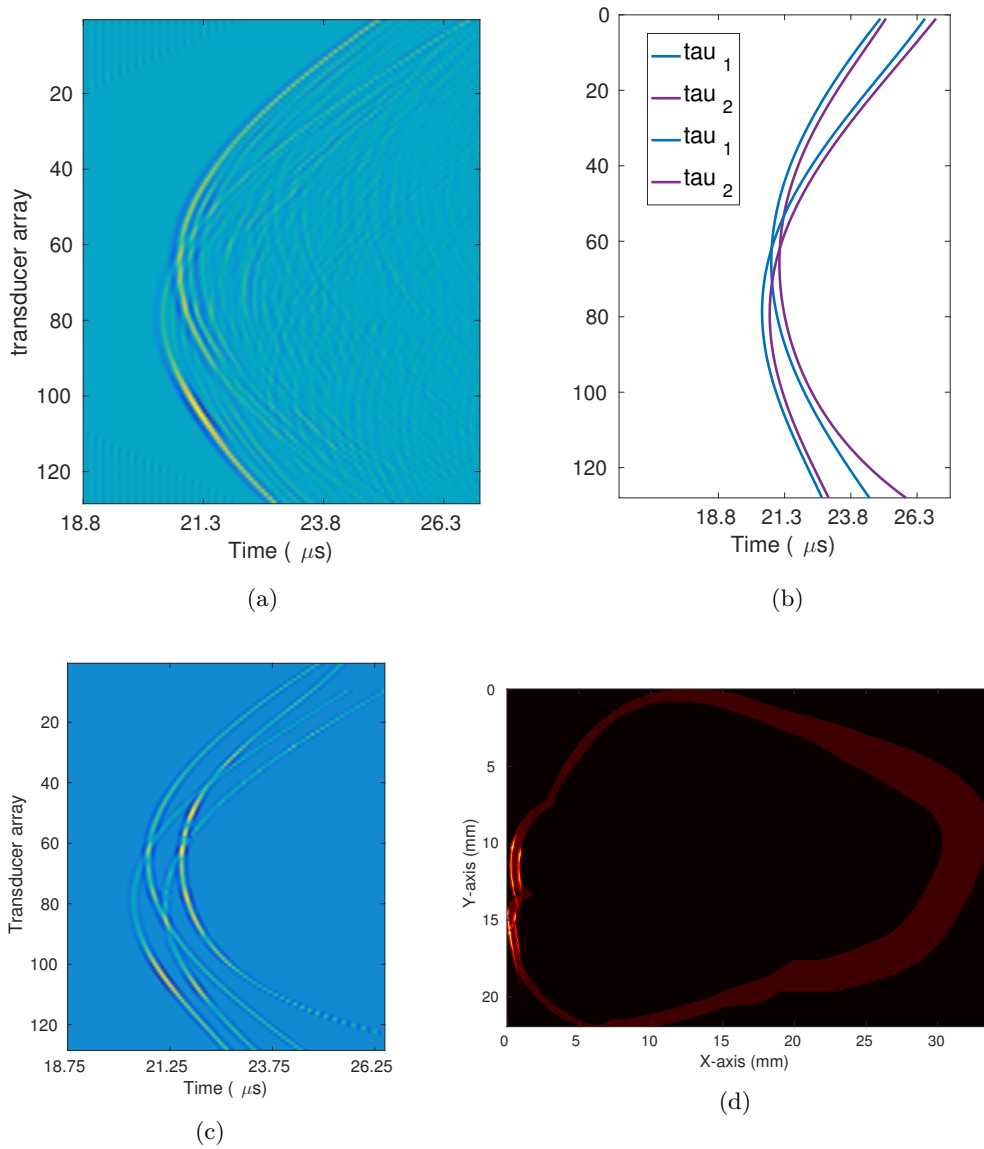


Figure 4.6: (a) received signals for the array located at an angle of 270 degrees, (b) time delays OMP, (c) recorrected time delays and amplitudes, (d) reconstructed TDTE image

The same process can be repeated for all simulated angles of the transducer array with respect to the bone sample, and the different TDTE images obtained for each angle are finally assembled together. The complete TDTE image is superimposed

on the original image, which is shown in Fig. 4.7 that the internal boundary is visible same with the external boundary and without mismatch.

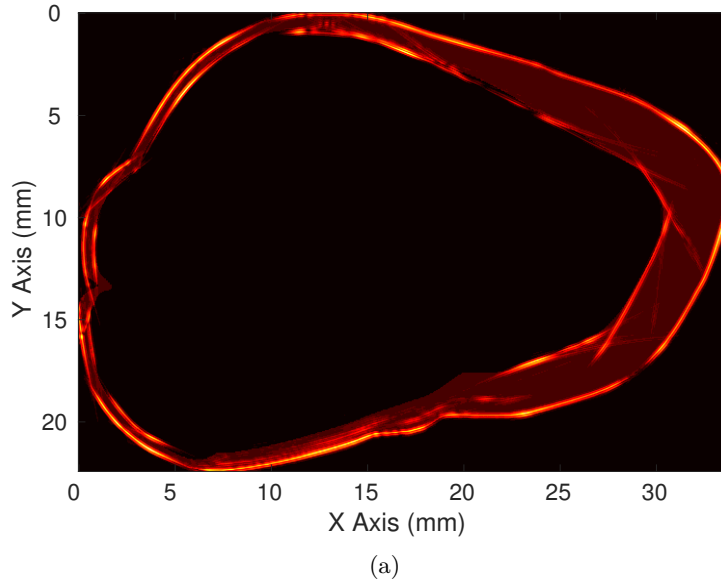


Figure 4.7: full reconstructed image of the cortical bone sample with TDTE and OMP, superimposed with the original map

4.4 Experimental validation using the cortical bone phantom

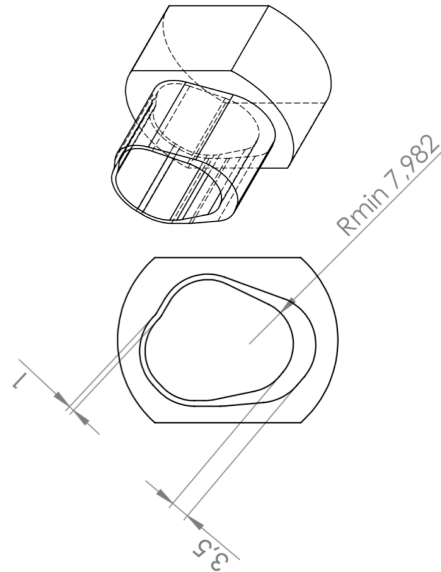
In order to validate the former approach, we have run an experiment with a cortical bone-mimicking tube (Sawbone, Pacific Research Laboratory Inc., Vashon, WA) with a geometry obtained from CT measurements of a real portion of femoral neck. Sawbone consists in short glass fibers embedded in an epoxy resin. The fibers of the manufactured tube are aligned with the axis of the cylinder. Thus this sample is transverse isotropic, the plane of symmetry being perpendicular to the axis of the cylinder. The material properties of sawbone are summarized in Table 4.4, in addition to previously measured ((Minonzio et al., 2011)) and usually considered as representative (Foiret et al., 2014; Laugier and Haïat, 2011) characteristics of the human cortical bone. Figs.4.8(a) and 4.8(b) show the phantom and its main geometrical properties.

	Sawbone	Human bone	Water
$c_L(\text{m} \cdot \text{s}^{-1})$	2870	3205	4000
$c_T(\text{m} \cdot \text{s}^{-1})$	1520	1495	
$\rho(\text{kg} \cdot \text{m}^{-3})$	1640	1879	1850
$s_L(\text{dB} \cdot \text{cm}^{-1} \cdot \text{MHz}^{-1})$	2.63	2.56	
$s_T(\text{dB} \cdot \text{cm}^{-1} \cdot \text{MHz}^{-1})$	8.40	Unknown	

Table 4.1: Comparison of longitudinal and transverse velocities, mass densities and attenuation coefficients between Sawbone (bone-mimicking material) and human cortical bone (mid-diaphysis of the femur), measured in the plane of isotropy. L and T stand for longitudinal and transverse components.



(a)



(b)

Figure 4.8: (a) femoral neck bone phantom, (b) geometrical parameters of the bone phantom

The ultrasonic transducer and receiver is a linear array of 128 cylindrically focused elements (Imasonic, Besancon, France), shown in Fig. 4.9(a), with the following properties:

- focused length: 160 mm \pm 10 mm
- array pitch: 1.1 mm
- center frequency (-6 dB): 1MHz \pm 15%
- bandwidth (-6 dB): 0.6MHz

The transducer array is used in emission to produce a plane wave that propagates in direction of the bone phantom. In reception, the 128 elements work independently, and we record the temporal responses on each element. The probe and the phantom are placed in a water tank (dimension 1.40m \times 1m \times 0.50m, such that the reflections from the tank walls can be neglected). The phantom is located at the focal length of the probe, i.e. 160mm. The excitation signal is a 1MHz Gaussian modulated sinusoid signal of temporal duration 1 μ s. The reflected signals are recorded from $t_0 = 200\mu$ s on a temporal duration of 79 μ s (containing the two main echoes) at a sampling frequency of 80MHz. The value of t_0 corresponds to approximatively twice the focal length of the probe at a propagation velocity of 1.5mm/ μ s (ultrasound velocity in water), thus to the time after which the reflected signals are expected, after propagation from the probe to the sample and back. A multi-channel electronic device (Lecoeur Electronique, Chuelles, France) is used to manage the 128 elements of the probe in reception. *In vivo*, it is impossible to obtain the whole image of the femoral neck, as the transducer array cannot be completely rotated around the femoral neck. So our experiment only tests 6 particular angles (0 degree, 22 degrees, 90 degrees, 140 degrees, 180 degrees and 270 degrees). The bone phantom is fixed on a support, whose rotation is controlled remotely. The complete experimental setup is shown on Fig.4.9. Once the measurements are done for each of the 6 angles mentioned above, the recorded data is processed by TDTE and OMP.

For a center frequency of 1.1MHz, the resolution is not enough to distinguish between the external and internal boundaries of the cortical shell and the corresponding echoes overlap in time. Nevertheless, the OMP allows to evaluate the time delays, even in the case of strong overlap of echoes. Once the time delays have been obtained, it is possible to simulate the received signals at a higher frequency, and the TDTE method produces an image of higher resolution. We have seen previously that the correct location of the inner interface requires a correction ratio to be used on the time delay evaluation. In the particular case of the bone phantom used in this experiment, the velocity ratio is $\sigma = v_b/v_w \approx 1.9$.

As an illustration, we can consider here the particular case of the transducer array located at an angle of 0 degree (cortical thickness $\approx 1mm$). The received signals are shown on Fig. 4.10(a), and the corresponding TDTE image on Fig. 4.10(d). In this case, only the outer interface appears visible. After evaluating the time delay by OMP, we simulate new received signals using a 3MHz Gaussian pulse: new received signals and resulting TDTE image are shown on Figs. 4.10(b) and 4.10(e), respectively. Here we clearly see that both the outer and inner interfaces are visible. The inner interface is not at the correct location due to the velocity mismatch between water and sawbone. We finally apply the correction ratio σ , and the obtained results are shown on Figs. 4.10(c) and 4.10(f). Now both interfaces are reconstructed correctly.

These figures illustrate the necessity of using OMP before the application of the TDTE process in the case of strong overlap between the echoes coming from the outer and inner interfaces. OMP allows to evaluate the time delays, and then to simulate new received signals at higher frequency. This alternative to the standard TDTE process allows to reconstruct the image of a thin interface (thickness less than or similar to one wavelength). Finally figures 4.10(c) and 4.10(f) illustrate again the necessity of the correction ratio, that evaluates the propagation velocity mismatch between the back-propagation (done in water) and real experiment (in the sawbone material, the ultrasonic wave propagates with a higher velocity).

The 6 series of measurements are processed using the same procedure, and the 6 resulting TDTE images are assembled together to form the global image shown on Fig. 4.11. One key point here is the correct evaluation of the time delays by OMP, and the application of the correction ratio to take into account the velocity mismatch. If this estimation is not correct, the TDTE result will be very sensitive to the wrong time delays. This figure proves that OMP is a performant add-on to standard TDTE that significantly enhances the capacity of TDTE imaging.

In this chapter, the OMP method shows efficient performance to solve the mismatch and weak of internal boundary in TDTE imaging. This strategy can keep the efficient of TDTE when there is analytical solution for the reference medium, and it can deal with normal discontinue boundary structure, such as the portion in front of transducer array located in 270 degree. However, this strategy is limited when the discontinuity of boundary structure is high, such as the portion in front of transducer array located in 0 degree, and also porous structure inside the cortical bone. Under such circumstance, the second iteration of TDTE is required, which will introduce in next chapter.

4.5 Appendix

As mentioned above, formula (4.2) is based on an approximation in the case of overlapping between echoes. The envelop of a temporal signal $\mathbf{y}(t)$ is obtained by computation of its Hilbert transform. In the particular case of a Gaussian pulse $\mathbf{g}(t)$ given by

$$\mathbf{g}(t) = e^{-s(t-\tau)^2} \cos[2\pi f(t-\tau) + \phi] \quad (4.10)$$

its Hilbert transform $\mathbf{g}_h(t)$ is

$$\mathbf{g}_h(t) = e^{-s(t-\tau)^2} \sin[2\pi f(t-\tau) + \phi] \quad (4.11)$$

such that the envelop of $\mathbf{g}(t)$ is

$$\tilde{\mathbf{g}}(t) = \sqrt{\mathbf{g}(t)^2 + \mathbf{g}_h(t)^2} = e^{-s(t-\tau)^2} \quad (4.12)$$

The envelop of the received signal (4.2) with $K = 2$ and in the absence of noise can be written as

$$\begin{aligned} \tilde{\mathbf{y}}(t) = & \sqrt{e^{-2s_1(t-\tau_1)^2} + e^{-2s_2(t-\tau_2)^2} + 2e^{-s_1(t-\tau_1)^2} \dots} \\ & \dots \sqrt{e^{-s_2(t-\tau_2)^2} \cos[2\pi(f_2\tau_2 - f_1\tau_1)]} \end{aligned} \quad (4.13)$$

When the $\cos[2\pi(f_2\tau_2 - f_1\tau_1)] \approx 1$, which means the time delay the previous expression simplifies and we obtain

$$\begin{aligned} \tilde{\mathbf{y}}(t) & \approx \sqrt{e^{-2s_1(t-\tau_1)^2} + e^{-2s_2(t-\tau_2)^2} + 2e^{-s_1(t-\tau_1)^2} e^{-s_2(t-\tau_2)^2}} \\ & \approx e^{-s_1(t-\tau_1)^2} + e^{-s_2(t-\tau_2)^2} \\ & \approx \tilde{\mathbf{g}}_1(t) + \tilde{\mathbf{g}}_2(t) \end{aligned} \quad (4.14)$$

To understand this approximation better, we give an illustration when the two echoes with and without overlapping. Fig. ?? and ?? illustrate the two echoes are without overlapping, the sum of envelop of each echo is equal to the envelop of the whole signal. When the echoes are overlapping shown in Fig. ??, there is mismatch between the two kinds of envelop, which is why we use approximation in Eq. 4.2. However, it can be observed that the mismatch don't influence the time delays basically. It means that the envelop of the received signal, written as the sum of two Gaussian pulses, can be approximated by the sum of the envelopes of each pulse. This justifies that the initial OMP, written on the temporal signals,

can be derived as an alternate and simplified version of OMP working on envelopes only.

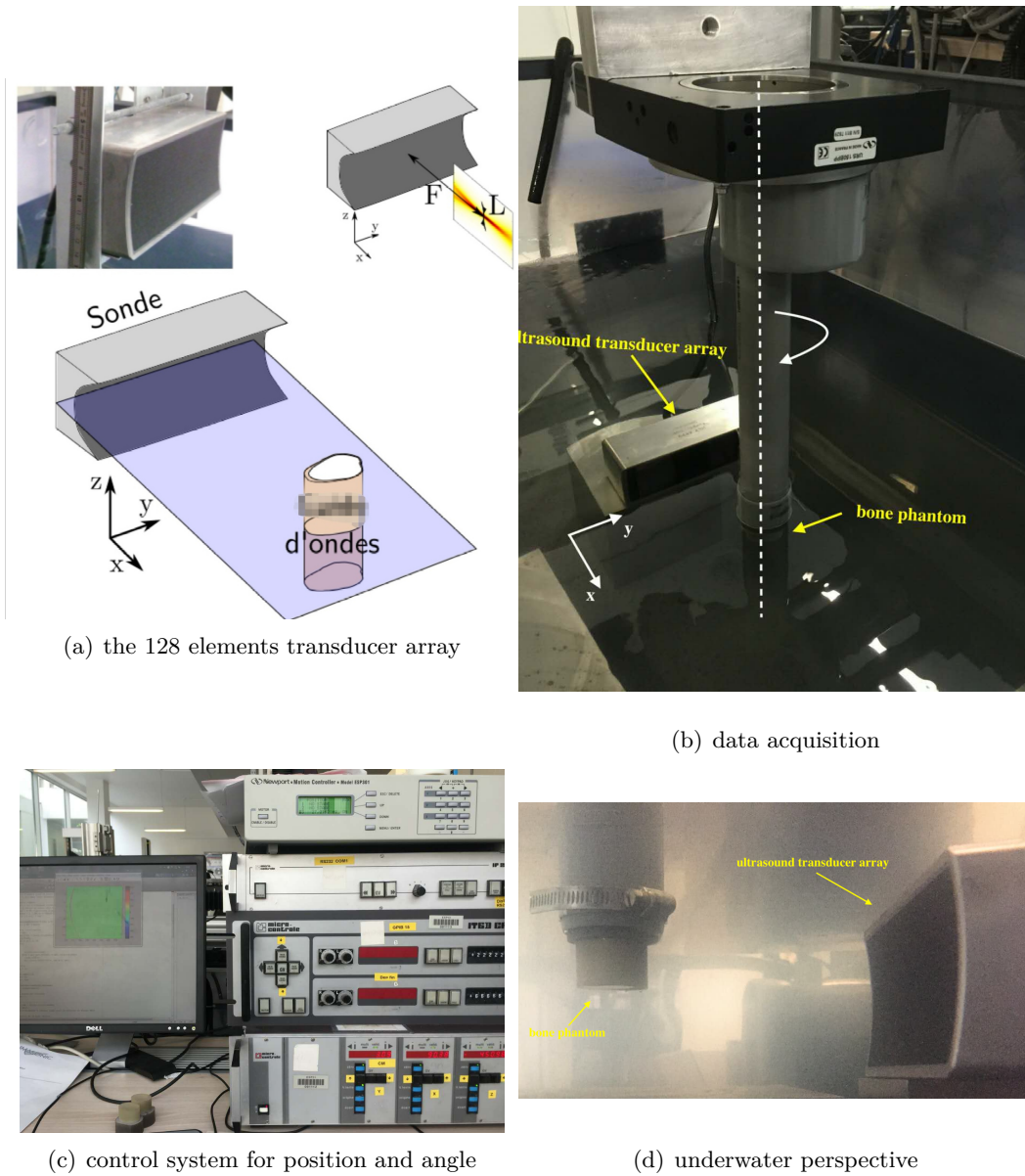


Figure 4.9: Experimental setup

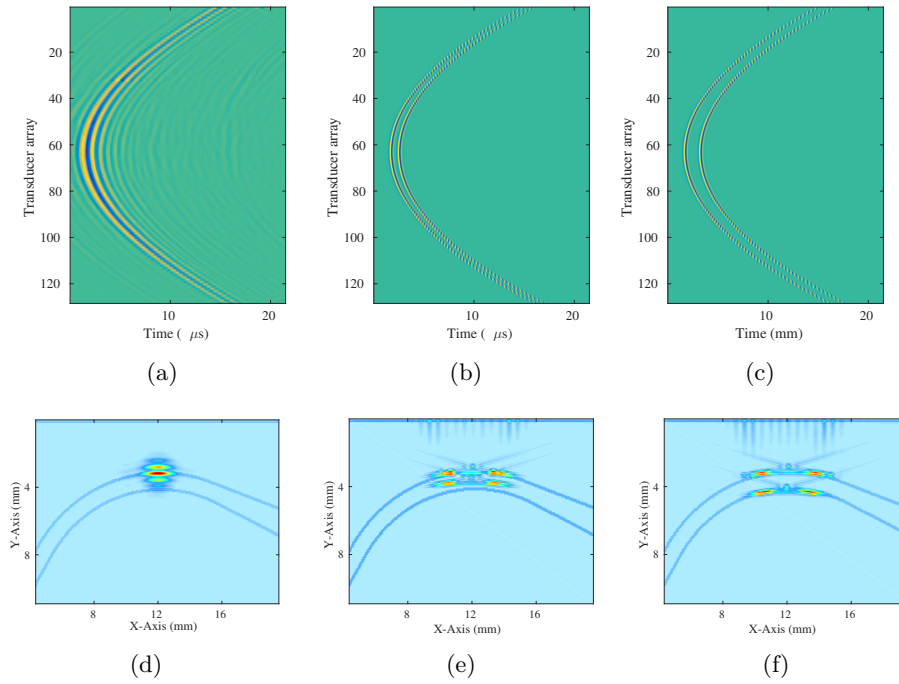


Figure 4.10: TDTE at 0 degree: (a) received signals without any processing, (b) reconstructed signal by OMP and increase of the frequency, (c) corrected time delays for the echoes from the inner boundary, (d-f) corresponding TDTE images.

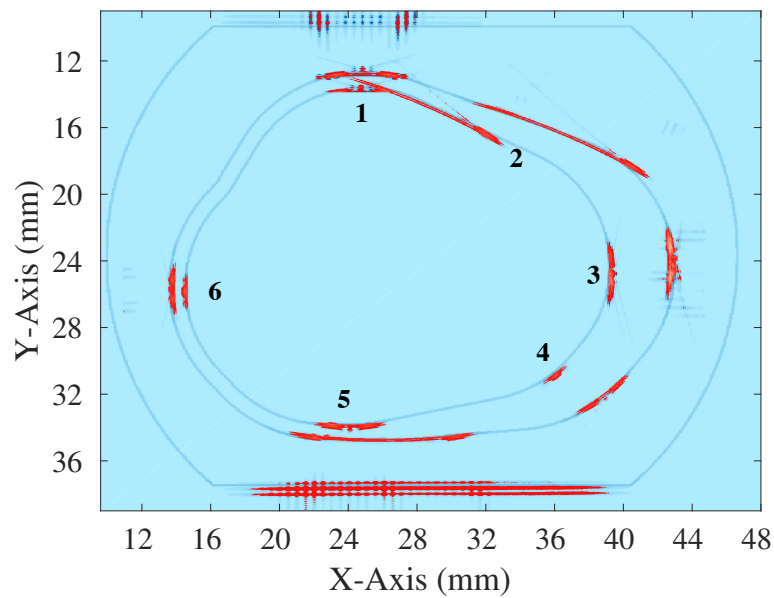


Figure 4.11: reconstructed image by TDTE and OMP, blue lines represent the contours of the bone phantom

CHAPTER 5

Iterative TDTE applied to cortical bone imaging

It has been illustrated in Chapter 3 that the principle of TDTE is to find the differences between a reference medium and the real inspected medium. Practically, this means that the reference medium should be chosen as close as possible to the real medium. For cortical bone imaging, the biggest challenge is that the inner structure of the bone (including the irregular boundary and porous structure) is difficult to obtain. If the reference medium is set to be homogeneous fluid, as done in Chapter 3, the displacement fields for both forward and adjoint problems can be approximated by an analytic formulation, based on the assumption that the elements of the array are small enough. Consequently, the cost in terms of computation time and memory storage is reasonable.

For cortical bone imaging, the first iteration of TDTE is enough to achieve the external boundary. The acoustical signature generated by the interior structure of the bone (including the inner boundary) is weak, mainly due to i) the attenuation in bone and ii) the strong contrast of acoustic impedance between soft tissues and bone. According to the principle of TDTE, if the external boundary information is used to construct the reference medium, the difference between the reference medium and inspected medium will focus on the interior structure.

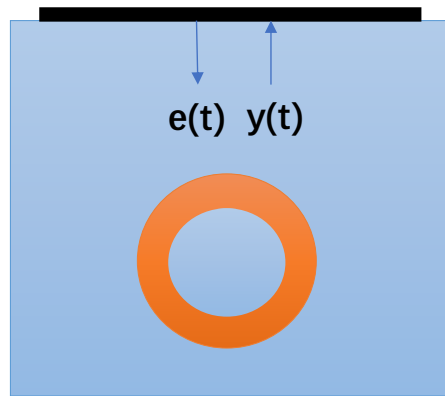
The main difficulty of iterative TDTE is that the homogeneous fluid reference medium cannot be used in the second iteration. It is therefore no more possible to take advantage of analytic solutions, and the problem must be treated purely numerically, for the forward as well as the adjoint problems. The immediate consequence is the computation time and storage requirements that increase significantly.

5.1 Iterative TDTE

To enhance the interior structure of the cortical shell, we have introduced sparse signal processing applied to the received signals before TDTE integration. This strategy can avoid iterative TDTE but can be applied only for a regular internal boundary. In a real bone, the internal boundary is generally not so regular, and

also with some porous structure. For this reason, and also due to the porosity of the cortical shell, the performance of sparse signal processing is limited as we cannot find a well-identified echo from a straightforward interface. In this case, iterative TDTE appears as the only feasible alternative, despite its cost in terms of computation time and memory storage.

Iterative TDTE is based on the same general principles as standard TDTE, just adapting the reference medium used in the back-propagation step from the image obtained at the previous iteration. As a consequence, the general scheme can be summarized as follows. Here we give an illustration of iterative TDTE imaging of cortical bone, which is represented by a tube in Figure 5.1. With an plane wave excitation $\mathbf{e}(t)$ to the inspected medium, the received signal denotes $\mathbf{y}(t)$.



(a)

Figure 5.1: the numerical setup for TDTE cortical bone imaging

- the first iteration uses a homogeneous fluid as reference medium: this first step allows to clearly identify the external boundary of the cortical bone, and can be performed numerically in an efficient way, using analytic solutions. The procedure is shown in Fig. 5.2(a), the external boundary is represented by bold orange circle, and internal boundary is weak and in a mismatch position, represented by dash orange circle.
- once the external boundary has been identified, we can imagine a modified reference medium made of two layers: 1) a homogeneous fluid between the transducer array and the previously obtained external boundary of the bone, and 2) a homogeneous elastic medium inside the external boundary of the

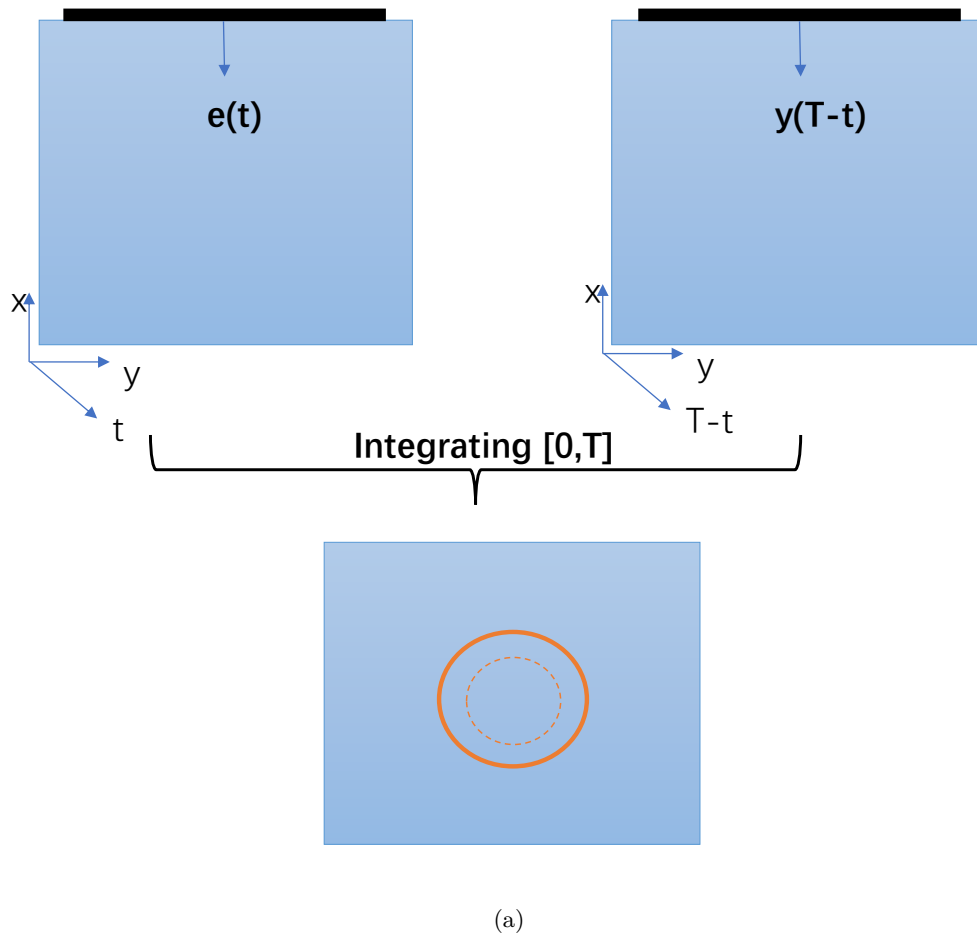


Figure 5.2: the scheme of first iterative TDTE

bone. With the same excitation $e(t)$ to the reference domain, the received signal is $y_1(t)$, illustrated in Fig. 5.3.

- the second iteration of TDTE will then exhibit the differences between this new reference medium and the real inspected medium, denoted $\mathbf{y}(t) - \mathbf{y}_1(t)$, making visible the effects of the internal boundary, represented by bold orange circle in Fig. 5.3, and porosity inside the cortical shell.

It is important to note that the modified reference medium implies the *a priori* knowledge of the elastic properties of the bone. For that purpose, we can use data that have been measured experimentally and published in literature. As mentioned earlier, one inconvenient is the large increase of the computation time and storage requirements, since the forward and adjoint fields need to be recorded in time and space for the TDTE integration. In chapter3, we also illustrated the wave field

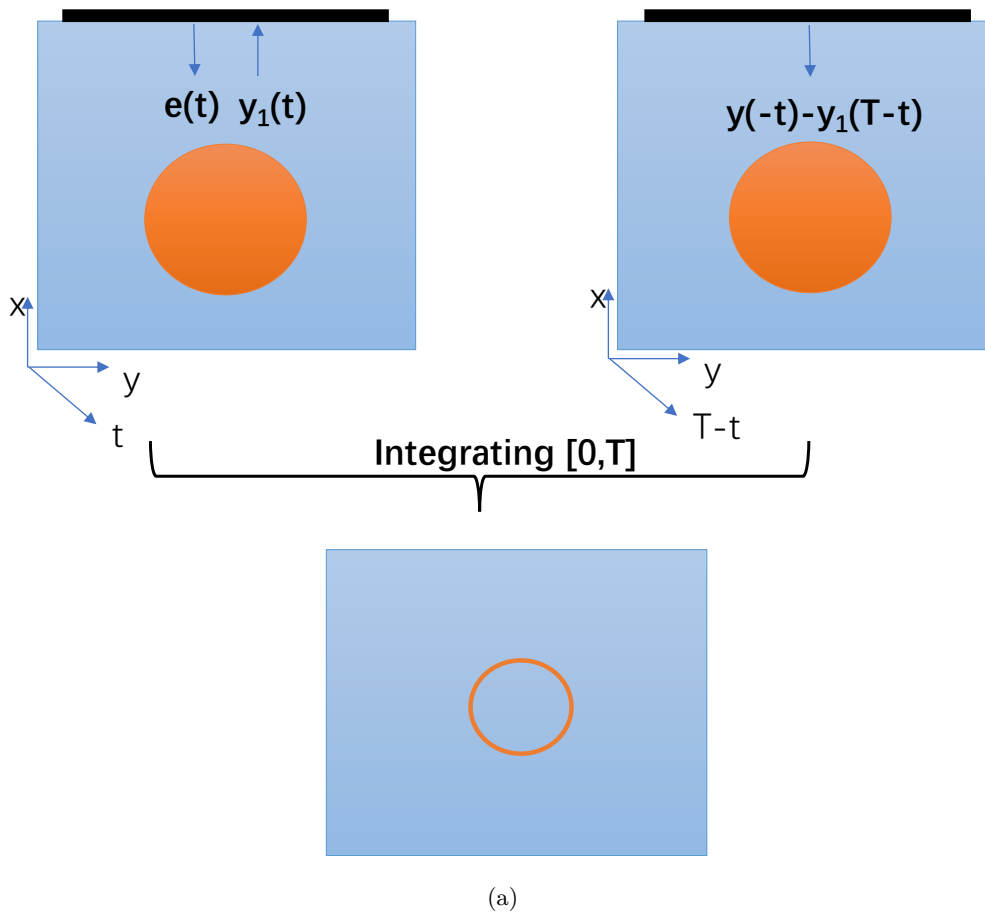


Figure 5.3: the second iteration of TDTE, reference medium is modified according to the result from first iteration

sampling frequency in time can be decreased in 30 times, and the integration time interval also can be reduced, these can also decrease the storage significantly.

5.2 Numerical simulation

5.2.1 Cortical bone with irregular internal boundary

In the previous chapter, it can be observed in Fig. 4.6(b) that, for a transducer array located at 0 degree (where the internal interface of cortical bone is quite irregular, the corresponding numerical setup is shown in Fig.5.4(a)), OMP cannot distinguish the echoes from the internal interface. In such circumstance, the internal boundary can't be obtained by first iteration of TDTE. In this condition, we will try to use second iteration of TDTE to obtain the internal boundary of corti-

cal bone for irregular boundary case. For the first iteration TDTE, the reference medium is homogeneous water shown in Chapter 3. For the second iteration TDTE, the reference medium is improved by considering the material inside the external boundary as bone material, shown on 5.4(b). The parameters of bone material in inspected cortical bone and reference medium of second iteration are both defined as the same with the previous chapter, illustrated in Table. 3.3.

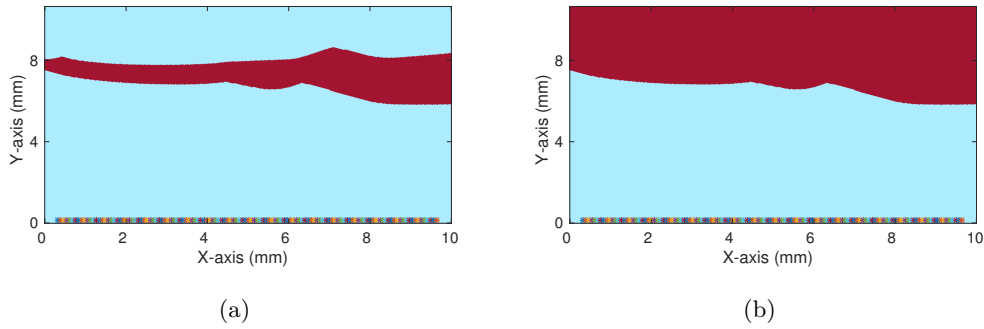


Figure 5.4: (a) numerical setup, the red area represents the bone material, (b) reference medium used for the second iteration of TDTE

For the inspected cortical bone (Fig. 5.4(a)), the corresponding received signal is shown in Fig. 5.5(a):left. And for the reference medium (Fig. 5.4(b)), the corresponding received signal is shown in Fig.5.5(a):middle. To perform the second iteration of TDTE in the adjoint domain, the adjoint source was calculated by the difference between the received signals (Fig. 5.5(a):left) from the inspected medium and the received signals from the reference medium (Fig. 5.5(b): middle). This difference, shown in Fig. 5.5(a):right, is used as new transmission for the adjoint problem in second iteration of TDTE. If we compare the different figures in Fig. 5.5(a), we can observe that

- the received signals from inspected cortical bone (Fig. 5.5(a):left) mix multiple information from the external and internal boundaries of the sample used in the simulation,
- the received signals from reference medium (Fig. 5.5(a):middle) principally contain information from the external interface only,
- their difference (Fig. 5.5(a):right) naturally enhances the effects of the internal boundary, since the effects of the external boundary, that are dominating the the full B-scan, have been removed by calculating the difference.

To see more clearly how the iterative TDTE enhance the internal boundary of cortical bone, we also give their waveform from one transducer, which is No.110 in

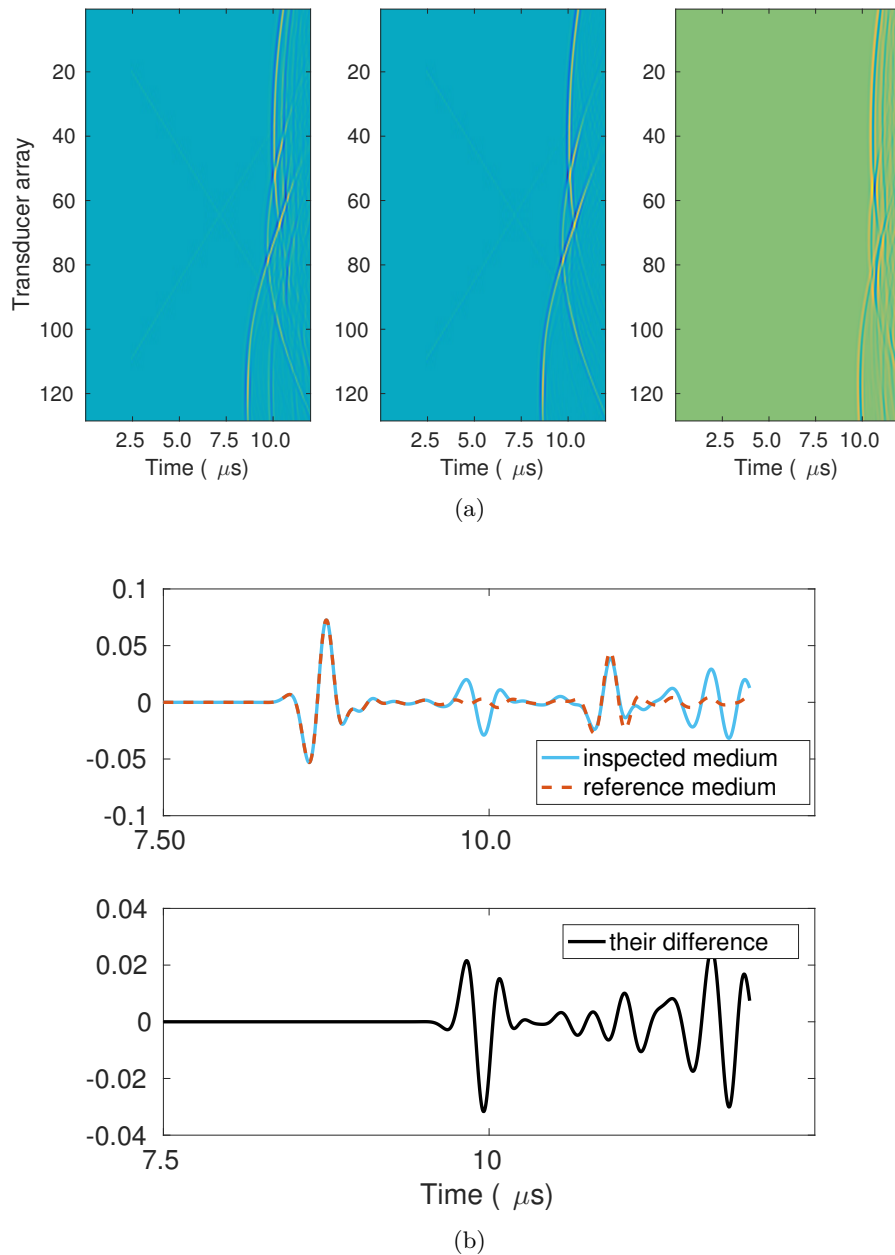


Figure 5.5: (a) left:received signals from inspected medium, middle: received signals from reference medium, right: their difference. (b) up: the signal from inspected medium and reference medium from one transducer (No.110), down: their difference

this 128 transducer array. It can be observed in Fig. 5.5(b) that the signal from both medium have the same first echo, which corresponding to external boundary. Their difference is enhanced naturally the second echo from internal boundary of inspected medium. This is the reason why the iterative TDTE can help us to

obtain some additional information about the internal structure of the cortical shell.

SimSonic2D is used here to calculate the displacement fields in both forward and adjoint domains, both domain are occurred in reference medium shown in Fig. 5.4(b). For forward problem, the excitation is same with original excitation $\mathbf{e}(t)$, the received signal $\mathbf{y}_1(t)$ and displacement fields $\mathbf{u}(\mathbf{x}, t)$ are recorded by SimSonic2D. For adjoint problem, the transmitted signal it the time difference of $\mathbf{y}(t) - \mathbf{y}_1(t)$, which is shown in Fig. 5.5(c), and the displacement fields $\mathbf{u}^\dagger(\mathbf{x}, t)$ are recored. Then, the two displacement fields $\mathbf{u}^\dagger(\mathbf{x}, t)$ and $\mathbf{u}(\mathbf{x}, t)$ are integrated over time, with a time duration T , which is length of received signal $[0, 12.5] \mu$ s.

$$K_{TE}(\mathbf{x}) = \int_0^T \|\mathbf{u}^\dagger(\mathbf{x}, T - t)\|^2 \|\mathbf{u}(\mathbf{x}, t)\|^2 dt \quad (5.1)$$

The reconstructed image in second iteration of TDTE and its overlapping with original image are shown in Fig. 5.6. From this figure, we observe that the reconstructed image matches the original map. Since the bone material in second reference medium is same with the inspected bone, which means the speed of wave is transmission in the bone is same with inspected medium, no more mismatch of internal boundary occurred in first iteration of TDTE.

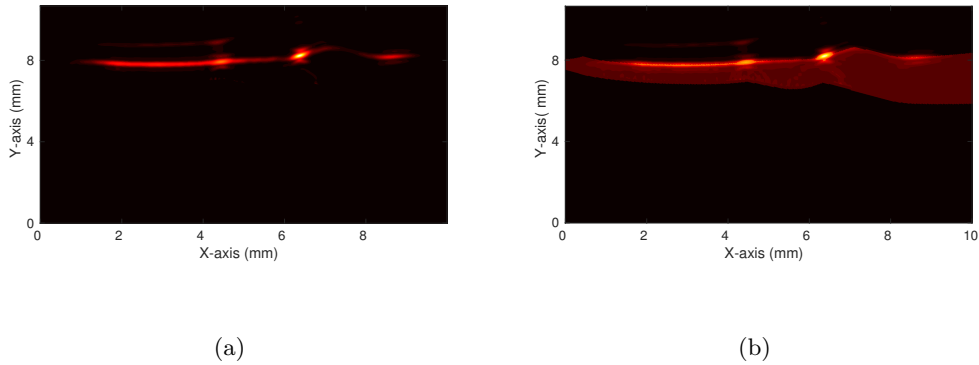


Figure 5.6: reconstructed image from the second iterations of TDTE and its overlapping with original inspected cortical bone

Finally, the reconstructed images from first and second iterations of TDTE are assembled together and the result is shown on Fig. 5.7, illustrating that we can successfully obtain an accurate map of the initial sample.

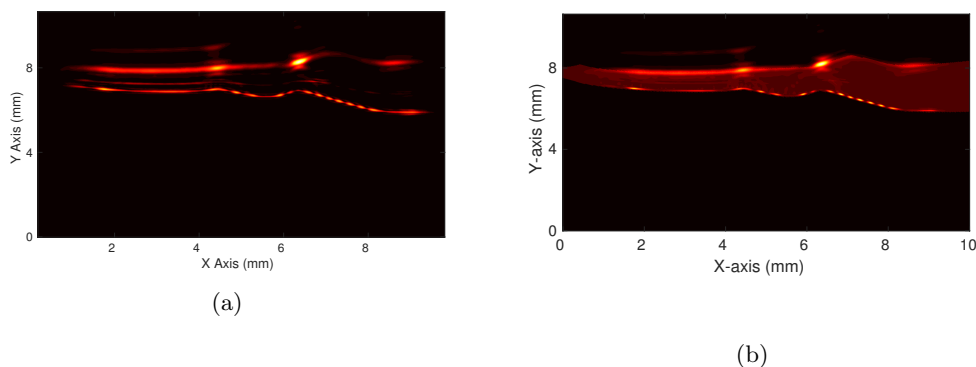


Figure 5.7: the reconstructed image by 2 iterations of TDTE and its overlapping with original image of cortical bone

5.3 bone phantom validation

For the bone phantom used in previously chapter, there is only one portion with irregular boundary, which is shown in Fig. 5.8, denoted by red dash rectangular. In this part, the thickness of sawbone is 1 mm, the structure in this part contains two different curvature. The sawbone was placed in a water tank, and the ultrasound probe was immersed in water for signal acquisition. The probe was place along the red bold line, which the cross-section view is illustrated in Fig. 5.8, in order to produce an image in the cross-section view of the irregular portion. The inter-element pulse-echo signals were recorded using a fully programmable ultrasound system (Vantage 64LE, Verasonics Inc., Redmonnd, WA, USA) equipped with a 5.2 MHz linear array transducer (L7-4 ATL, Bothell, WA, USA; pitch 0.298 mm, 128 elements).

In the first iteration of TDTE, the reference medium is homogeneous water. Since the measurement is real experiment, an initial simulation domain including the size and position of transducer array should be defined for the TDTE. The pitch of each element of transducer array should be defined as the reality (0.298mm). Then the TDTE imaging can be obtain by analytic solution introduce in Chapter 3, the result is show in Fig. 5.9(a), where it can be observed that external boundary of cortical bone are clear visible. Since the thickness of cortical bone phantom in this part is 1 mm, the internal boundary is still visible, but with a mismatch position caused by the velocity mismatch we discussed above. Its B-scan image is shown in Fig. 5.9(b), where can be observed that the resolution is less than TDTE

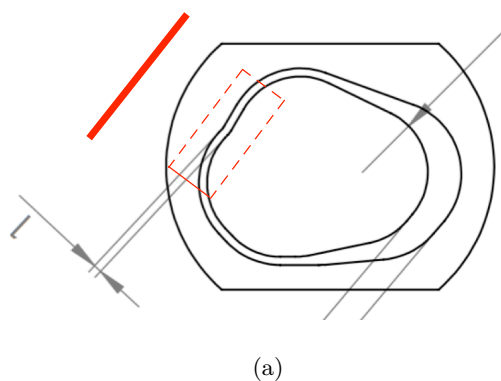


Figure 5.8: the cross-section view of experimental setup for measuring the bone phantom, where the red bold line represents the ultrasound transducer array

image.

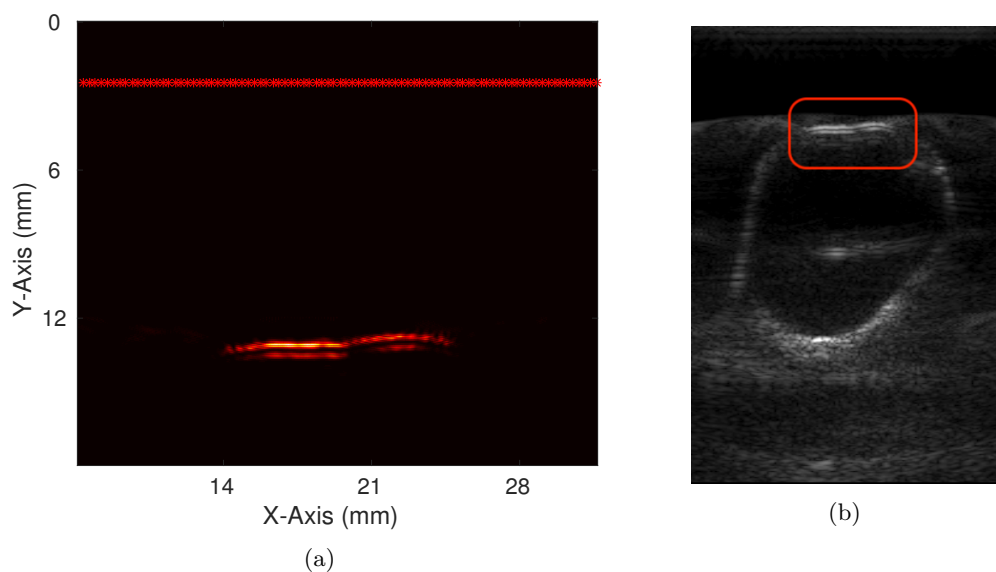
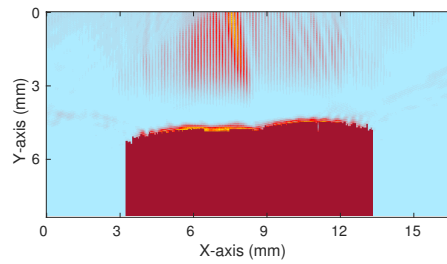


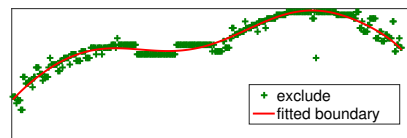
Figure 5.9: (a) the TDTE image by first iteration, where the red stars represent the transducer array (b) B-scan image

To build the reference medium for second iteration, the external boundary of TDTE image need to be extracted. By choosing the highest value of pixel in each column of TDTE image, we can located the external boundary with some turbulence, shown in Fig. 5.10(a). After processing by high order curve fitting, the external boundary are more smooth, which is used in the second iteration shown in Fig. 5.10(b), where the red pixels represent bone phantom material, while blue

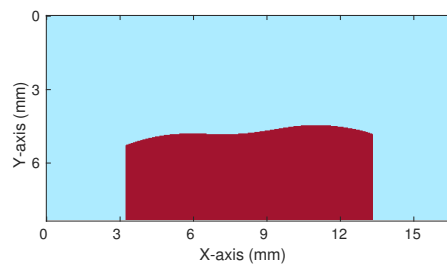
pixels represent water, where the parameters are illustrated in Table 4.4 (Chapter 4).



(a)



(b)



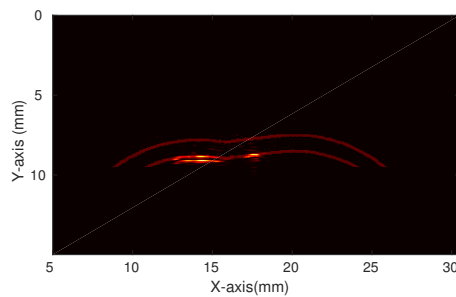
(c)

Figure 5.10: (a) the external boundary extracted from TDTE image, (b) curve fitting of the extracted point from (a), (c) reference medium used for the second iteration

Then the second iteration of TDTE is performed on the new reference medium as follows,

- Firstly, the forward simulation is excited by the same Gaussian pulse with real experimental measurement, the corresponding received signal and displacement of wavefield are recorded.

- Secondly, calculating the adjoint source: the adjoint source is obtained by the time difference between the real received signals and signals from forward simulation.
- Thirdly, running the adjoint simulation, which is also performed by Simsonic2D, the displacement of wavefield are recorded.
- Integration: integrating the two displacement wavefields on time, the TDTE image and its overlapping on the original structure of bone phantom are shown in Fig. 5.11, we can observe that the internal boundary is successfully obtained in right position.



(a)

Figure 5.11: the TDTE image in second iteration and its overlapping with original bone phantom

5.4 Iterative TDTE of cortical bone with osteoporosis (pores inside cortical bone)

In the previous section, we have shown that iterative TDTE is able to reconstruct the irregular internal boundary of the cortical shell. However, the cortical shell may also contain small pores that are involved in the mechanical characteristics of the bone. Once again it is important to evaluate the structure and dimensions of this porosity, especially, one mainly repression of osteoporosis is the porosity increasing of cortical bone. To imaging the pores in cortical bone will be important to evaluate the cortical bone, and iterative TDTE may help for that particular purpose.

A portion of osteoporosis cortical bone with several pores is shown on Figure 5.12(a). This image is used to build a numerical map with two kind of materials usable in SimSonic2D: the yellow pixels represent bone material, while blue pixels represent water. A transducer array of 128 elements (array pitch 1.5mm) is placed on the top of the map shown on Fig.5.12(b). The transmitted signal is a Gaussian pulse of central frequency 3.5MHz and bandwidth 1MHz.

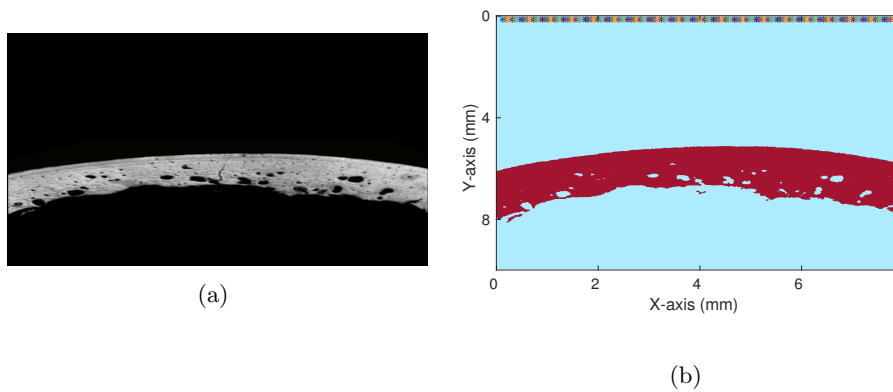
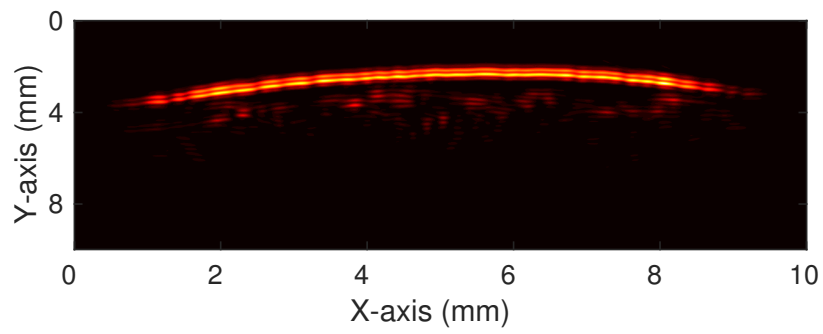


Figure 5.12: (a) CT image of a cross-section of cortical bone, (b) numerical configuration

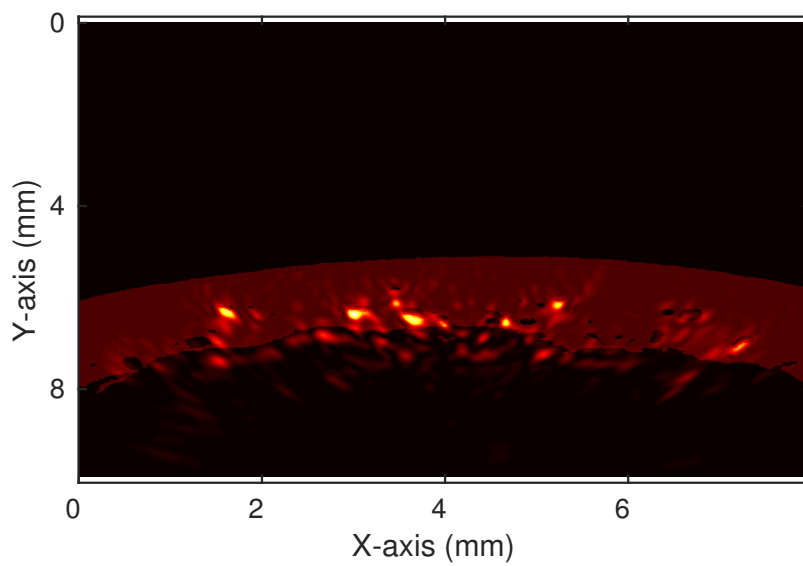
The first iteration of TDTE is performed by the reference medium, which is homogeneous water. The TDTE image is shown on Fig. 5.13(a), where the external boundary is obtained, and the pores is shown in low contrast and mismatched, caused by the high contrast between cortical bone and surrounding medium, and also velocity mismatch as we discussed above.

For the second iteration of TDTE, we replace the medium below the external boundary by bone material to build a new reference medium. The resulting image is shown on Fig. 5.13(b), where the biggest pores are effectively identified. We can also observe that the central part of the reconstructed image has a larger intensity than the left and right sides: this is due to the fact that i) the central part is closer to the transducer array and ii) the shape of the external boundary appears parallel to the array, therefore resulting in less losses of reflected and refracted components due to geometrical effects.

In order to compensate this geometrical effect, we can rotate the transducer array and run iterative TDTE separately. The transducer array is placed in three different angles, which one is in the central front of the cortical bone, the other



(a)



(b)

Figure 5.13: (a) first iteration of TDTE, (b) second iteration of TDTE

two angles are rotated 5 degrees in clockwise and counter-clockwise separately. The three configurations are shown in left column of Fig. 5.14, and the corresponding second iteration TDTE image are shown in the right column of Fig. 5.14. It can be observed that the left, central and right parts are effectively enhanced independently.

The last three TDTE images, resulting from 3 different angles of the transducer array with respect to the simulated sample, can finally be assembled together to produce the final image shown on Fig. 5.15, that now contains more details than the image on Fig. 5.13.

Furthermore, it can be observed some tails behind the reconstructed pores in Fig. 5.13, which are not the real defects in cortical bone. Especially more seriously below the internal boundary of cortical bone. In Fig. 5.15, the tails of the reconstructed pores are improved significantly, there is no visible fake shadows below the internal boundary of cortical bone. And the pores are reconstructed with more clear boundary. The principle is very similar with CT scanner. For one angle projection, there will exist shadow behind the defects. By assembling several projections from different angles, the contrast between the real defects and fake shadow will be increased, the shadow will become invisible. This numerical simulation indicates us in two aspects: (a) the second iterative TDTE has a good potential in imaging the pores and defects, which is important in evaluate the osteoporosis. (b) the TDTE imaging combined with computed tomography configurations provides better performance, increase the resolution of pores.

In the above simulation, it can be observed that the smallest reconstructed pores with a diameter of 0.16mm, and the central frequency of excitation is 3.5 MHz, which the corresponding ratio of diameter/wavelength is 0.14.

Normally, the saying of porosity is referring the diameter from 0.05 to 0.2 mm. To validate the performance of second iterative TDTE in osteoporosis cortical bone, a CT image from a femur neck cortical bone with osteoporosis is shown in Fig. 5.16. The zoom out area is set to be the simulation area.

By taking consideration of the above resolution (ratio of diameter/wavelength is 0.14), we set our excitation to be 10 MHz Gaussian pulse. the simulation setup is same with above. The reconstruction of second iterative TDTE overlapping with its original map is shown in Fig. 5.17, where some diameter of Pores equaling to 0.05 mm can be reconstructed. The corresponding ratio of diameter/wavelength is 0.13. It can be also observed that it is sensitive with perpendicular narrow crack,

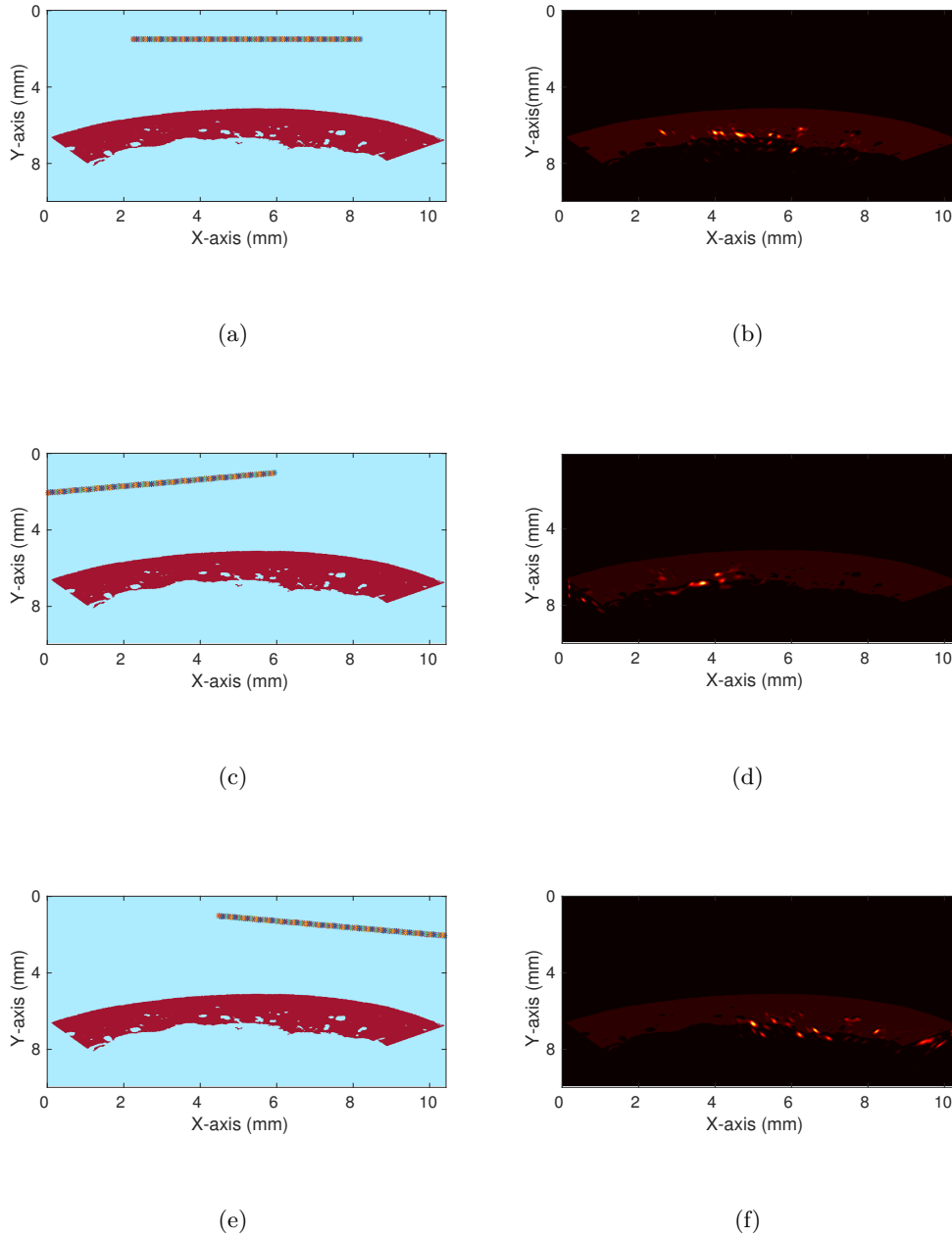


Figure 5.14: Left: numerical configuration, Right: corresponding TDTE image from the second iteration

and the reconstruction precision decreases with depth. Overall, the second iterative TDTE shows significant promising result in osteoporosis cortical bone imaging by high frequency ultrasound.

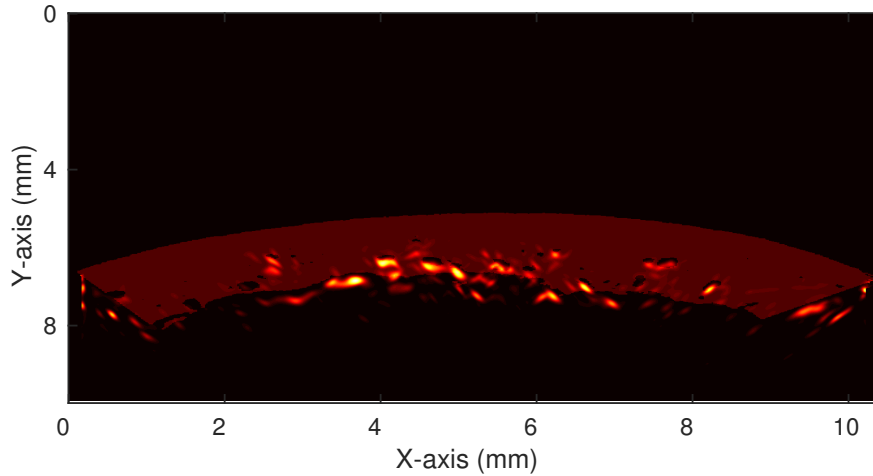


Figure 5.15: the summation of three TDTE images, from three different angles

In this chapter, we introduce the second strategy to enhance the performance of TDTE imaging. Although losing sort of efficiency compared to sparse signal processing, the benefit of second iterative TDTE, which is in dealing with irregular inner boundary and porous structure cortical bone, is irreplaceable. The increasing of storage caused by the second iterative TDTE can be acceptable, and more important, it shows promising result in small pores (0.05mm) in osteoporosis cortical bone, which is a significant improvement in ultrasound cortical bone imaging.

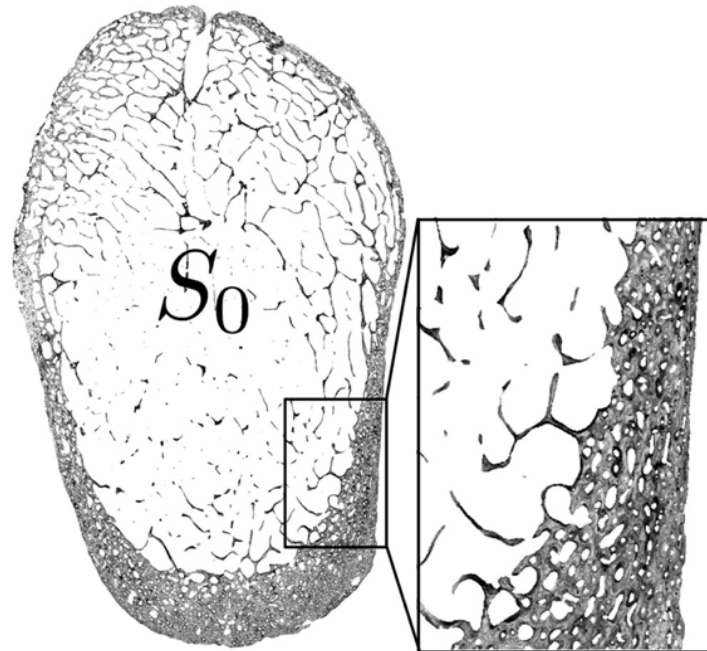


Figure 5.16: CT image from a femur neck cortical bone with osteoporosis

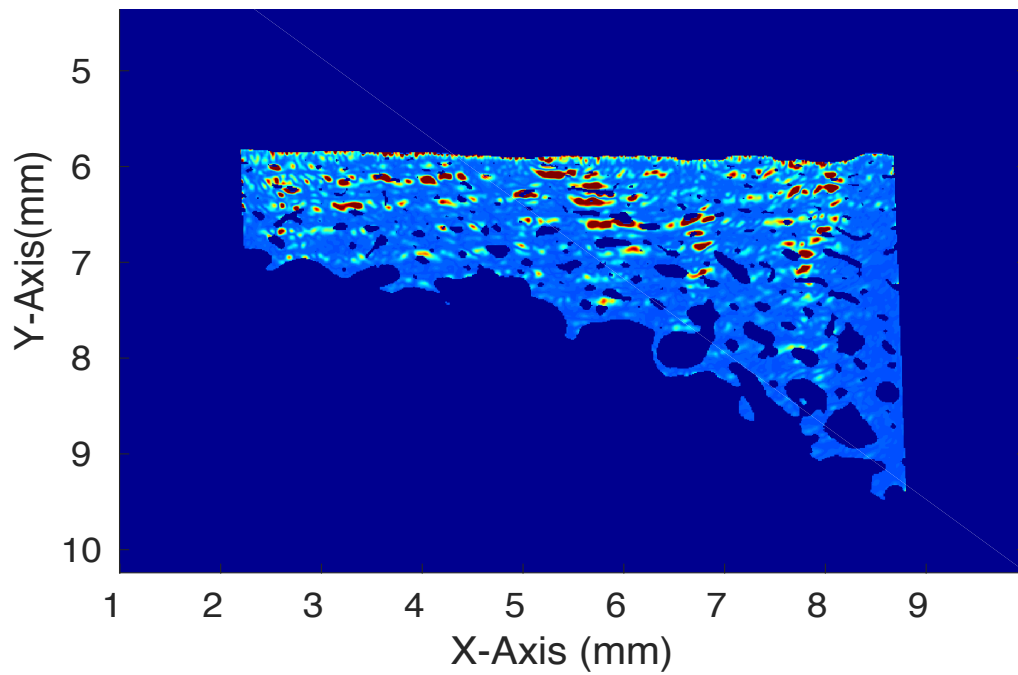


Figure 5.17: the second iterative TDTE image of osteoporosis femur neck

CHAPTER 6

Quantitative Imaging of Cortical Bone by Full Waveform Inversion

In geophysics community, the seismic migration as well as Full Waveform Inversion (FWI) has played a central role in constructing the subsurface images and multi-parameters of Earth's interior currently (Luo et al., 2009; Virieux and Operto, 2009). They are based on optimizing a misfit function between the observed data and synthetic data using gradient-based algorithm, which can be calculated via the adjoint method both in time (Tromp et al. 2004 (Tromp et al., 2004); Liu et al. 2006 (Liu and Tromp, 2006)) and frequency (Plessix, 2006; Pratt et al., 1998) domains, resulting with "sensitivity kernels" respect to density, shear modulus and bulk modulus. The calculation of kernels involves the time-integrated interaction between the current forward wavefield and an adjoint wavefield generated synthetically. However, not until recently has FWI brought insightful results, the significant acceleration provided by parallel processing with graphics processing units (GPUs) has allowed a considerable reduction in execution times. Recently, FWI methods have also started to be applied in medical ultrasound imaging, particularly focus on the breast tomography, see e.g. (Sandhu et al., 2015a,b), Wang et al 2015 (Wang et al., 2015) and Perez-Liva et al 2017 (Pérez-Liva et al., 2017) and references therein, as well as shear wave elastography ((Arnal et al., 2013)). (Bernard et al., 2017) has applied FWI for quantitative cortical bone imaging in 2D numerical simulation. The high time consuming and storage requirements are the main obstacles of Full Waveform Inversion applying in medical imaging. The time domain topological gradient (TDTG) share the main principle of FWI, which is to minimize the misfit waveform between the inspected medium and reference medium, but it is derived from the mathematical community of shape optimization.

FWI is an established tool for building high resolution velocity model of earth interior. Seismic migration, which attempts to map reflected and/or refracted signals to their actual spatial origin, plays a central role in imaging. Migration techniques are frequently based upon approximations to the seismic wave equation. (Tarantola, 1984) demonstrates that the seismic inverse problem may be solved iteratively by numerically calculating the gradient of a waveform misfit function with respect to a set of model parameters. This gradient may be constructed from the interaction between 1) the wavefield resulting from the current model and 2)

a wavefield obtained by time-reversal of the difference between the experimental data and the temporal signals at all receivers, once again resulting from the current model. This processing requires two numerical simulations per iteration: one for the current model and the second one for the time-reversed differences between experimental and simulated data ((Luo et al., 2009; Zhu et al., 2009)). It is also widely known that the gradient of the previous misfit function can be solved using the adjoint method ((Plessix, 2006; Tromp et al., 2004)), which has been also applied to Full waveform inversion ((Virieux and Operto, 2009)). (Mendel, 1983) and (Tarantola, 1984) have shown that the gradient of a least-squares waveform misfit function is equivalent to the images resulting from seismic migration. (Mora, 1987) has developed a numerical implementation of these ideas for nonlinear inversion of multioffset seismic reflection data. In addition, an iterative waveform minimization procedure in the frequency domain has been developed by (Pratt et al., 1998).

Migration has played a central role in constructing subsurface images by projecting reflections recorded at the surface back to their origins. Although various migration techniques have been consistent with Claerbouts generic definition, the imaging principle has also been related to the gradient of a waveform misfit functional in the context of an optimization problem, in which we seek to determine a model that minimizes a misfit function ((Luo et al., 2009; Zhu et al., 2009)). Migration can then be treated as a partial inversion or the initial step of an iterative inversion. It is widely known that the gradient of such a misfit function may be calculated via the adjoint method ((COURTIER and TALAGRAND, 1987; Plessix, 2006; Tarantola, 1984; Tromp et al., 2004)), which has been applied to full waveform inversion in exploration seismology as well as in regional tomography. For easier understanding, we will introduce migration first and Full Waveform Inversion after.

6.1 Migration by adjoint method

As above discussion, the migration can be started from waveform inversion problem, as the partial of it. According to (Tarantola, 1984) and (Tromp et al., 2004), a least-squares waveform misfit function is used to solve the inversion by quantifying the fit between experimental and simulated data. The experimental data is the reception from a phased array with N independent elements and their emission.

The waveform misfit function χ is defined as

$$\chi = \frac{1}{2} \sum_r \int_0^T [\mathbf{s}(\mathbf{x}_r, t) - \mathbf{d}(\mathbf{x}_r, t)]^2 dt \quad (6.1)$$

where r corresponds to a particular receiver of the array, $[0, T]$ denotes the time interval of interest, $\mathbf{d}(\mathbf{x}_r, t)$ the series of experimental measurements (temporal signals measured by each receiver), and $\mathbf{s}(\mathbf{x}_r, t)$ the simulated received signals. The vector \mathbf{x}_r corresponds to the spatial position of the receivers. For simplification, we will use \mathbf{d} and \mathbf{s} to denote experimental and synthetic data, omitting the explicit dependence with \mathbf{x}_r and t .

(Tromp et al., 2004) has discussed the minimization of the misfit function using the adjoint formulation, we give a brief introduction of the adjoint method here. Minimizing the misfit function must satisfy the constraint that the synthetic displacement \mathbf{s} satisfies the wave equation. Mathematically, this implies the PDE-constrained minimization of the action

$$\chi = \frac{1}{2} \sum_r \int_0^T [\mathbf{s}(\mathbf{x}_r, t) - \mathbf{d}(\mathbf{x}_r, t)]^2 - \int_0^T \int_{\Omega} \lambda (\rho \partial_t^2 \mathbf{s} - \nabla \cdot \mathbf{T} - \mathbf{f}) d^2 \mathbf{x} dt \quad (6.2)$$

Where the vector λ remains to be determined. Taking the variation of the Eq. 6.2, through integrating terms involving spatial and temporal derivations, we will obtain

$$\begin{aligned} \delta \chi = & \int_0^T \int_{\Omega} \sum_r [\mathbf{s}(\mathbf{x}_r, t) - \mathbf{d}(\mathbf{x}_r, t)] \delta(\mathbf{x} - \mathbf{x}_r) d^2 \mathbf{x} dt \\ & - \int_0^T \int_{\Omega} (\delta \rho \lambda \cdot \partial_t^2 \mathbf{s} + \nabla \lambda : \delta \mathbf{c} : \nabla \mathbf{s} - \lambda \cdot \delta \mathbf{f}) d^2 \mathbf{x} dt \\ & - \int_0^T \int_{\Omega} [\rho \partial_t^2 \lambda - \nabla \cdot (\mathbf{c} : \nabla \lambda)] \delta \mathbf{s} d^2 \mathbf{x} dt \\ & - \int_{\Omega} [\rho (\lambda \cdot \partial_t \delta \mathbf{s} - \partial_t \lambda \cdot \delta \mathbf{s})]_T d^2 \mathbf{x} - \int_0^T \int_{\partial \Omega} \hat{\mathbf{n}} \cdot (\mathbf{c} : \nabla \lambda) \cdot \delta \mathbf{s} d^2 \mathbf{x} dt \end{aligned} \quad (6.3)$$

To make the variation in the 6.3 be stationary with respect to perturbations of displacement $\delta \mathbf{s}$. The perturbations of the model parameters $\delta \rho$, $\delta \mathbf{c}$ and $\delta \mathbf{f}$ can be ignored, the Lagrange multiplier λ is required to satisfy the equation

$$\rho \partial_t^2 \lambda - \nabla \cdot (\mathbf{c} : \nabla \lambda) = \sum_r [\mathbf{s}(\mathbf{x}_r, t) - \mathbf{d}(\mathbf{x}_r, t)] \delta(\mathbf{x} - \mathbf{x}_r) \quad (6.4)$$

Introducing the above solution of the Lagrange multiplier λ into Eq. (6.3) with free surface condition, the variation in the action (6.3) can be reduced to

$$\delta \chi = - \int_0^T \int_{\Omega} (\delta \rho \lambda \cdot \partial_t^2 \mathbf{s} + \nabla \lambda : \delta \mathbf{c} : \nabla \mathbf{s} - \lambda \delta \mathbf{f}) d^2 \mathbf{x} dt \quad (6.5)$$

If the Lagrange multiplier wavefield λ is defined as the adjoint wavefield \mathbf{s}^\dagger , which is

$$\mathbf{s}^\dagger(\mathbf{x}, t) = \lambda(\mathbf{x}, T - t) \quad (6.6)$$

Thus the adjoint wavefield \mathbf{s}^\dagger is equal to the time-reversed Lagrange multiplier wavefield λ . The adjoint wavefield \mathbf{s}^\dagger is determined by

$$\rho \partial_t^2 \mathbf{s}^\dagger - \nabla \cdot \mathbf{T}^\dagger = \sum_r [\mathbf{s}(\mathbf{x}_r, t) - \mathbf{d}(\mathbf{x}_r, t)] \delta(\mathbf{x} - \mathbf{x}_r) \quad (6.7)$$

Where the adjoint stress \mathbf{T}^\dagger is defined in terms of the gradient of the adjoint displacement as follows,

$$\mathbf{T}^\dagger = \mathbf{c} : \nabla \mathbf{s}^\dagger \quad (6.8)$$

It can be observed that the adjoint wavefield is governed by the same wave equation, up to the source term: for the real wavefield, the source term corresponds to the real excitation, while for the adjoint wavefield it results from the time reversed difference between the synthetics \mathbf{s} and experimental data \mathbf{d} at the different receivers. Replacing the Lagrange multiplier by the adjoint wavefield, the gradient of the misfit function can be rewritten as

$$\delta\chi = - \int_0^T \int_\Omega (\delta \ln \rho K_\rho + \delta \mathbf{c} : K_\mathbf{c}) d^2 \mathbf{x} dt + \int_0^T \int_\Omega \mathbf{s}^\dagger \cdot \delta \mathbf{f} d^3 \mathbf{x} dt \quad (6.9)$$

Where we have defined the following primary sensitive kernels

$$K_\rho(\mathbf{x}) = - \int_0^T \rho(\mathbf{x}) \mathbf{s}^\dagger(\mathbf{x}, T-t) \cdot \partial_t^2 \mathbf{s}(\mathbf{x}, t) dt \quad (6.10)$$

$$K_\mathbf{c}(\mathbf{x}) = - \int_0^T \nabla \mathbf{s}^\dagger(\mathbf{x}, T-t) \nabla \mathbf{s}(\mathbf{x}, t) dt \quad (6.11)$$

The elastic tensor in Eq. (6.9) can be repressed in terms of bulk and shear moduli denoted by κ and μ , consequently, the misfit function (6.9) becomes

$$\delta\chi = \int_\Omega (K_\rho \delta \ln \rho + K_\kappa \delta \ln \kappa + K_\mu \delta \ln \mu) d^2 \mathbf{x} \quad (6.12)$$

Where the corresponding primary kernels are just linear combinations of K_ρ and $K_\mathbf{c}$ given by

$$K_\rho(\mathbf{x}) = \rho(\mathbf{x}) \int \partial_t \mathbf{s}^\dagger(\mathbf{x}, T-t) \cdot \partial_t \mathbf{s}(\mathbf{x}, t) dt \quad (6.13)$$

$$K_\kappa(\mathbf{x}) = -\kappa(\mathbf{x}) \int [\nabla \cdot \mathbf{s}^\dagger(\mathbf{x}, T-t)] [\nabla \cdot \mathbf{s}(\mathbf{x}, t)] dt \quad (6.14)$$

$$K_\mu(\mathbf{x}) = -2\mu(\mathbf{x}) \int \mathbf{D}^\dagger(\mathbf{x}, T-t) : \mathbf{D}(\mathbf{x}, t) dt \quad (6.15)$$

Where $\mathbf{D} = (1/2)[\nabla \mathbf{s} + (\nabla \mathbf{s})^T] - (1/3)(\nabla \cdot \mathbf{s})\mathbf{I}$. Instead of density and the shear and bulk moduli, it is physically more significant to rewrite the derivation with respect to density and shear and compressional velocities. The corresponding volumetric

kernels $K_{\hat{\rho}}$, K_{α} and K_{β} represent the sensitivity of the misfit function with respect to small perturbations of the density, shear and compressional velocities, respectively.

$$K_{\hat{\rho}} = K_{\rho} + K_{\kappa} + K_{\mu} \quad (6.16)$$

$$K_{\beta} = 2 \left(K_{\mu} - \frac{4}{3} \frac{\mu}{\kappa} K_{\kappa} \right) \quad (6.17)$$

$$K_{\alpha} = 2 \left(\frac{\kappa + 4/3\mu}{\kappa} \right) K_{\kappa} \quad (6.18)$$

With this new parametrization, the perturbation of the misfit function (6.12) can be rewritten as:

$$\delta\chi = \int_{\Omega} (K_{\hat{\rho}}\delta\ln\rho + K_{\alpha}\delta\ln\alpha + K_{\beta}\delta\ln\beta) d^2\mathbf{x} \quad (6.19)$$

6.1.1 The connection between imaging and adjoint kernels

Claerbout's imaging principle states that 'reflectors exist at points in the ground where the first arrival of the downgoing wave is time coincident with an upgoing wave' (Claerbout, 1971). Basically, this principle gives us an approximation to the spatial distribution of reflection coefficients. (Tarantola, 1984) realized that the density waveform sensitivity kernel is closely related to the imaging principle. The relationship between the density kernel K_{ρ} and the imaging principle can be briefly illustrated as follows. The image formation can be understood as an integration of the up- and down-going wavefields in time. In seismic migration, the down-going (resp. up-going) velocity wavefield is related to the forward (resp. adjoint) displacement field. By substituting these relationships into the imaging formation, which is an integration of the up- and down-going wavefields in time, the imaging formation becomes familiar with the definition of density kernel K_{ρ} . For multicomponent data in an elastic medium, (Kiyashchenko et al., 2007)) proposes a modified imaging formulation by involving an additional term similar to our bulk kernel K_{μ} . This modified imaging formulation looks very similar to the sum of our density and bulk kernels, i.e., our impedance kernel $K_{\hat{\rho}}$ in the acoustic approximation. In the next sections, we will see that the impedance kernel is indeed a more natural choice for image formation, leading to crisper images of the reflectors in the medium.

6.1.2 Numerical implementation of sensitive kernels

In order to calculate the primary and secondary kernels defined in the above section, we have used the software Specfem2D ((Komatitsch and Tromp, 2002;

Komatitsch et al., 2016; Liu and Tromp, 2008)). This software allows to simulate both the forward and adjoint seismic wave propagation in two dimensional acoustic, elastic, poroelastic or coupled acoustic-elastic-poroelastic media, including PML (Perfectly Matched Layer) absorbing conditions. The specfem2D suits well to parallel implementation on very large supercomputers.

It can be also used in the previous TDTE imaging by adding the definition of TDTE kernel (3.7), which are involving the production between forward and adjoint wavefield same as sensitive kernels.

The mesh generation is a critical point for a spectral-element simulation. Ideally, the mesh should honor all first- and second-order discontinuities in the geologic model, contain at least five points per shortest wavelength.

By observing the mathematical formulation of the different kernels of interest: Eq. (6.13,6.14,6.15), we simultaneously need the forward wavefield \mathbf{s} at time t as well as the adjoint wavefield \mathbf{s}^\dagger at time $T - t$. This condition rules out the possibility of carrying both the forward and adjoint simulations simultaneously in a unique simulation scenario, as both wavefields would be calculated at the same time t . The most intuitive approach consists in running the forward simulation first and record the resulting wavefield at all points of the spatial domain and time, then launch the adjoint simulation. Once both simulations have been fully completed, the two forward and adjoint fields can be mixed together and integrated in time, according to Eq. (6.13,6.14,6.15).

The main inconvenient of this approach is that a large simulation (large spatial domain and/or simulation on a large time interval) may require a large amount of disk storage. This issue is efficiently managed by Specfem2D in the particular case of non-attenuating propagation media: in this case, the forward and adjoint problems are solved simultaneously, such that the final temporal integration can be realized directly, without saving huge data on the disk. The backward wavefield, which is forward simulation on the time direction of $T - t$, is determined by

$$\rho \partial_t^2 \mathbf{s} = \nabla \cdot (\mathbf{c} : \nabla \mathbf{s}) + \mathbf{f} \tag{6.20}$$

$$\mathbf{s}(\mathbf{x}, T) \text{ and } \partial_t \mathbf{s}(\mathbf{x}, T) \text{ given} \tag{6.21}$$

$$\hat{\mathbf{n}} \cdot (\mathbf{c} : \nabla \mathbf{s}) = 0 \text{ on } \partial\Omega \tag{6.22}$$

This initial and boundary value problem can be solved to reconstruct the forward wavefield $\mathbf{s}(\mathbf{x}, t)$ in the time interval $[0, T]$, which is the same as the wave equation solved for the forward simulation. Technically, the only difference between the backward and forward problems reduces to a change of the sign for the time variable. This gives the possibility to perform both the forward and adjoint simulations simultaneously, the forward wavefield at time t corresponding to the adjoint wavefield at time $T - t$, resulting in an immediate computation of the product and resulting integration over time. The immediate consequence is that it is no more needed to store the whole wavefields in space and time. An advantage of this approach is that only the wavefield at the last time step of the forward simulation needs to be stored and finally reloaded for the reconstruction of $\mathbf{s}(\mathbf{x}, t)$ and the computation of the kernels.

So, we can give a procedure of numerical implementation of computing kernels by `specfem2D`: firstly, define the reference medium and mesh the medium with embedded or third-party mesh generator, then run the forward simulation, the received synthetic seismograms are used to be constructed the adjoint source, only the last frame is recoded (for solving backward wave equation). Secondly, operate the adjoint simulation, which this procedure consists in: 1) the adjoint wave filed by adjoint source in time $t = \{0 \rightarrow T\}$, 2) reconstruct the forward wavefield in time $t = \{T \rightarrow 0\}$ from the recoded last frame at T through (6.20), 3) compute the adjoint kernel by accumulating the product between the forward and adjoint wavefield along time. The first three sub-procedures are performing simultaneously in `Specfem2D`.

Practically, the computation of the kernels follows the steps below:

- we first define the reference medium and create a mesh of it using a mesh generator (embedded or third-party software),
- this mesh is used by `Specfem2D` to calculate the received synthetic seismograms that will be used as adjoint sources (after a time-reversal operation),
- the last frame is recorded to solve the backward wave equation,
- we then simulate the adjoint problem and reconstruct the forward wavefield in time from the last recorded frame; meanwhile, the adjoint kernel is processed.

6.2 Numerical imaging of cortical bone internal boundary by adjoint kernels

The migration principle by adjoint method is similar to Time domain Topological energy, in the sense that a reference medium close to the real model produces better results. If the reference medium is water (acoustic medium), the adjoint method will encounter a mismatch in the spatial domain that corresponds to cortical bone (elastic medium) in the computation of the elastic kernel.

Considering the previous chapters, TDTE is an efficient approach to obtain the external boundary of the cortical bone with just one iteration. This preliminary information will reduce the calculation significantly. Here we use this information to build the new reference medium before applying the migration principle. Consequently the new reference medium is now made of two materials, with a boundary that results from the previous TDTE processing. The medium above the boundary is water, while the medium below the boundary is made of bone material. This is fundamentally equivalent to the second iteration of TDTE discussed in chapter 5. The elastic kernel is finally calculated to obtain a spatial distribution of density, and longitudinal and transverse velocities inside the cortical bone.

The initial reference medium is illustrated on Fig. 6.1 (identical to Fig. 5.4 in Chapter 5). A linear array of 128 elements (spatial pitch 1.1mm, represented by the green stars), is used to transmit and receive signals. The emitted signal is a 3.5MHz sinusoid pulse modulated by a Gaussian envelop, with a bandwidth of 1MHz at -6dB. The parameters for the bone-mimicking material (Sawbone) are the same as those used in Chapter 4 Table. 4.4. The other important parameters are as flow:

- the temporal sampling: $2.5e^{-2}\mu s$ (sampling frequency 40MHz),
- total number of temporal steps: 48000 (total duration 1200 μs),
- boundary condition: PML,
- horizontal number of grid points: 400 (spatial step 0.35mm).
- recorded type of seismography: pressure

Firstly, the received signal $\mathbf{y}(t)$ back-propagated from inspected cortical bone is recorded by performing the simulation on the medium Fig. 6.1(a). In this regular simulation, the simulation type of SPEC-FEM2D was set to 1, which is indicated

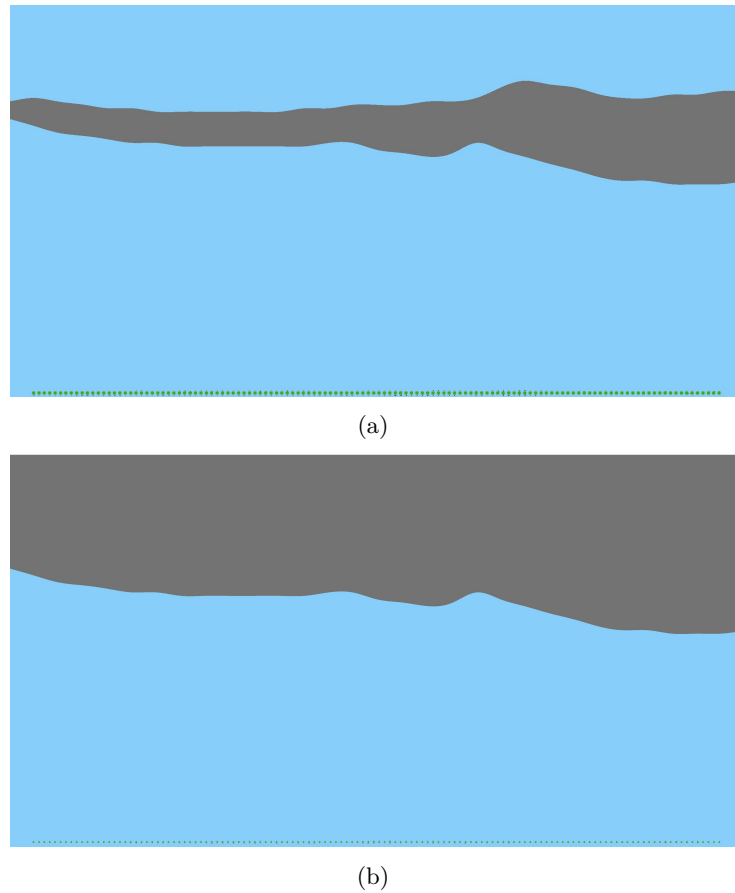


Figure 6.1: (a) the numerical setup of cortical bone when array located in 0 degree (b) the numerical setup of reference medium in specfem2D (the gray and blue areas correspond to the cortical bone and water, respectively, the green stars represent the transducer array)

forward simulation. Option of `SAVE_FORWARD` was set to false, which means the last frame don't need to be saved.

The following step for the migration in cortical bone imaging is illustrated on Fig. 6.2. We first run the forward simulation with Specfem2D (simulation type =1, `SAVE_FORWARD` = true), consequently, the resulting outputs are i) the wavefield at the last temporal frame and ii) the received signals $\mathbf{y}_1(t)$. Then we calculate the adjoint source resulting from the difference between the real received signals $\mathbf{y}(t)$ and $\mathbf{y}_1(t)$. The last step consists in using Specfem2D (simulation type =3, which indicates the adjoint simulation, `SAVE_FORWARD` = false) again to calculate the adjoint simulation and perform the temporal integration described by Eq. (6.14, 6.15, 6.16). As discussed above, i) the wavefield integration between

forward and adjoint fields and ii) the sensitive kernels are computed simultaneously.

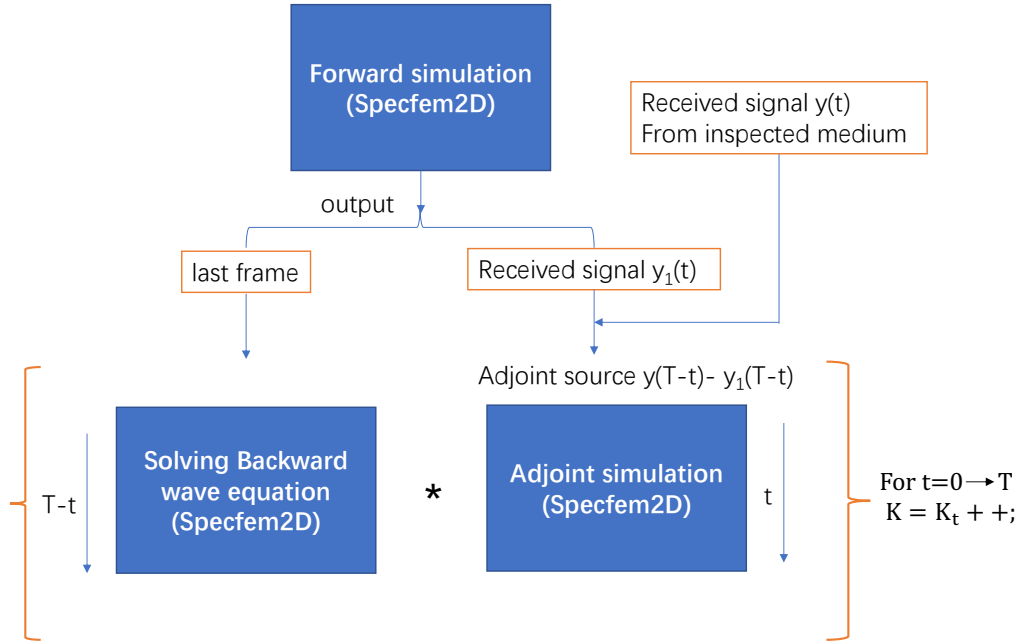


Figure 6.2: the scheme of numerical simulation perform by Specfem2D

The six primary and secondary kernels are illustrated on Fig. 6.3 (left: density, shear and bulk modulus kernels, right: Impedance, transverse and longitudinal velocities). On this figure, the obtained kernels are shown only inside the elastic domain. As discussed previously, the density kernel K_ρ is equivalent to the imaging principle. Notice that, the K_ρ , K_κ , K_μ , K_α are representative of the internal boundary of the cortical bone. On the contrary, K_μ , K_β are not sensitive to this internal boundary.

However, when K_ρ , K_κ and K_μ are summed to produce the 'impedance' kernel $K_{\hat{\rho}}$ (Figure 6.3(b)), the low-frequency artifacts disappear. It can be observed that the impedance kernel ($K_{\hat{\rho}}$) looks similar to the density kernel (K_ρ) for internal boundary of cortical bone, but with better contrast. The density represents the main contribution to the impedance kernel, while the shear modulus kernel plays a secondary role in the production of the impedance kernel.

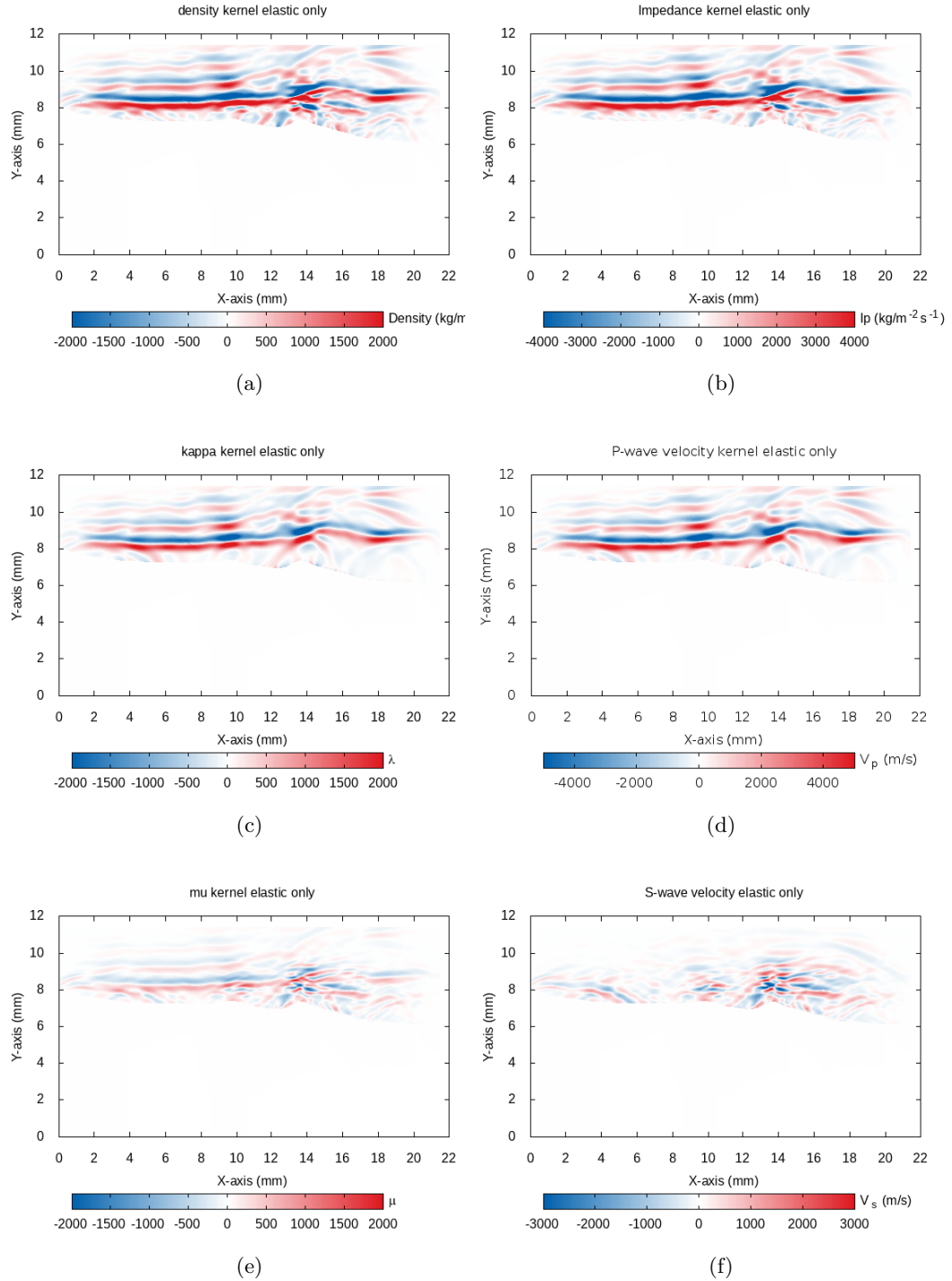


Figure 6.3: (a) K_ρ kernel (b) K_β kernel (c) K_κ kernel (d) K_α kernel (e) K_μ kernel (f) K_β kernel

It can be also observed that K_μ and K_β , both related to the shear modulus, have weak amplitudes in the top of the spatial domain, corresponding to the acoustic area.

For better observation of the internal boundary of cortical bone, we change the color bar to disable the miner?s value of K_α kernel, where the internal boundary are more visible, shown in Fig. 6.4.

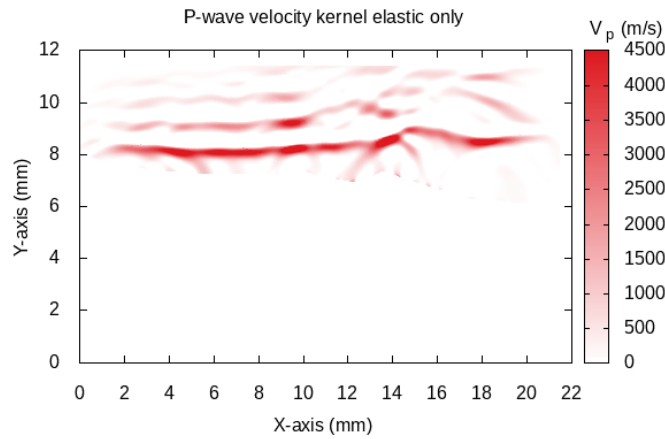


Figure 6.4: K_α kernel

In this simulation we used the same central frequency 3.5 MHz of excitation as the TDTE. It shows the same performance with the TDTE in the aspect of imaging the boundary of cortical bone. However, the migration should give more information on the distribution of density, P-wave and S-wave velocity, since the migration is the first iteration of FWI, where the minimization of misfit is based on gradient descend. This means the first iteration should provide a sufficient solution. By observing the Fig. 6.3, almost all the information focus on the internal boundary of cortical bone. To obtain more information on the distribution of density, P-wave and S-wave velocity, we decrease the central frequency of excitation to 800 KHz, of which the half wavelength is approximate to the cortical thickness. The corresponding six kernels are shown in Fig. 6.5. It can be observed that the K_ρ , $K_{\hat{\rho}}$, K_κ , K_α kernels can give a rough distribution of density and P-wave velocity of cortical bone, K_μ and K_β kernel give a relevant poor distribution of S-wave velocity of cortical bone, however, they can indicate where the S-wave

velocity equals to zero (above cortical bone).

Based on these results, we can conclude that the migration principle can give information about the internal boundary of the cortical bone, and a spatial distribution of density and transverse and longitudinal velocities. High frequency can provide better interface information with poorer distribution of density, P- and S-wave velocity, vice versa, low frequency can provide better distribution but poor interface information.

To obtain a more accurate spatial distribution of these physical parameters, an iterative procedure (known as Full Waveform Inversion) is needed.

6.3 Full waveform inversion

Theoretical analyses suggest that FWI includes two modes: tomography and migration ((Mora, 1989)). The tomographic model are normally related to data with large offsets, which are rich in refractions and wide angle reflections. Applying standard FWI on the reflections from this type of data sets is essentially equivalent to carrying out nonlinear least squares migration (e.g., (Wu et al., 2016); (Yao and Jakubowicz, 2015)). Migration model of FWI dominates the inversion. Although the inversion also includes the tomographic mode, it is much weaker than the migration mode.

Once again, FWI searches for a velocity model that produces a full wavefield that best fit the observed full wavefield. This is generally performed by an iterative non-linear optimized approach using a gradient method, represented as formula (6.1). The gradient is formula (6.11) calculated by adjoint method, the negative gradient shows the steepest descent direction, i.e. where the data residuals decrease the most. The obtained model of one iteration, provides the starting model for the next iteration. So the misfit function can be rewritten in the form of

$$\chi(\mathbf{m}) = \frac{1}{2} \sum_r \int_0^T [\mathbf{s}(\mathbf{m}, \mathbf{x}_r, t) - \mathbf{d}(\mathbf{m}, \mathbf{x}_r, t)]^2 dt. \quad (6.23)$$

Though the above misfit function, represented a conventional waveform-difference measure of fit, FWI explicitly casts the inversion problem as a nonlinear optimization procedure. In this approach, the wave speed model \mathbf{m} is iteratively improved by using a nonlinear optimization algorithm to minimize the waveform differences.

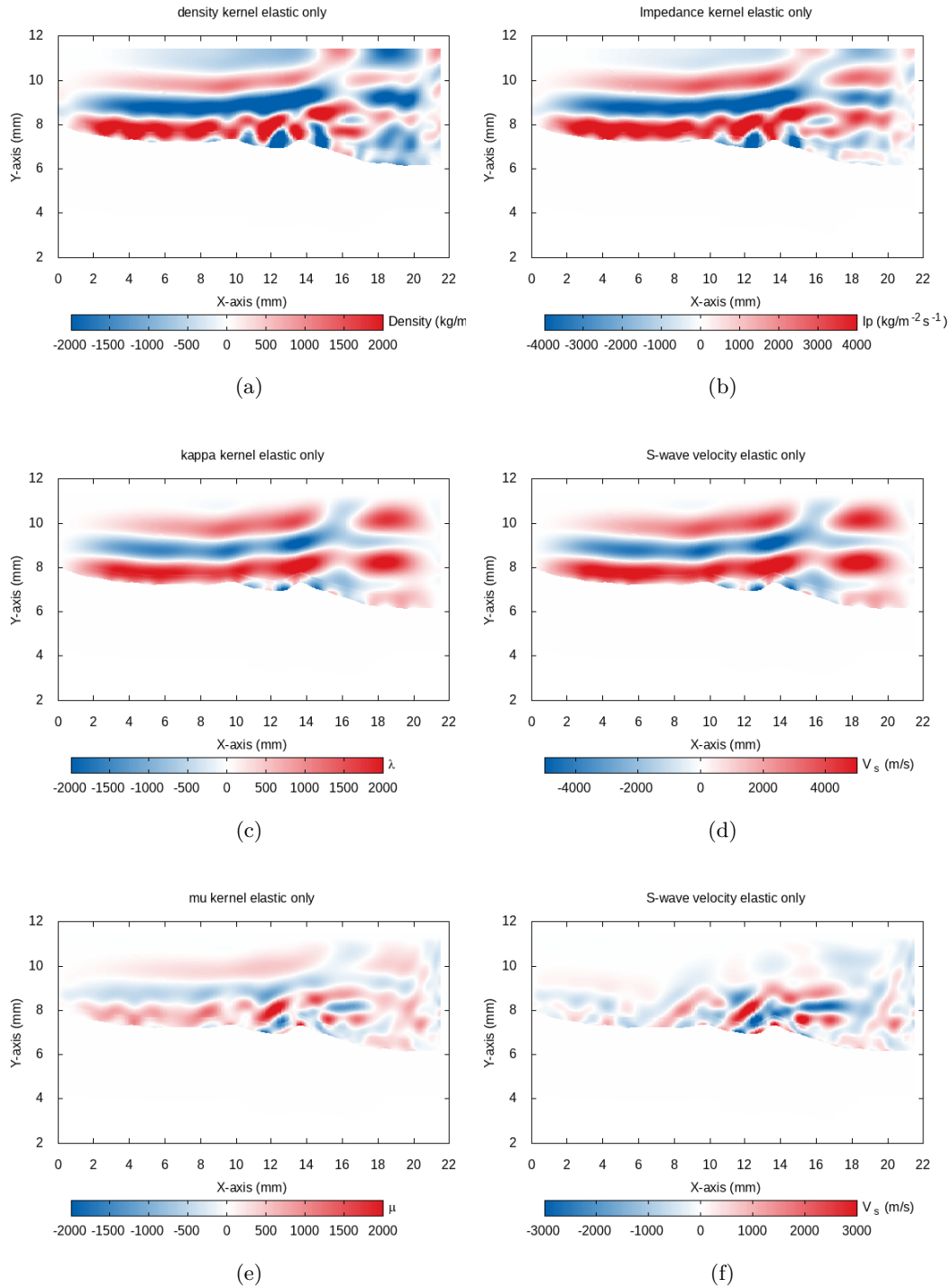


Figure 6.5: (a) K_ρ kernel (b) $K_{\hat{\rho}}$ kernel (c) K_κ kernel (d) K_α kernel (e) K_μ kernel (f) K_β kernel

This minimization can be solved by the l_2 norm. In the vicinity of \mathbf{m} , the misfit function can be expanded into a Taylor series:

$$\chi(\mathbf{m} + \delta\mathbf{m}) = \chi(\mathbf{m}) + \mathbf{g}(\mathbf{m}) \cdot \delta\mathbf{m} + \delta\mathbf{m} \cdot \mathbf{H}(\mathbf{m}) \cdot \delta\mathbf{m} \quad (6.24)$$

Where the $\mathbf{g}(\mathbf{m})$ is the gradient of the waveform misfit function, and has been solved in above section. $\mathbf{H}(\mathbf{m})$ is the Hessian:

$$\mathbf{H}(\mathbf{m}) = \frac{\partial^2 \chi(\mathbf{m})}{\partial \mathbf{m}^2}. \quad (6.25)$$

By assuming the gradient and Hessian on the model are dependent, a Hessian-based algorithm utilized both the gradient and Hessian can be obtained a model update. The model update is determined by Newton method,

$$\delta\mathbf{m} = -\mathbf{H}^{-1} \cdot \mathbf{g}. \quad (6.26)$$

The local minimum of (6.23) is thus given by perturbing the model in the direction of the gradient preconditioned by the inverse Hessian.

The Hessian-based algorithm has a quadratic convergence rate; however, it suffers from exorbitant computational costs as well as huge storage requirements. Quasi-Newton methods, such as L-BFGS (Liu and Nocedal, 1989), estimate the Hessian based on gradients from previous iterations, and thus have good convergence rates yet relatively modest computational costs. Limited-memory BFGS (L-BFGS or LM-BFGS) is an optimization algorithm in the family of quasi-Newton methods that approximates the Broyden-Fletcher-Goldfarb-Shanno (BFGS) algorithm using a limited amount of computer memory. By applying L-BFGS to estimate Hessian, we can update the model by

$$\mathbf{m}_{k+1} = \mathbf{m}_k - \sigma_k \mathbf{H}_{QN}^{-1} \mathbf{g}_k \quad (6.27)$$

where H_{QN}^{-1} is the L-BFGS approximation to the inverse Hessian, σ_k is the step length determined by the line search, k represents the k -th iteration. And each step of gradient is illustrated in above section, which is the sum of kernels (6.19) by adjoint method. Actually the standard FWI is the iterative procedure of migration.

6.4 Numerical Implement

The iterative inversion workflow may comprise three main steps for which tools are provided:

- Summing event kernels, K_α , K_β , K_ρ to build the misfit gradient $\mathbf{g}(\mathbf{m})$
- Smoothing and post-processing of the gradient $\mathbf{g}(\mathbf{m})$
- Updating the model based on (6.27)

For both the nonlinear optimization procedure itself and related pre- and post-processing tasks, it can be applied with the SeisFlows framework (Modrak et al., 2018) (github.com/rmodrak/seisflows). Forward and adjoint modelings are carried out using SPECFEM2D. The workflow of SeisFlows are shown in Fig. 6.6.

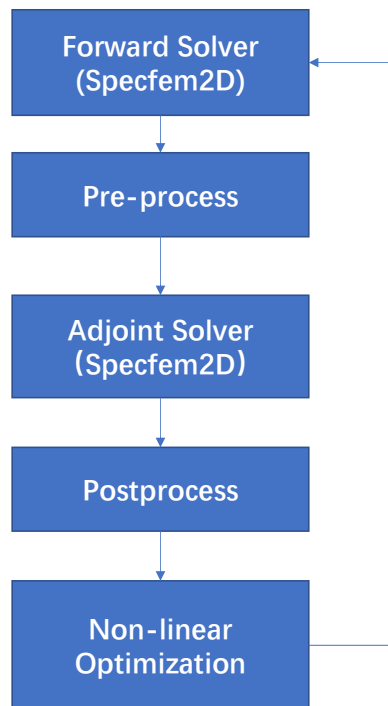


Figure 6.6: the scheme of Full waveform inversion

6.4.1 pre-processing, post-processing, Nonlinear optimization

In Seisflow framework, preprocessing refers to operations carried out on seismic traces, encompassing both $\chi(m)$ and $\mathbf{s}(\mathbf{x}_r, t)$ in Eq. 6.1. The name reflects the fact

that such operations are usually performed prior to data residual back-projection. The default preprocessing class works with time-domain data and relies on `obspy` (a Python framework for processing seismological data, <https://docs.obspy.org>) for reading and writing data and signal processing.

Post-processing refers to image processing operations on models, sensitivity kernels, or migrated images. Post-processing operations are usually performed after data back-projection. A wide variety of operations are included this category in `seisflow`. Workflow including smoothing, basis projection, and Tikhonov and total variation regularization. Because post-processing operations are sometimes performed directly on the model or kernels as expressed in the spectral element basis used by `SPECFEM2D` solver, there may be some overlap between the solver and post-processing component. `SeisFlows` use standalone utilities in the `SPECFEM2D` packages for smoothing operations on spectral-element bases, rather than reimplementing these operations in Python.

The nonlinear optimization of model update is divided into two steps. First, a search direction is computed based on the gradient of the objective function. Second, a step length is determined along the search direction through a line search procedure. The Limited-memory BFGS algorithm (L-BFGS) (Liu and Nocedal, 1989) is a quasi-Newton method, which means that search directions are based on a low-dimensional quadratic model of the objective function. After several decades of experience with such methods, L-BFGS is generally regarded as the most effective quasi-Newton method ((Nocedal, 1992)). L-BFGS uses an estimation to the inverse Hessian matrix to steer its search through variable space, it stores only a few vectors that represent the approximation implicitly. Due to its resulting linear memory requirement, the L-BFGS method is particularly well suited for optimization problems with a large number of variables. It is limited-memory in the sense that results from only the most recent gradient evaluations need to be stored.

Here we give an illustration of the L-BFGS. For a given initial model \mathbf{m}_0 , objective function f is being minimized, diagonal scaling \mathbf{D} , memory value l , and stopping threshold $\delta > 0$, the p_k is descent direction $\mathbf{H}_{QN}^{-1}\mathbf{g}$ in the k -th iteration. The L-BFGS algorithm is as follows:

It should be noticed that the symbols λ , μ are irrelevant with same symbols that appear elsewhere. L-BFGS's relatively modest memory usage rests on the fact

Algorithm 3 Limited-memory BFGS algorithm

- 1: Evaluate $f_0 = f(\mathbf{m}_0)$, $g_0 = \nabla f(\mathbf{m}_0)$.
 - 2: Set $p_0 = -g_0$, $k = 1$
 - 3: **while** $g_{k+1}^T g_{k+1} < \delta$ **do**
 - 4: Set $q = g_k$, $i = k - 1$, $j = \min(k, l)$
 - 5: Performing j times: $\lambda_i = \frac{s_i^T p}{y_i^T s_i}$, $q = q - \lambda_i y_i$, $i = i - 1$
 - 6: Set $\gamma = \frac{s_{k-1}^T y_{k-1}}{y_{k-1}^T y_{k-1}}$, $r = \gamma Dq$, $i = k - j$
 - 7: Performing j times: $\mu = \frac{y_i^T r}{y_i^T s_i}$, $r = r + s_i(\lambda_i - \mu)$, $i = i + 1$
 - 8: **return** $p_k = -r$
 - 9: Compute ζ_k by line search and set $\mathbf{m}_{k+1} = \mathbf{m}_k + \zeta_k p_k$
 - 10: Evaluate $f_{k+1} = f(\mathbf{m}_{k+1})$, $g_{k+1} = \nabla f(\mathbf{m}_{k+1})$.
 - 11: Set $s_k = \mathbf{m}_{k+1} - \mathbf{m}_k$, $y_k = g_{k+1} - g_k$, $k = k + 1$.
 - 12: **end while**
-

that if k is the current iteration number and l is the memory value, then vector pairs prior to $\{s_{k-l}, y_{k-l}\}$ are no longer needed and can be removed from storage. The scaling factor γ , which accounts for differences between the true Hessian and the approximation thereto, is essential to the good performance of the algorithm.

6.4.2 Numerical implement

In this simulation, the map, initial model and transducers are set the same as the last section, other main parameters are as follow:

- number of iterations: 15
- step thresh in each optimization of line search: $\zeta = 0.2$
- maximum trial steps for each optimization: 10
- central frequency of emitted signal $f_0 = 800$ kHz
- solver: SPEC-FEM2D
- optimize algorithm: LBFGS

Unfortunately, after 15 iterations of FWI, the FWI couldn't obtain sufficient distribution of shear wave, more times iteration is still required. Since the reason of limited time, we didn't obtain a satisfied final result in the end of thesis writing,

this work needs to be gone further in future with more iterations. According to the experience from (Nguyen and Modrak, 2018), the reconstruction of elastic medium shown in Fig. 1.7 is not accurate enough, even with a sufficient iterations. However, in the perspective of efficiency, the migration with low frequency has already given us sufficient result with only one iteration. It seems migration is a better strategy than FWI in cortical bone imaging.

CHAPTER 7

Summary and conclusion

Applying ultrasound into cortical bone evaluation has been attracted significant attention in past decades, since the affordable and non-radiation of ultrasound. The evaluation of cortical bone including the mechanical properties: cortical thickness, density, elasticity and stiffness. On the other hand, the imaging of cortical bone is also providing us more information on structure with a more intuitively and macroscopically.

The mechanical parameters of cortical bone mainly involving in parameter estimation, which is a classical and well-developed issue. In this study, the sparse signal processing shows promising performance compared with traditional signal processing methods in ultrasound parameter estimation, especially the sparse signal processing method open a new way for broadband ultrasound attenuation of cortical bone *in vivo* estimation.

In other committees such as NDT and geophysics, they face the same challenge with cortical bone imaging by ultrasound. TDTE shows a promising result in imaging the low impedance contrast media and porous media. For quantitative imaging, seismic migration and Full waveform inversion are playing the central role in geophysics for reconstruction interior of earth, which can provide density, P-wave velocity and S-wave velocity distributions.

7.1 Summary

The contributions of this thesis are in two aspects: First is introducing sparse signal processing to estimate the cortical thickness and broadband attenuation *in vivo* with a mono ultrasound transducer efficiently. Second is introducing Time Domain Topological Energy and adjoint tomography to cortical bone imaging with ultrasound transducer array.

Compared to traditional method with a mono transducer array, only the time delay can be estimated. By introducing the OMP on the same configuration, a more precisely result can be obtained and with an additional benefit, which the broadband attenuation can be estimated *in vivo* simultaneously. As far as

we know, this is the first time the BUA (Broadband Ultrasound Attenuation) of cortical bone estimated *in vivo* at radius. This work is a preliminary study with only several volunteer's validation, which has shown a promising result, a widely validation need to be done in the future.

The meaning of this part of work is by introducing advanced signal processing method, endowing a traditional approach with more parameters estimation. It will accumulate the promotion of clinical application, as a simple configuration to estimate the thickness and BUA of cortical bone. Especially as an affordable mean for high risk population screening

Imaging methods based on time reversal is limited in cortical bone domain, since the high contrast between the soft tissue and cortical bone, the signal from the inner bone is usually very weak. With the development of computational capacity recently, one kind of imaging method based on numerical simulation has been risen. Time domain topological energy, based on the principle of inserting the hole in the reference medium to make it closer to the real inspected medium, shows a promising result in NDT. And it has a primary application is medical soft tissue imaging. This is the first time we introduce TDTE in cortical bone imaging. By using a simple homogeneous fluid reference medium, the TDTE image can be obtained efficiently. However, this efficient choice of reference medium, only the external boundary of cortical bone can be reconstructed well, the internal boundary of cortical bone is week in the TDTE image and mismatched with its real position.

There are two different ideas to deal with this problem: one is to increase the time-delay and amplify the amplitude of the second main echo, which is corresponding to the internal boundary. This involves the signal processing of time delay estimation. By applying the OMP we used in previously part, the second main echo can be reconstructed by amplifying the amplitudes and increasing the time delays, which is the ratio between the wave velocity in cortical bone and reference medium (water). This approach can successful reconstruction the external and internal boundary of cortical bone in numerical simulation and sawbone of femur neck. However, it only can handle the regular internal boundary. For irregular internal boundary, the echoes corresponding to the internal boundary are difficult to identify. Under such circumstance, the iterative TDTE by improving the reference medium with previous iteration information is the only option. In cortical bone imaging application, the reference medium in second iteration should utilize

the information from the first iteration, by setting the material under external boundary to be bone. So, the second iteration of TDTE can reconstructed the difference between the real inspected cortical bone and updated reference medium, which is the internal boundary of cortical bone. The disadvantage of iterative TDTE is the computation and storage burden. For a homogenous reference medium, the displacement wavefield can be obtained by analytical solution, for the non-homogenous medium, the displacement of wave filed can be obtained only by the numerical simulation software. So, both of the forward and adjoint wavefield need to be stored. The iterative TDTE are also show a good performance in numerical simulation and sawbone of femur neck. For the irregular internal boundary and osteoporosis, the iterative TDTE is irreplaceable, especially the 2nd iterative TDTE can reconstruct the pores with diameter equaling to 0.05mm.

The TDTE with sparse signal processing or iterative TDTE can give a satisfied solution on cortical bone imagine. However, it only can give the geometry structure information, but can't give a quantitative image. In geophysics domain, migration and Full waveform inversion are widely used to give the image as well as the quantitative information of earth interior, including distribution of density, P-wave velocity and S-wave velocity. It has the familiar principle with TDTE, which is trying to minimize the difference between the reference model and inspected model. Both of them are solving minimization of misfit function by adjoint method, involving simulating the forward and adjoint field on reference model. The difference between them is the derivation of misfit function. TDTE is driven from topological optimization, the derivation of misfit function is mainly based on the structure of reference medium. In the migration and FWI, the minimization is respected on the model parameters: density, P-wave velocity and S-wave velocity. So, the minimization of misfit function yields six sensitive kernel, represented the distribution of density, P-wave velocity and S-wave velocity.

The migration imaging by six sensitive kernels are produced by one step gradient minimization, which means the migration only gives a rough quantitative distribution of parameters. It tries to provide the solution which is most closed to the real model in one iteration. In the numerical simulation, we can observe that, the density and impedance kernels can provide us the internal boundary of cortical bone, but the accurate parameters distribution is not sufficient. If we want to obtain more accurate distribution, the iterative procedure is required, which is full waveform inversion.

7.2 Comparison between TDTE, migration and full waveform inversion

In the second part of this thesis, we use one category of imaging method based on the minimization of the difference between real medium and reference medium, this category including: TDTE, migration and full wave form inversion. Each of them has different advantages and disadvantages. Based on the validation in numerical simulation and bone phantom, we give the following comparison in Table. 7.1.

Here we give some explanation of the Table:

1. Both of the three methods require compute two wavefield: forward and adjoint. Among them, one-time iteration of TDTE do not require simulation software. For second iteration of TDTE, a FDTD based software is used here and it is also efficient in recording the two wavefield.
2. For migration and FWI, a widely used software Specfem2D based on spectral element simulation is used here. One special feature of this software is which it can avoid store the displacement of the two wave-fields. It uses backward simulation from the last frame, so in the integration, the displacement of forward and adjoint wavefield can be multiplied simultaneously. As a consequence, the forward simulation needs to run two times.
3. In imaging the small holes inside the cortical bone, the iterative TDTE is more promising, since the FWI requires computationally expensive high-frequency numerical wave simulations.

All these imaging methods introduced in this thesis are based on to minimize the distance between the reference medium and inspected medium, the minimization is solved by introducing adjoint method. The gradient of Full waveform inversion gives a descent direction for the optimization of continuous parameters that are defined on the whole domain, it minimizes the cost function through modify the parameter distribution. TDTE (Topological gradient) allows a real modification of the topology of the domain, it minimize the cost function through topology modification. Consequently, the TDTE is more sensitive in structure imaging and FWI (migration) is more sensitive in reconstruction of parameter distribution. Here we also give a capacity illustration between them:

Where the number of + quantification of the capacity.

By the above illustration, the three methods can be a compensation for each other. There is one idea need to be noticed recently, which is combing of the time

Table 7.1: the comparison of three imaging method

Method	iteration	computation requirements	storage requirements	advantage	disadvantage
TDTE	1	low(analytical solution)	low(no displacement of wavefield need to be stored).	fast and given the external boundary of cortical bone	1. internal structure is mismatched and week. 2. Can not give the quantitative image
	2	low	high(two wave field need to be stored for the integrating)	can give the internal structure	Can not give the quantitative image
Migration	1	medium (forward simulation need to be run two times, first time is only for recording the last frame, second time is run simultaneously with adjoint simulation)	low(by sepefem software, only the last frame of forward simulation needs to be stored).	can give a rough quantitative image	the distribution is parameters including density, P-wave velocity, S-wave velocity is not sufficient
FWI	several.	high	medium	can give the accurate distribution of density, P-wave velocity and S-wave velocity	the computation requirements is huge, which is limited in clinical application

Table 7.2: the quantify comparison of three imaging method

Method	TDTE	migration		FWI
		Low frequency	High frequency	
Structure information	+++	+	++	+
Parameter distribution	-	++	+	+++
Efficiency	+++	+++	++	-

reversed migration and elastic FWI ((Nguyen and Modrak, 2018)). Reverse-time migration (RTM) can reconstruct reflectors and scatters by cross-correlating the source wavefield and the receiver wavefield given a known velocity model of the background. Ultrasonic waveform tomography based on full-waveform inversion (FWI) has succeeded in detecting anomalous features in engineered structures. But the reconstruction of the wave velocity model of the small-size and high-contrast defects is difficult because it requires computationally expensive high-frequency numerical wave simulations. To reduce computational cost and improve detection of small defects, a useful approach is to divide the waveform tomography procedure into two steps: first, a low-frequency background reconstruction aimed at recovering background structure using FWI, and second, a high-frequency imaging step targeting defects using RTM. In our case, the RTM can be replaced by the TDTE. This kind of combination might provide an new perspective in cortical bone imaging for both the small holes inside the cortical bone and the distribution of density, and elastic parameters.

Bibliography

- W. F. ABENDSCHEIN and G. W. HYATT. ULTRASONICS AND PHYSICAL PROPERTIES OF HEALING BONE. *The Journal of Trauma: Injury, Infection, and Critical Care*, 12(4):297–301, 1972.
- B. Arnal, G. Pinton, P. Garapon, M. Pernot, M. Fink, and M. Tanter. Global approach for transient shear wave inversion based on the adjoint method: a comprehensive 2D simulation study. *Physics in Medicine & Biology*, 58(19):6765–6778, 2013.
- P. Augat, H. Reeb, and L. E. Claes. Prediction of fracture load at different skeletal sites by geometric properties of the cortical shell. *Journal of Bone and Mineral Research*, 11(9):1356–1363, 2009.
- J. Bai, G. Chen, D. Yingst, and J. Leveille. Attenuation compensation in viscoacoustic reverse time migration. In *SEG Technical Program Expanded Abstracts 2013*, pages 3825–3830. Society of Exploration Geophysicists, 2013.
- Y. Bala, R. Zebaze, A. Ghasem-Zadeh, E. J. Atkinson, S. Iuliano, J. M. Peterson, S. Amin, Å. Bjørnerem, L. J. Melton III, H. Johansson, J. A. Kanis, S. Khosla, and E. Seeman. Cortical Porosity Identifies Women With Osteopenia at Increased Risk for Forearm Fractures. *Journal of Bone and Mineral Research*, 29(6):1356–1362, 2014.
- R. Barkmann, P. Laugier, U. Moser, S. Dencks, F. Padilla, G. Haiat, M. Heller, and C. C. Gluer. A method for the estimation of femoral bone mineral density from variables of ultrasound transmission through the human femur. *Bone*, 40(1):37–44, 2007.
- R. Barkmann, P. Laugier, U. Moser, S. Dencks, M. Klausner, F. Padilla, G. Haiat, M. Heller, and C.-C. Glüer. In Vivo Measurements of Ultrasound Transmission Through the Human Proximal Femur. *Ultrasound in Medicine & Biology*, 34(7):1186–1190, 2008.
- R. Barkmann, S. Dencks, P. Laugier, F. Padilla, K. Brixen, J. Ryg, A. Seekamp, L. Mahlke, A. Bremer, M. Heller, and C. C. Gluer. Femur ultrasound (FemUS)—first clinical results on hip fracture discrimination and estimation of femoral BMD. *Osteoporosis International*, 21(6):969–976, 2009.

- D. C. Bauer. Broadband ultrasound attenuation predicts fractures strongly and independently of densitometry in older women. A prospective study. Study of Osteoporotic Fractures Research Group. *Archives of Internal Medicine*, 157(6): 629–634, 1997.
- T. J. Beck, A. C. Looker, F. Mourtada, M. M. Daphtary, and C. B. Ruff. Age Trends in Femur Stresses From a Simulated Fall on the Hip Among Men and Women: Evidence of Homeostatic Adaptation Underlying the Decline in Hip BMD. *Journal of Bone and Mineral Research*, 21(9):1425–1432, 2006.
- S. Bernard, J. Schneider, P. Varga, P. Laugier, K. Raum, and Q. Grimal. Elasticity–density and viscoelasticity–density relationships at the tibia mid-diaphysis assessed from resonant ultrasound spectroscopy measurements. *Biomechanics and Modeling in Mechanobiology*, 15(1):97–109, 2015.
- S. Bernard, V. Monteiller, D. Komatitsch, and P. Lasaygues. Ultrasonic computed tomography based on full-waveform inversion for bone quantitative imaging. *Physics in Medicine & Biology*, 62(17):7011–7035, 2017.
- N. Bochud, Q. Vallet, J.-G. Minonzio, and P. Laugier. Predicting bone strength with ultrasonic guided waves. *Scientific Reports*, pages 1–14, 2017.
- M. Bonnet. Topological sensitivity for 3D elastodynamic and acoustic inverse scattering in the time domain. *Elsevier*, 195:5239–5254, 2006.
- M. Bonnet and G. Delgado. The topological derivative in anisotropic elasticity. *Quarterly Journal of Mechanics and Applied Mathematics*, 66:557–386, 2013.
- E. Bossy, M. Talmant, and P. Laugier. Three-dimensional simulations of ultrasonic axial transmission velocity measurement on cortical bone models. *The Journal of the Acoustical Society of America*, 115(5):2314–2324, 2004a.
- E. Bossy, M. Talmant, F. Peyrin, L. Akrouf, P. Cloetens, and P. Laugier. An In Vitro Study of the Ultrasonic Axial Transmission Technique at the Radius: 1-MHz Velocity Measurements Are Sensitive to Both Mineralization and Intracortical Porosity. *Journal of Bone and Mineral Research*, 19(9):1548–1556, 2004b.
- V. Bousson, A. Le Bras, F. Roqueplan, Y. Kang, D. Mitton, S. Kolta, C. Bergot, W. Skalli, E. Vicaud, W. Kalender, K. Engelke, and J. D. Laredo. Volumetric quantitative computed tomography of the proximal femur: relationships linking geometric and densitometric variables to bone strength. Role for compact bone. *Osteoporosis International*, 17(6):855–864, 2006.

- S. Boutroy, M. L. Bouxsein, F. Munoz, and P. D. Delmas. In Vivo Assessment of Trabecular Bone Microarchitecture by High-Resolution Peripheral Quantitative Computed Tomography. *The Journal of Clinical Endocrinology & Metabolism*, 90(12):6508–6515, 2005.
- M. L. Bouxsein and S. E. Radloff. Quantitative Ultrasound of the Calcaneus Reflects the Mechanical Properties of Calcaneal Trabecular Bone. *Journal of Bone and Mineral Research*, 12(5):839–846, 1997.
- K. Briot and C. Roux. Ostéoporose cortico-induite. *La Revue de Médecine Interne*, 34(5):315–323, 2013.
- K. Briot, S. Paternotte, S. Kolta, R. Eastell, D. Felsenberg, D. M. Reid, C.-C. Glüer, and C. Roux. FRAX®: Prediction of Major Osteoporotic Fractures in Women from the General Population: The OPUS Study. *PLoS ONE*, 8(12):e83436, 2013.
- R. Brossier, S. Operto, and J. Virieux. Robust elastic frequency-domain full-waveform inversion using the L1norm. *Geophysical Research Letters*, 36(20):136, 2009.
- S. Chaffa, V. Roberjot, F. Peyrin, G. Berger, and P. Laugier. Frequency dependence of ultrasonic backscattering in cancellous bone: Autocorrelation model and experimental results. *The Journal of the Acoustical Society of America*, 108(5):2403–2411, 2000.
- S. Chen and D. Donoho. Basis pursuit. In *1994 28th Asilomar Conference on Signals, Systems and Computers*, pages 41–44. IEEE Comput. Soc. Press.
- J. F. Claerbout. TOWARD A UNIFIED THEORY OF REFLECTOR MAPPING. *GEOPHYSICS*, 36(3):467–481, 1971.
- P. COURTIER and O. TALAGRAND. Variational assimilation of meteorological observations with the adjoint vorticity equation. II: Numerical results. *Quarterly Journal of the Royal Meteorological Society*, 113(478):1329–1347, 1987.
- M. O. Culjat, D. Goldenberg, P. Tewari, and R. S. Singh. A Review of Tissue Substitutes for Ultrasound Imaging. *Ultrasound in Medicine & Biology*, 36(6):861–873, 2010.
- J. D. Currey. Bone Strength: What are We Trying to Measure? *Calcified Tissue International*, 68(4):205–210, 2001.

- R. Demirli and J. Saniie. Model-based estimation of ultrasonic echoes. Part II: Nondestructive evaluation applications. *IEEE Transactions on Ultrasonics, Ferroelectrics and Frequency Control*, 48(3):803–811, 2001.
- S. Dencks, R. Barkmann, F. Padilla, P. Laugier, G. Schmitz, and C. C. Gluer. Model-based estimation of quantitative ultrasound variables at the proximal femur. *IEEE Transactions on Ultrasonics, Ferroelectrics and Frequency Control*, 55(6):1304–1315, 2008.
- N. Dominguez and V. Gibiat. Non-destructive imaging using the time domain topological energy method. *Ultrasonics*, 50(3):367–372, 2010.
- N. Dominguez, V. Gibiat, and Y. Esquerre. Time domain topological gradient and time reversal analogy: an inverse method for ultrasonic target detection. *Wave Motion*, 42(1):31–52, 2005.
- E. Donnelly. Methods for Assessing Bone Quality: A Review. *Clinical Orthopaedics and Related Research*®, 469(8):2128–2138, 2010.
- D. L. Donoho and X. Huo. Uncertainty principles and ideal atomic decomposition. *IEEE Transactions on Information Theory*, 47(7):2845–2862, 2001.
- P. Droin, G. Berger, and P. Laugier. Velocity dispersion of acoustic waves in cancellous bone. *IEEE Transactions on Ultrasonics, Ferroelectrics and Frequency Control*, 45(3):581–592, 1998.
- V. Egorov, A. Tatarinov, N. Sarvazyan, R. Wood, L. Magidenko, S. Amin, S. Khosla, R. J. Ruh, J. M. Ruh, and A. Sarvazyan. Osteoporosis detection in postmenopausal women using axial transmission multi-frequency bone ultrasonometer: Clinical findings. *Ultrasonics*, 54(5):1170–1177, 2014.
- H. W. Engl, M. Hanke, and A. Neubauer. Tikhonov Regularization of Nonlinear Problems. In *Regularization of Inverse Problems*, pages 241–276. Springer Netherlands, Dordrecht, 1996.
- A. W. Enneman, K. M. A. Swart, M. C. Zillikens, S. C. van Dijk, J. P. van Wijngaarden, E. M. Brouwer-Brolsma, R. A. M. Dhonukshe-Rutten, A. Hofman, F. Rivadeneira, T. J. M. van der Cammen, P. Lips, C. P. G. M. de Groot, A. G. Uitterlinden, J. B. J. van Meurs, N. M. van Schoor, and N. van der Velde. The association between plasma homocysteine levels and bone quality and bone mineral density parameters in older persons. *Bone*, 63:141–146, 2014.
- H. A. Eschenauer, V. V. Kobelev, and A. Schumacher. Bubble method for topology and shape optimization of structures. *Structural Optimization*, 8(1):42–51, 1994.

- M. Fink. Time reversal of ultrasonic fields. I. Basic principles. *IEEE Transactions on Ultrasonics, Ferroelectrics and Frequency Control*, 39(5):555–566, 1992.
- J. Foiret, J. Minonzio, M. Talmant, and P. Laugier. Cortical bone quality assessment using quantitative ultrasound on long bones. In *2012 34th Annual International Conference of the IEEE Engineering in Medicine and Biology Society (EMBC)*, pages 1121–1124. IEEE, 2012.
- J. Foiret, J.-G. Minonzio, C. Chappard, M. Talmant, and P. Laugier. Combined estimation of thickness and velocities using ultrasound guided waves: a pioneering study on in vitro cortical bone samples. *IEEE Transactions on Ultrasonics, Ferroelectrics and Frequency Control*, 61(9):1478–1488, 2014.
- M. L. Frost, G. M. Blake, and I. Fogelman. Quantitative Ultrasound and Bone Mineral Density Are Equally Strongly Associated with Risk Factors for Osteoporosis. *Journal of Bone and Mineral Research*, 16(2):406–416, 2001.
- S. Garreau, P. Guillaume, and M. Masmoudi. The Topological Asymptotic for PDE Systems: The Elasticity Case. *SIAM Journal on Control and Optimization*, 39(6):1756–1778, 2001.
- V. Gibiat, P. Sahuguet, and A. Chouippe. Wave Guide Imaging through Time Domain Topological Energy. *Physics Procedia*, 3(1):523–531, 2010.
- V. Gibiat, X. Jacob, S. Rodriguez, and P. Sahuguet. Imaging of a fractal pattern with time and frequency domain topological derivative. *The Journal of the Acoustical Society of America*, 138(3):1765–1765, 2015.
- I. F. Gorodnitsky and B. D. Rao. Sparse signal reconstruction from limited data using FOCUSS: a re-weighted minimum norm algorithm. *IEEE Transactions on Signal Processing*, 45(3):600–616, 1997.
- M. A. Greenfield. Current status of physical measurements of the skeleton. *Medical Physics*, 19(6):1349–1357, 1998.
- Q. Grimal and P. Laugier. Quantitative ultrasound assessment of cortical bone properties beyond bone mineral density. *IRBM (in press)*, 2019.
- Q. Grimal, J. Grondin, S. Guérard, R. Barkmann, K. Engelke, C.-C. Glüer, and P. Laugier. Quantitative ultrasound of cortical bone in the femoral neck predicts femur strength: Results of a pilot study. *Journal of Bone and Mineral Research*, 28(2):302–312, 2013.

- B. B. Guzina and M. Bonnet. Topological derivative for the inverse scattering of elastic waves. *Quarterly Journal Mechanics Applied Mathematics*, 57:161–179, 2004.
- G. Haiat, F. Padilla, R. Barkmann, S. Kolta, C. Latremouille, C. C. Gluer, and P. Laugier. In vitro speed of sound measurement at intact human femur specimens. *Ultrasound in Medicine & Biology*, 31(7):987–996, 2005.
- S. Han, J. Rho, J. Medige, and I. Ziv1. Ultrasound velocity and broadband attenuation over a wide range of bone mineral density. *Osteoporosis International*, 6(4):291–296, 1996.
- T. N. Hangartner and D. F. Short. Accurate quantification of width and density of bone structures by computed tomography. *Medical Physics*, 34(10):3777–3784, 2007.
- D. Hans and S. Baim. Quantitative Ultrasound (QUS) in the Management of Osteoporosis and Assessment of Fracture Risk. *Journal of Clinical Densitometry*, 20(3):322–333, 2017.
- D. Hans and M. A. Krieg. The clinical use of quantitative ultrasound (QUS) in the detection and management of osteoporosis. *IEEE Transactions on Ultrasonics, Ferroelectrics and Frequency Control*, 55(7):1529–1538, 2008.
- R. P. Heaney. Osteoporotic bone fragility. Detection by ultrasound transmission velocity. *JAMA: The Journal of the American Medical Association*, 261(20):2986–2990, 1989.
- G. Holzer, G. von Skrbensky, L. A. Holzer, and W. Pichl. Hip Fractures and the Contribution of Cortical Versus Trabecular Bone to Femoral Neck Strength. *Journal of Bone and Mineral Research*, 24(3):468–474, 2009.
- J.-C. Hong, K. H. Sun, and Y. Y. Kim. The matching pursuit approach based on the modulated Gaussian pulse for efficient guided-wave damage inspection. *Smart Materials and Structures*, 14(4):548–560, 2005.
- W. Jeong, H.-Y. Lee, and D.-J. Min. Full waveform inversion strategy for density in the frequency domain. *Geophysical Journal International*, 188(3):1221–1242, 2012.
- R. Jing, R. Madis, and F. Zheng. Quantitative imaging of thickness maps using ultrasonic guided wave tomography based on full-waveform inversion. In *2016 IEEE Far East NDT New Technology & Application Forum (FENDT)*, pages 235–239. IEEE, 2016.

- J. A. Kanis and C. C. Gluer. An Update on the Diagnosis and Assessment of Osteoporosis with Densitometry. *Osteoporosis International*, 11(3):192–202, 2000.
- J. Karjalainen, O. Riekkinen, J. Töyräs, H. Kroger, and J. Jurvelin. Ultrasonic assessment of cortical bone thickness in vitro and in vivo. *IEEE Transactions on Ultrasonics, Ferroelectrics and Frequency Control*, 55(10):2191–2197, 2008a.
- J. Karjalainen, O. Riekkinen, J. Töyräs, H. Kroger, and J. Jurvelin. Ultrasonic assessment of cortical bone thickness in vitro and in vivo. *IEEE Transactions on Ultrasonics, Ferroelectrics and Frequency Control*, 55(10):2191–2197, 2008b.
- J. P. Karjalainen, O. Riekkinen, and H. Kroger. Pulse-echo ultrasound method for detection of post-menopausal women with osteoporotic BMD. *Osteoporosis International*, 29(5):1193–1199, 2018.
- D. Kiyashchenko, R. E. Plessix, and B. Kashtan. Modified imaging principle: An alternative to preserved-amplitude least-squares wave-equation migration. *GEO-PHYSICS*, 72(6):S221–S230, 2007.
- D. Komatitsch and J. Tromp. Spectral-element simulations of global seismic wave propagation-I. Validation. *Geophysical Journal International*, 149(2):390–412, 2002.
- D. Komatitsch, Z. Xie, E. Bozdağ, E. Sales de Andrade, D. Peter, Q. Liu, and J. Tromp. Anelastic sensitivity kernels with parsimonious storage for adjoint tomography and full waveform inversion. *Geophysical Journal International*, 206(3):1467–1478, 2016.
- M. A. Krieg and H. Didier. Quantitative ultrasound in the management of osteoporosis. *The Journal of the Acoustical Society of America*, 127(3):2006–2006, 2010.
- R. Kuc, M. Schwartz, and L. V. Micsky. Parametric Estimation of the Acoustic Attenuation Coefficient Slope for Soft Tissue. In *1976 Ultrasonics Symposium*, pages 44–47. IEEE, 1976.
- R. Lakes, H. S. Yoon, and J. Lawrence Katz. Ultrasonic wave propagation and attenuation in wet bone. *Journal of Biomedical Engineering*, 8(2):143–148, 1986.
- C. M. Langton, A. V. Ali, C. M. Riggs, G. P. Evans, and W. Bonfield. A contact method for the assessment of ultrasonic velocity and broadband attenuation in cortical and cancellous bone. *Clinical Physics and Physiological Measurement*, 11(3):243–249, 2001.

- P. Lasaygues. Assessing the cortical thickness of long bone shafts in children, using two-dimensional ultrasonic diffraction tomography. *Ultrasound in Medicine & Biology*, 32(8):1215–1227, 2006.
- P. Lasaygues and J. P. Lefebvre. Bone Imaging by Low Frequency Ultrasonic Reflection Tomography. In *Acoustical Imaging*, pages 507–514. Kluwer Academic Publishers, Boston, 2002.
- P. Lasaygues, J. P. Lefebvre, and M. Bouvat-Merlin. High-Resolution Process in Ultrasonic Reflection Tomography. In *Acoustical Imaging*, pages 35–41. Springer, Boston, MA, Boston, 2002.
- P. Lasaygues, R. Guillermin, and J.-P. Lefebvre. Ultrasonic Computed Tomography. In *Bone Quantitative Ultrasound*, pages 441–459. Springer, Dordrecht, Dordrecht, 2011.
- P. Laugier. Instrumentation for in vivo ultrasonic characterization of bone strength. *IEEE Transactions on Ultrasonics, Ferroelectrics and Frequency Control*, 55(6):1179–1196, 2008.
- P. Laugier and G. Häiat. *Bone Quantitative Ultrasound*. Springer Science & Business Media, Dordrecht, 2010.
- P. Laugier and G. Häiat. Introduction to the Physics of Ultrasound. In *Bone Quantitative Ultrasound*, pages 29–45. Springer, Dordrecht, Dordrecht, 2011.
- P. Laugier, P. Giat, P. Droin, A. Saied, and G. Berger. Ultrasound images of the os calcis: a new method of assessment of bone status. In *IEEE Ultrasonics Symposium*, pages 989–992. IEEE.
- L. H. Le. An investigation of pulse-timing techniques for broadband ultrasonic velocity determination in cancellous bone: a simulation study. *Physics in Medicine & Biology*, 43(8):2295–2308, 1999.
- S. Lees and D. Z. Klopholz. Sonic velocity and attenuation in wet compact cow femur for the frequency range 5 to 100 MHz. *Ultrasound in Medicine & Biology*, 18(3):303–308, 1992.
- F. Lefebvre, Y. Deblock, P. Campistron, D. Ahite, and J. J. Fabre. Development of a new ultrasonic technique for bone and biomaterials in vitro characterization. *Journal of Biomedical Materials Research*, 63(4):441–446, 2002.

- C. Li, N. Duric, P. Littrup, and L. Huang. In vivo Breast Sound-Speed Imaging with Ultrasound Tomography. *Ultrasound in Medicine & Biology*, 35(10):1615–1628, 2009.
- D. C. Liu and J. Nocedal. On the limited memory BFGS method for large scale optimization. *Mathematical Programming*, 45(1-3):503–528, 1989.
- Q. Liu and J. Tromp. Finite-Frequency Kernels Based on Adjoint Methods. *Bulletin of the Seismological Society of America*, 96(6):2383–2397, 2006.
- Q. Liu and J. Tromp. Finite-frequency sensitivity kernels for global seismic wave propagation based upon adjoint methods. *Geophysical Journal International*, 174(1):265–286, 2008.
- C. Lu, J. Lin, W. Chew, and G. Otto. Image Reconstruction with Acoustic Measurement Using Distorted Born Iteration Method. *Ultrasonic Imaging*, 18(2):140–156, 2016.
- Y. Lu and J. E. Michaels. Ultrasonic Signal Decomposition via Matching Pursuit with an Adaptive and Interpolated Dictionary. In *REVIEW OF PROGRESS IN QUANTITATIVE NONDESTRUCTIVE EVALUATION*, pages 579–586. AIP, 2007.
- Y. Lu and J. E. Michaels. Numerical implementation of matching pursuit for the analysis of complex ultrasonic signals. *IEEE Transactions on Ultrasonics, Ferroelectrics and Frequency Control*, 55(1):173–182, 2008.
- Y. Luo, H. Zhu, T. Nissen-Meyer, C. Morency, and J. Tromp. Seismic modeling and imaging based upon spectral-element and adjoint methods. *The Leading Edge*, 28(5):568–574, 2009.
- Y. Ma and D. Hale. A projected Hessian matrix for full waveform inversion. In *SEG Technical Program Expanded Abstracts 2011*, pages 2401–2405. Society of Exploration Geophysicists, 2012.
- I. Mano, K. Horii, H. Hagino, T. Miki, M. Matsukawa, and T. Otani. Estimation of in vivo cortical bone thickness using ultrasonic waves. *Journal of Medical Ultrasonics*, 42(3):315–322, 2015.
- D. Marshall, O. Johnell, and H. Wedel. Meta-analysis of how well measures of bone mineral density predict occurrence of osteoporotic fractures. *BMJ*, 312(7041):1254–1259, 1996.

- M. Masmoudi, J. Pommier, and B. Samet. The topological asymptotic expansion for the Maxwell equations and some applications. *Inverse Problems*, 21(2):547–564, 2005.
- P. M. Mayhew, C. D. Thomas, J. G. Clement, N. Loveridge, T. J. Beck, W. Bonfield, C. J. Burgoyne, and J. Reeve. Relation between age, femoral neck cortical stability, and hip fracture risk. *The Lancet*, 366(9480):129–135, 2005.
- E. V. McCloskey, S. A. Murray, D. Charlesworth, C. Miller, J. Fordham, K. Clifford, R. Atkins, and J. A. Kanis. Assessment of broadband ultrasound attenuation in the os calcis in vitro. *Clinical Science*, 78(2):221–225, 1990.
- J. M. Mendel. On: “Inversion of normal incidence seismograms” by A. Bamberger, G. Chavent, Ch. Hemon, and P. Lailly (G EOPHYSICS, May 1982, p. 757–770). *GEOPHYSICS*, 48(10):1411–1411, 1983.
- J.-G. Minonzio, J. Foiret, M. Talmant, and P. Laugier. Impact of attenuation on guided mode wavenumber measurement in axial transmission on bone mimicking plates. *The Journal of the Acoustical Society of America*, 130(6):3574–3582, 2011.
- R. T. Modrak, D. Borisov, M. Lefebvre, and J. Tromp. SeisFlows—Flexible waveform inversion software. *Computers & Geosciences*, 115:88–95, 2018.
- P. Moilanen. Ultrasonic guided waves in bone. *IEEE Transactions on Ultrasonics, Ferroelectrics and Frequency Control*, 55(6):1277–1286, 2008.
- P. Moilanen, P. H. F. Nicholson, T. K rkk inen, Q. Wang, J. Timonen, and S. Cheng. Assessment of the tibia using ultrasonic guided waves in pubertal girls. *Osteoporosis International*, 14(12):1020–1027, 2003.
- P. Moilanen, M. Talmant, P. H. F. Nicholson, S. Cheng, J. Timonen, and P. Laugier. Ultrasonically determined thickness of long cortical bones: Three-dimensional simulations of in vitro experiments. *The Journal of the Acoustical Society of America*, 122(4):2439–2445, 2007.
- E. Mor, A. Azoulay, and M. Aladjem. A matching pursuit method for approximating overlapping ultrasonic echoes. *IEEE Transactions on Ultrasonics, Ferroelectrics and Frequency Control*, 57(9):1996–2004, 2010.
- P. Mora. Nonlinear two-dimensional elastic inversion of multioffset seismic data. *GEOPHYSICS*, 52(9):1211–1228, 1987.

- P. Mora. Elastic wavefield inversion and the adjoint operation for the elastic wave equation. In *Mathematical Geophysics*, pages 117–137. Springer Netherlands, Dordrecht, 1988.
- P. Mora. Inversion = migration + tomography. *GEOPHYSICS*, 54(12):1575–1586, 1989.
- L. T. Nguyen and R. T. Modrak. Ultrasonic wavefield inversion and migration in complex heterogeneous structures: 2D numerical imaging and nondestructive testing experiments. *Ultrasonics*, 82:357–370, 2018.
- P. H. F. Nicholson, G. Lowet, C. M. Langton, J. Dequeker, and G. V. d. Perre. A comparison of time-domain and frequency-domain approaches to ultrasonic velocity measurement in trabecular bone. *Physics in Medicine & Biology*, 41(11):2421–2435, 1999.
- K. K. Nishiyama, H. M. Macdonald, H. R. Buie, D. A. Hanley, and S. K. Boyd. Postmenopausal Women With Osteopenia Have Higher Cortical Porosity and Thinner Cortices at the Distal Radius and Tibia Than Women With Normal aBMD: An In Vivo HR-pQCT Study. *Journal of Bone and Mineral Research*, pages 091019190442039–30, 2009.
- C. F. Njeh, D. Hans, J. Li, B. Fan, T. Fuerst, Y. Q. He, E. Tsuda-Futami, Y. Lu, C. Y. Wu, and H. K. Genant. Comparison of Six Calcaneal Quantitative Ultrasound Devices: Precision and Hip Fracture Discrimination. *Osteoporosis International*, 11(12):1051–1062, 2001.
- J. Nocedal. Theory of algorithms for unconstrained optimization. *Acta Numerica*, 1:199, 1992.
- S. Norton. Ultrasonic reflectivity tomography: Reconstruction with circular transducer arrays. *Ultrasonic Imaging*, 1(2):154–184, 1979.
- W. P. Olszynski, J. D. Adachi, D. A. Hanley, K. S. Davison, and J. P. Brown. Comparison of Speed of Sound Measures Assessed by Multisite Quantitative Ultrasound to Bone Mineral Density Measures Assessed by Dual-Energy X-Ray Absorptiometry in a Large Canadian Cohort: the Canadian Multicentre Osteoporosis Study (CaMos). *Journal of Clinical Densitometry*, 19(2):234–241, 2016.
- S. Operto, J. Virieux, A. Ribodetti, and J. E. Anderson. Finite-difference frequency-domain modeling of viscoacoustic wave propagation in 2D tilted transversely isotropic (TTI) media. *GEOPHYSICS*, 74(5):T75–T95, 2009.

- Y. C. Pati, R. Rezaifar, and P. S. Krishnaprasad. Orthogonal matching pursuit: recursive function approximation with applications to wavelet decomposition. In *27th Asilomar Conference on Signals, Systems and Computers*, pages 40–44. IEEE Comput. Soc. Press.
- M. Pérez-Liva, J. L. Herraiz, J. M. Udías, E. Miller, B. T. Cox, and B. E. Treeby. Time domain reconstruction of sound speed and attenuation in ultrasound computed tomography using full wave inversion. *The Journal of the Acoustical Society of America*, 141(3):1595–1604, 2017.
- R. E. Plessix. A review of the adjoint-state method for computing the gradient of a functional with geophysical applications. *Geophysical Journal International*, 167(2):495–503, 2006.
- R. E. Plessix and H. Rynja. VTI full waveform inversion: a parameterization study with a narrow azimuth streamer data example. In *SEG Technical Program Expanded Abstracts 2010*, pages 962–966. Society of Exploration Geophysicists, 2012.
- C. Prada, J. L. Thomas, and M. Fink. The iterative time reversal process: Analysis of the convergence. *The Journal of the Acoustical Society of America*, 97(1):62–71, 1995.
- G. Pratt, C. Shin, and Hicks. Gauss-Newton and full Newton methods in frequency-space seismic waveform inversion. *Geophysical Journal International*, 133(2):341–362, 1998.
- Prins, Jørgensen, Jørgensen, and Hassager. The role of quantitative ultrasound in the assessment of bone: a review. *Clinical Physiology*, 18(1):3–17, 1998.
- Prins, Jørgensen, and Hassager. The role of quantitative ultrasound in the assessment of bone: a review. *Clinical Physiology*, 18(1):3–17, 2008.
- V. C. Protopappas, I. C. Kourtis, L. C. Kourtis, K. N. Malizos, C. V. Massalas, and D. I. Fotiadis. Three-dimensional finite element modeling of guided ultrasound wave propagation in intact and healing long bones. *The Journal of the Acoustical Society of America*, 121(6):3907, 2007.
- C. Ravaut, S. Operto, L. Improta, J. Virieux, A. Herrero, and P. Dell’Aversana. Multiscale imaging of complex structures from multifold wide-aperture seismic data by frequency-domain full-waveform tomography: application to a thrust belt. *Geophysical Journal International*, 159(3):1032–1056, 2004.

- G. Renaud, P. Kruizinga, D. Cassereau, and P. Laugier. In vivo ultrasound imaging of the bone cortex. *Physics in Medicine & Biology*, 63(12):125010, 2018.
- R. O. Ritchie, M. J. Buehler, and P. Hansma. Plasticity and toughness in bone. *Physics Today*, 62(6):41–47, 2009.
- S. Rodriguez, P. Sahuguet, V. Gibiat, and X. Jacob. Fast topological imaging. *Ultrasonics*, 52(8):1010–1018, 2012.
- K. Rohde, D. Rohrbach, C.-C. Glüer, P. Laugier, Q. Grimal, K. Raum, and R. Barkmann. Influence of porosity, pore size, and cortical thickness on the propagation of ultrasonic waves guided through the femoral neck cortex: a simulation study. *IEEE Transactions on Ultrasonics, Ferroelectrics and Frequency Control*, 61(2):302–313, 2014.
- P. Rossman, J. Zagzebski, C. Mesina, J. Sorenson, and R. Mazess. Comparison of speed of sound and ultrasound attenuation in the os calcis to bone density of the radius, femur and lumbar spine. *Clinical Physics and Physiological Measurement*, 10(4):353–360, 2001.
- N. Ruiz-Reyes, P. Vera-Candeas, J. Curpián-Alonso, J. C. Cuevas-Martinez, and F. López-Ferreras. RETRACTED: Matching pursuit-based approach for ultrasonic flaw detection. *Signal Processing*, 86(5):962–970, 2006.
- S. K. Sahoo and A. Makur. Signal Recovery from Random Measurements via Extended Orthogonal Matching Pursuit. *IEEE Transactions on Signal Processing*, 63(10):2572–2581, 2015.
- P. Sahuguet, A. Chouippe, and V. Gibiat. Biological tissues imaging with time domain topological energy. *Physics Procedia*, 3(1):677–683, 2010.
- H. Sai, G. Iguchi, T. Tobimatsu, K. Takahashi, T. Otani, K. Horii, I. Mano, I. Nagai, H. Iio, T. Fujita, K. Yoh, and H. Baba. Novel ultrasonic bone densitometry based on two longitudinal waves: significant correlation with pQCT measurement values and age-related changes in trabecular bone density, cortical thickness, and elastic modulus of trabecular bone in a normal Japanese population. *Osteoporosis International*, 21(10):1781–1790, 2010.
- G. Y. Sandhu, C. Li, O. Roy, S. Schmidt, and N. Duric. Frequency domain ultrasound waveform tomography: breast imaging using a ring transducer. *Physics in Medicine & Biology*, 60(14):5381–5398, 2015a.

- G. Y. S. Sandhu, C. Li, O. Roy, S. Schmidt, and N. Duric. High-resolution quantitative whole-breast ultrasound: in vivo application using frequency-domain waveform tomography. In J. G. Bosch and N. Duric, editors, *SPIE Medical Imaging*, page 94190D. SPIE, 2015b.
- A. Sarvazyan, A. Tatarinov, V. Egorov, S. Airapetian, V. Kurtenok, and C. J. Gatt Jr. Application of the dual-frequency ultrasonometer for osteoporosis detection. *Ultrasonics*, 49(3):331–337, 2009.
- M. Sasso, G. Haiat, Y. Yamato, S. Naili, and M. Matsukawa. Dependence of ultrasonic attenuation on bone mass and microstructure in bovine cortical bone. *Journal of Biomechanics*, 41(2):347–355, 2008.
- J. T. Schousboe, O. Riekkinen, and J. Karjalainen. Prediction of hip osteoporosis by DXA using a novel pulse-echo ultrasound device. *Osteoporosis International*, pages 1–9, 2016.
- L. Sirgue and R. G. Pratt. Efficient waveform inversion and imaging: A strategy for selecting temporal frequencies. *GEOPHYSICS*, 69(1):231–248, 2004.
- E. Siris. Absolute Versus Relative Fracture Risk. *Journal of Bone and Mineral Research*, 20(4):705–705, 2004.
- E. S. Siris, Y.-T. Chen, T. A. Abbott, E. Barrett-Connor, P. D. Miller, L. E. Wehen, and M. L. Berger. Bone Mineral Density Thresholds for Pharmacologic Intervention to Prevent Fractures. *Obstetrical & Gynecological Survey*, 59(11):769–771, 2004.
- J. G. Snedeker, F. H. Walz, M. H. Muser, G. Schroeder, T. L. Mueller, and R. Müller. Microstructural insight into pedestrian pelvic fracture as assessed by high-resolution computed tomography. *Journal of Biomechanics*, 39(14):2709–2713, 2006.
- J. Sokolowski and A. Zochowski. On the Topological Derivative in Shape Optimization. *SIAM Journal on Control and Optimization*, 37(4):1251–1272, 1999.
- E. M. Stein, F. Rosete, P. Young, M. Kamanda-Kosseh, D. J. McMahon, G. Luo, J. J. Kaufman, E. Shane, and R. S. Siffert. Clinical Assessment of the 1/3 Radius Using a New Desktop Ultrasonic Bone Densitometer. *Ultrasound in Medicine & Biology*, 39(3):388–395, 2013.
- R. Strelitzki, A. J. Clarke, and J. A. Evans. The measurement of the velocity of ultrasound in fixed trabecular bone using broadband pulses and single-frequency tone bursts. *Physics in Medicine & Biology*, 41(4):743–753, 1999.

- O. Ström, F. Borgström, J. A. Kanis, J. Compston, C. Cooper, E. V. McCloskey, and B. Jönsson. Osteoporosis: burden, health care provision and opportunities in the EU. *Archives of Osteoporosis*, 6(1-2):59–155, 2011.
- M. Talmant, S. Kolta, C. Roux, D. Haguenauer, I. Vedel, B. Cassou, E. Bossy, and P. Laugier. In vivo Performance Evaluation of Bi-Directional Ultrasonic Axial Transmission for Cortical Bone Assessment. *Ultrasound in Medicine & Biology*, 35(6):912–919, 2009.
- A. Tarantola. Inversion of seismic reflection data in the acoustic approximation. *GEOPHYSICS*, 49(8):1259–1266, 1984.
- A. Tarantola. Inversion of travel times and seismic waveforms. In *Seismic Tomography*, pages 135–157. Springer Netherlands, Dordrecht, 1987.
- A. Tarantola. Theoretical Background for the Inversion of Seismic Waveforms, Including Elasticity and Attenuation. In *Scattering and Attenuations of Seismic Waves, Part I*, pages 365–399. Birkhäuser Basel, Basel, 1988.
- A. Tatarinov, V. Egorov, N. Sarvazyan, and A. Sarvazyan. Multi-frequency axial transmission bone ultrasonometer. *Ultrasonics*, 54(5):1162–1169, 2014.
- M. B. Tavakoli and J. A. Evans. The effect of bone structure on ultrasonic attenuation and velocity. *Ultrasonics*, 30(6):389–395, 1992.
- J. Töyräs, M. T. Nieminen, H. Kroger, and J. S. Jurvelin. Bone mineral density, ultrasound velocity, and broadband attenuation predict mechanical properties of trabecular bone differently. *Bone*, 31(4):503–507, 2002.
- J. Tromp, C. Tape, and Q. Liu. Seismic tomography, adjoint methods, time reversal and banana-doughnut kernels. *Geophysical Journal International*, 160(1):195–216, 2004.
- Q. Vallet, N. Bochud, C. Chappard, P. Laugier, and J.-G. Minonzio. In Vivo Characterization of Cortical Bone Using Guided Waves Measured by Axial Transmission. *IEEE Transactions on Ultrasonics, Ferroelectrics and Frequency Control*, 63(9):1361–1371, 2016.
- J. Virieux and S. Operto. An overview of full-waveform inversion in exploration geophysics. *GEOPHYSICS*, 74(6):WCC1–WCC26, 2009.
- K. Wang, T. Matthews, F. Anis, C. Li, N. Duric, and M. Anastasio. Waveform inversion with source encoding for breast sound speed reconstruction in ultra-

- sound computed tomography. *IEEE Transactions on Ultrasonics, Ferroelectrics and Frequency Control*, 62(3):475–493, 2015.
- K. A. Wear. Frequency dependence of ultrasonic backscatter from human trabecular bone: Theory and experiment. *The Journal of the Acoustical Society of America*, 106(6):3659–3664, 1999.
- K. A. Wear. Autocorrelation and cepstral methods for measurement of tibial cortical thickness. *IEEE Transactions on Ultrasonics, Ferroelectrics and Frequency Control*, 50(6):655–660, 2003.
- D. P. Wipf and B. D. Rao. Sparse Bayesian Learning for Basis Selection. *IEEE Transactions on Signal Processing*, 52(8):2153–2164, 2004.
- D. Wu, G. Yao, J. Cao, and Y. Wang. Least-squares RTM with L1 norm regularization. *Journal of Geophysics and Engineering*, 13(5):666–673, 2016.
- G. Yao and H. Jakubowicz. Least-squares reverse-time migration in a matrix-based formulation. *Geophysical Prospecting*, 64(3):611–621, 2015.
- R. M. Zebaze, A. Ghasem-Zadeh, A. Bohte, S. Iuliano-Burns, M. Mirams, R. I. Price, E. J. Mackie, and E. Seeman. Intracortical remodelling and porosity in the distal radius and post-mortem femurs of women: a cross-sectional study. *The Lancet*, 375(9727):1729–1736, 2010.
- Z. Zhang and B. D. Rao. Sparse Signal Recovery With Temporally Correlated Source Vectors Using Sparse Bayesian Learning. *IEEE Journal of Selected Topics in Signal Processing*, 5(5):912–926, 2011.
- R. Zheng, L. H. Le, M. D. Sacchi, D. Ta, and E. Lou. Spectral ratio method to estimate broadband ultrasound attenuation of cortical bones in vitrousing multiple reflections. *Physics in Medicine & Biology*, 52(19):5855–5869, 2007.
- R. Zheng, L. H. Le, M. D. Sacchi, and E. Lou. Imaging Internal Structure of Long Bones Using Wave Scattering Theory. *Ultrasound in Medicine & Biology*, 41(11):2955–2965, 2015.
- H. Zhu, Y. Luo, T. Nissen-Meyer, C. Morency, and J. Tromp. Elastic imaging and time-lapse migration based on adjoint methods. *GEOPHYSICS*, 74(6):WCA167–WCA177, 2009.